Journal of Electromagnetic Analysis and Applications

ISSN: 1942-0730 (Print), 1942-0749 (Online)

Volume 2, Number 2, February 2010

www.scirp.org/journal/jemaa

Scientific Research

JOURNAL EDITORIAL BOARD

ISSN: 1942-0730 (Print) 1942-0749 (Online)

http://www.scirp.org/journal/jemaa

J. Electromagnetic Analysis & Applications, **2010, 2, 63-119**
Published Online February 2010 in SciRes (www.SciRP.org/journal/jemaa)

TABLE OF CONTENTS

Volume 2 Number 2 February 2010

Journal of Electromagnetic Analysis and Applications (JEMAA)

Journal Information

SUBSCRIPTIONS

The *Journal of Electromagnetic Analysis and Applications* (Online at Scientific Research Publishing, www.SciRP.org) is published quarterly by Scientific Research Publishing, Inc., USA.

E-mail: jemaa@scirp.org

Subscription rates: Volume 2 2010

Print: $50 per copy.

Electronic: free, available on www.SciRP.org.

To subscribe, please contact Journals Subscriptions Department, E-mail: jemaa@scirp.org

Sample copies: If you are interested in subscribing, you may obtain a free sample copy by contacting Scientific Research Publishing, Inc at the above address.

SERVICES

Advertisements

Advertisement Sales Department, E-mail: jemaa@scirp.org

Reprints (minimum quantity 100 copies)

Reprints Co-ordinator, Scientific Research Publishing, Inc., USA.

E-mail: jemaa@scirp.org

COPYRIGHT

PRODUCTION INFORMATION

For manuscripts that have been accepted for publication, please contact:

E-mail: jemaa@scirp.org

J. Electromagnetic Analysis & Applications, **2010, 2: 63-74**
doi:10.4236/jemaa.2010.22010 Published Online February 2010 (www.SciRP.org/journal/jemaa)

A Search for a Low Anisotropic Superconductor

A. A. Khurram[1], Nawazish A. Khan[2]

[1]Experimental Physics Labs, National Centre for Physics, Quaid-i-Azam University, Islamabad, Pakistan; [2]Materials Science Laboratory, Department of Physics, Quaid-i-Azam University, Islamabad, Pakistan.
Email: khuram_qau@yahoo.com

Received July 27th, 2009; revised September 12th, 2009; accepted September 17th, 2009.

ABSTRACT

In this article, we have given a review of thallium based ($Tl_mBa_2Ca_{n-1}Cu_nO_{2n+2}$) and copper based ($CuBa_2Ca_{n-1}\ Cu_nO_{2n+4}$) high temperature superconductors. This review article is based on the methods of preparation in the form of bulk and thin films and their physical properties. We have also studied the sources of anisotropy and methods of lowering it via changing the composition of charge reservoir layer and developing a better inter-plane coupling.

Keywords: *Review Article, $Tl_mBa_2Ca_{n-1}CunO_{2n+2}$ and $CuBa_2Ca_{n-1}Cu_nO_{2n+4}$ Superconductors, Synthesis, Physical Properties*

1. Introduction

One of the general features of high temperature superconductors is the anisotropy parameter [$\gamma=\rho_c/\rho_{ab}=\xi_{ab}/\xi_c$] which comes from their layered structure. The technological critical temperature and irreversibility field which play very important role in the use of high T_c superconductors in various applications are strongly related to the anisotropy parameter as $Z==T_c/\gamma$ and $H_{irr}=H_{c2}/\gamma$ respectively The understanding of the sources of anisotropy in these layered cuprates is essential to accomplish the direly needed isotropic superconductor; i.e. like BCS superconductor. Therefore, it is very important to search for a superconducting material which has higher critical temperature, T_c, critical current density and as well as lower anisotropy. The thallium based superconductors $Tl_mBa_2Ca_{n-1}Cu_nO_{2n+2}$ (m=1, 2; n=1, 2, 3, 4, 5) are superior over other cuprates due to their higher T_c, J_c, H_{irr} and low microwave surface resistances. The maximum critical temperature achieved in both the families of thallium based superconductors is 123K and 127K and current densities are of the order of 10^6 A/cm^2. Another family of oxides which has comparable superconducting characteristics as thallium based compounds but with lower anisotropy is $Cu_mBa_2Ca_{n-1}Cu_nO_{2n+2}$ (m=1 n=1, 2, 3, 4, 5). The major disadvantage associated with these superconductors is their preparation under very high pressures i.e. 4GPa, which makes their large scale production difficult. However, the superconducting properties of $Tl_mBa_2Ca_{n-1}Cu_nO_{2n+2}$ and $Cu_mBa_2Ca_{n-1}Cu_nO_{2n+2}$ are combined in a new superconductor family which is represented as $(Cu_{1-x}Tl_x)Ba_2Ca_{n-1}Cu_nO_{2n+2}$. These superconductors are prepared at normal pressure by substituting thallium at copper site in $Cu_mBa_2Ca_{n-1}Cu_nO_{2n+2}$ superconductors. These superconductors have anisotropy parameter (γ=3-11) in between that of Cu and Tl based superconductors. In this article we have first reviewed the methods of preparation and physical properties of thallium based superconductors and then the copper based superconductor. We have also shown that the Tl-1223 as well Cu-1223 superconductors is more promising members of their families. At the end the end of the article the superconducting properties of $(Cu_{1-x}Tl_x)$ $Ba_2Ca_2Cu_3O_{10-\delta}$ are given.

2. Thallium Based Superconductors

The thallium based Tl-Ba-Ca-Cu-O (TBCCO) superconductor was discovered in 1988 by Sheng and Hermann [1,2–6] which is proven to be the best among all other cuprates due to their higher transition temperature, [$T_c(0)$], transport critical current densities, [J_c] and low microwave surface resistances, [R_s]. Since the discovery of superconductivity in this system, several new phases of $Tl_mBa_2Ca_{n-1}Cu_nO_{2n+2}$ (m=1, 2; n=1, 2, 3, 4, 5) have been synthesized [7,8–10]. In the two-layer thallium compounds, the $Tl_2Ba_2Cu_1O_6$, $Tl_2Ba_2Ca_1Cu_2O_8$, $Tl_2Ba_2Ca_2Cu_3O_{10}$, $Tl_2Ba_2Ca_3Cu_4O_{10}$, and $Tl_2Ba_2Ca_4Cu_5O_8$ are major phases, which can be simply represented as, Tl-2201, Tl-2212, Tl-2223, Tl-2224 and Tl-2245 with critical temperatures of 95, 118, 127, 112 and 105K respectively. The maximum critical temperature of ~127K is found in Tl-2223 superconductor [11,12]. On the other hand the monolayer Tl-based system includes $TlBa_2Ca_1Cu_2O_7$,

$Tl_1Ba_2Ca_2Cu_3O_9$, $TlBa_2Ca_3Cu_4O_{11}$, and $Tl\ Ba_2Ca_4Cu_5O_{13}$ superconductor phases, which for brevity can be represented as Tl-1212, Tl-1223, Tl-1234 and Tl-1245 with critical temperatures 103, 123, 112 and 107K respectively. The materials with double Tl-O layers have body centered tetragonal structure and single Tl-O layer compounds have primitive tetragonal structure. The crystal structures of Tl-2223 and Tl-1223 superconductors are shown in Figure 1. A brief review of thallium-based superconductors will be given in the following sections.

2.1 $Tl_2Ba_2Ca_{n-1}Cu_nO_{2n+2}$ Superconductors

The thallium-based compounds with double Tl-O layer in the unit cell are the best among other cuprates of LBCO, YBCO and BSCCO series due to their higher critical temperature and low microwave surface resistance. These materials exhibit tetragonal symmetry with I4/mmm space group. The structure of these compounds comprises copper provskite-like blocks with n (n=1, 2, 3…) CuO_2 planes separated by two Tl-O layers. Each CaO layer is sandwiched between two CuO_2 planes and BaO layer between the CuO_2 plane and TlO layers. These compounds can be represented by a formula Tl-22 (n1)n, where n represents the number of CuO_2 planes. The oxygen coordination number of Tl, Cu, Ca and Ba in these compounds is 6, 4/5, 8, and 9 respectively. The c-axis lengths in these materials ranges from 23.248Å for n=1 to 42.07Å for n=4 [13,14]. The critical temperature increases up to 127K with number of CuO_2 planes n from 1 to 3 and then decreases for higher number of CuO_2 planes in the unit cell of bilayer TlO compounds. In Figure 2 is shown the dependence of T_c on number of CuO_2 planes for different superconductors. Since Tl-based superconductor materials have higher critical temperature, so much attention has been given to the synthesis of bulk and thin film samples of these compounds, which can be used for electronic devices [15–24]. Among the double TlO layer compounds, the Tl-2223 is the most promising due to its high critical temperature of 127K as compared to its counterparts in double Tl-O layer series [25,26]. Both the bulk and thin film samples of this material have been prepared [22]. The superconducting properties of Tl-22(n-1)n compounds can be changed by employing different synthesis routes and doping of different cations (i.e. Hg, Pb, Sr, Y, Pr, Co etc.) in charge reservoir block and superconducting block [23,27–37]. Parkin *et al.* have been succeeded to prepare $Tl_2Ba_2Ca_2Cu_3O_x$ superconductor with critical temperature, which varies from 118 to 127K depending upon the synthesis conditions [8]. The substitution of Hg at thallium site has been seen to improve the staking regularity of the atomic layers in the 2223 phase and phase stability as compared to pure Tl-2223 phase [38–40]. The critical

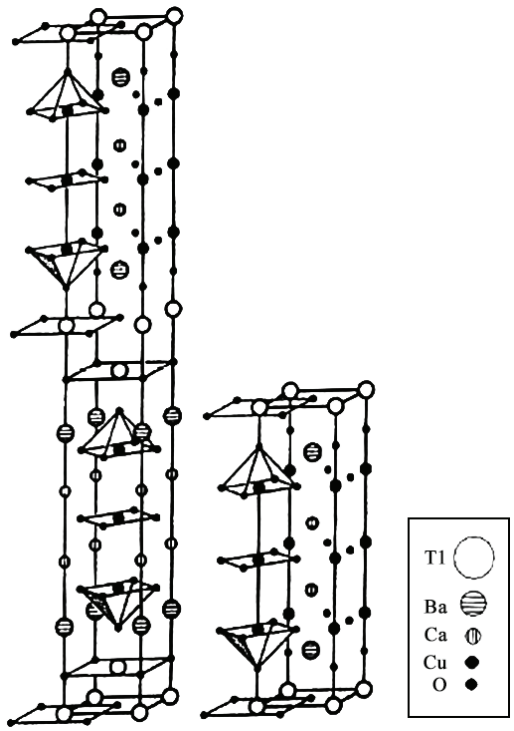

Figure 1. The crystal structures of Tl-2223 and Tl-1223 superconductor

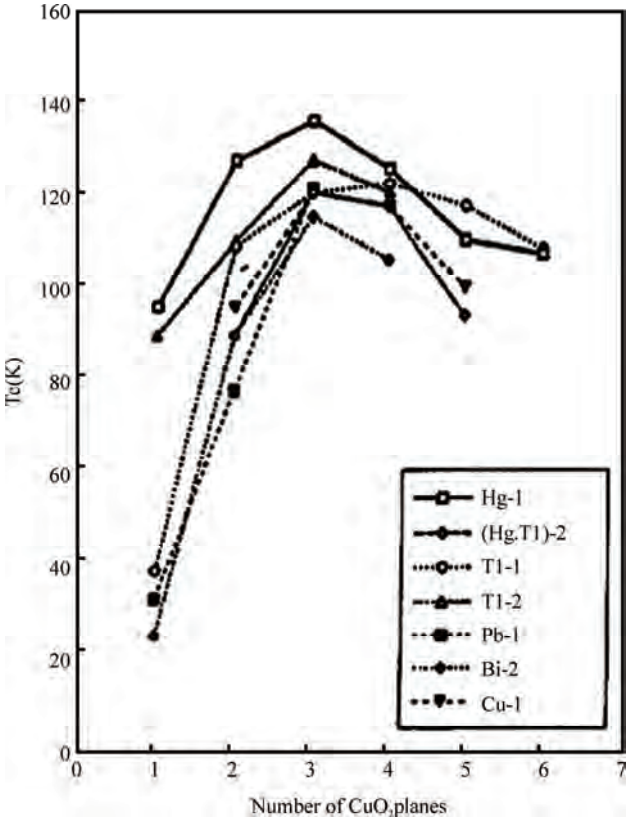

Figure 2. The dependence of critical temperature on number of CuO_2 planes in different superconductors [64]

temperature, however, decreases in TlHg-2223 to 118K but in TlHg-2212 the $T_c(0)$ has been raised to 5K higher than pure thallium based superconductor [23]. In Tl-2212 superconductors the doping of tetravalent Pr at Ca site was found to suppress the superconductivity [31]. Two reasons are proposed for the suppression of superconductivity with Pr substitution. One is the breaking of cooper pairs due to their interaction with magnetic moment of *4f* electrons of Pr ion and secondly, the localization of carriers caused by the overlap of *4f* orbital with O2p-Cu3d orbital. On the other hand the Y at Ca site in Tl-2212 superconductor has the same effect like that of Pr, suppressing the critical temperature and localization of carriers but in a different manner because Y does not have *4f* electrons [41]. The decrease in the $T_c(0)$ of Tl-2212 superconductor with Pr concentration is shown in Figure 3. Similarly the doping of magnetic impurities at Cu site in CuO_2 planes can also suppress the superconductivity due to scattering of superconducting carriers from these impurity atoms. In Tl-2212 the cobalt substitution at Cu site has shown decrease in the critical temperature with increased Co concentrations [34]. The phase purity is necessary for the use of superconducting compounds for device fabrications. The partial substitution of Ba by Sr in thallium-based superconductors can improve their phase stability. The doping of Sr at Ba in Tl-2223 superconductor resulted in a phase pure material, but with a lower $T_c(0)$ as compared to Sr free compound [30]. The addition of Ag_2O in the starting composition also stabilizes Tl-2223 phase otherwise the chances of formation of Tl-2212 superconductor with two CuO_2 layers are increased [22]. In addition to the phase stability the addition of silver can improve the intergranular coupling, which enhances the transport properties such as critical current density and decreases the room temperature resistivity [22,39,40]. The critical current density with Ag_2O doped Tl-2223 samples is estimated to be three times the critical current of undoped material [22]. Figure 4 shows the results of $T_c(0)$ and R(300K) for different

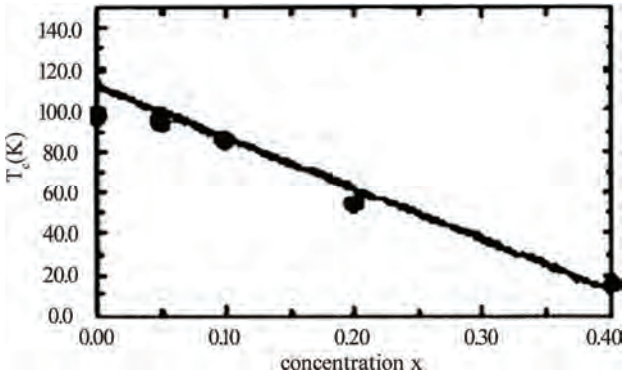

Figure 3. The lowering of critical temperature in Tl-2212 superconductor with the increase of Pr concentration [31]

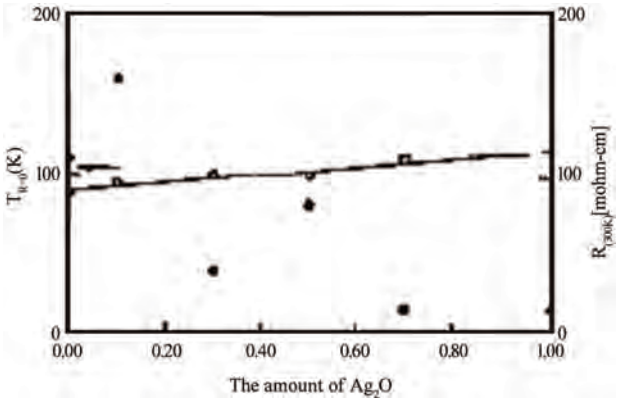

Figure 4. Variation of critical temperature and room temperature resistivity with Ag_2O concentration in Tl-2223 superconductor [22]

Ag_2O doping concentrations. The doping of Li in Tl-2223 starting composition results in a critical temperature of 117K and the normal state resistivity becomes independent of the applied magnetic fields [29]. Since the maximum $T_c(0)$ in a given compound also strongly depends on the interlayer coupling so the external pressure can be used as a source to improve the superconducting properties intrinsically. The application of pressure contracts the Cu-(apical) oxygen bond length which favors the transfer of carriers from the charge reservoir layer to CuO_2 planes. D. Tristan *et al.* have studied the properties of Tl-2223 and Tl-2234 superconductors under different pressures and found that the critical temperature (~119K) of Tl-2223 sample prepared under ambient pressure is increased to 133K when 4.2GPa pressure was applied [25]. The change in the critical temperature of Tl-2223 and Tl-2234 with applied pressure is shown in Figure 5. The reliable, high quality thin films are prerequisite for the use of thallium based high temperature superconductors for electrical, magnetic and optical applications. The methods of preparation of thin films include rf and dc sputtering, sequential electron beam and thermal evaporation, and pulsed laser ablation. The highest critical current density in double layer TlO compounds is attained in Tl-2223 thin films, which is of the order of 107 A/cm^2 (90K, 0T) [5]. On the other hand the critical current density of Tl-2212 superconductor is in the range of 10^5-10^6 A/cm^2 at 77K depending upon the deposition techniques used [42–46].

2.2 $Tl_1Ba_2Ca_{n-1}Cu_nO_{2n+2}$ Superconductors

The family of thallium based superconductors with single Tl-O layer is comprised of Tl-1212, Tl-1223 and Tl-1234 compounds. These superconducting compounds are more promising because of their lower anisotropy, higher $T_c(0)$, higher critical current densities and irreversibility field H_{irr} as compared to their counterparts in double Tl-O

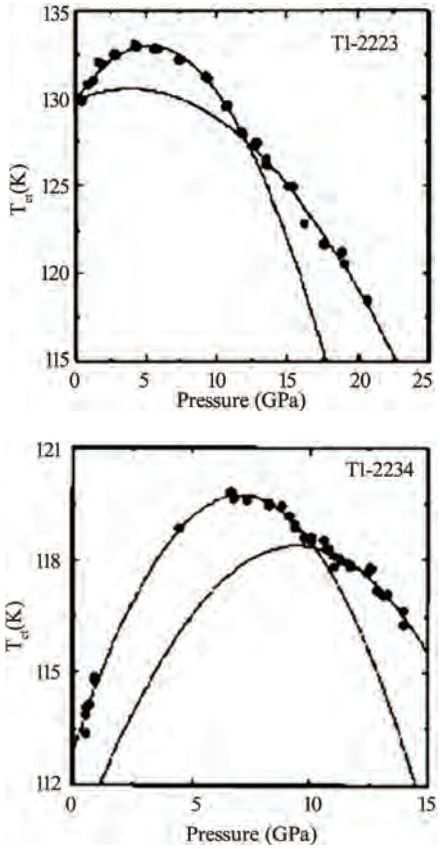

Figure 5. Effect of pressure on critical temperature of Tl-2223 and Tl-2234 superconductor [25]

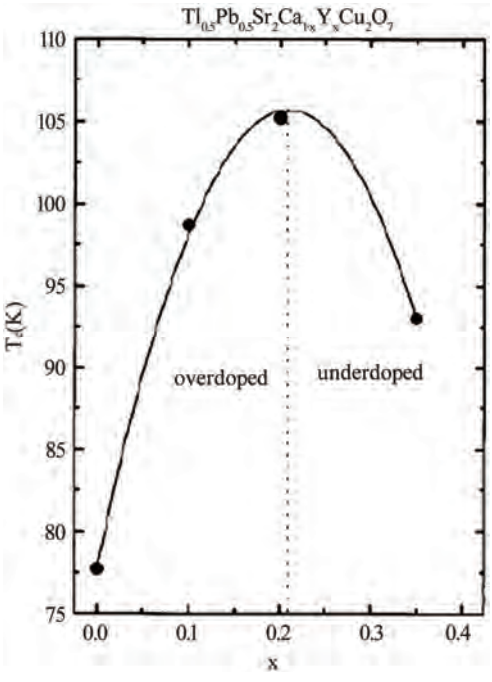

Figure 6. The $T_c(0)$ versus doping concentration of Y in TlPb-1212 superconductor [56]

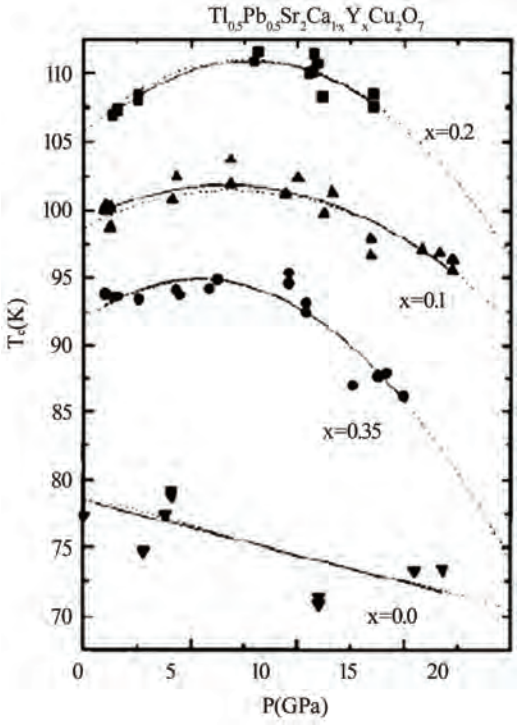

Figure 7.The variation of critical temperature with applied pressure for different concentrations of Y in TlPb-1212 superconductor [56]

layer superconductors family [47–55]. The $TlSr_2CaCu_2O_7$ (Tl-1212) is the parent compound in single Tl-O layer superconductors showing no signs of superconductivity down to liquid helium temperature because it grows in the over-doped state [56]. But the substitutions at Tl and Ca sites have been proven to bring about the superconductivity in this compound and enhance its phase stability [57–60]. When doped with Pb or Cr at the thallium site and Y at the Ca site the critical temperature has been enhanced to 110K in Tl-1212 [57,58,61]. But the Pr or Nd substitution at the Ca site lowers the $T_c(0)$ of this material because the number of holes are reduced below the optimum value; these elements promote the hole filling mechanism [61]. The application of pressure can also optimize the number of holes in CuO_2 planes and increases the critical temperature. In Figures 6 and 7, the dependence of critical temperature of TlPb-1212 superconductor (doped with Y) on the doping concentration and the applied pressure is shown. The Tl-1212 superconductor has lower anisotropy due to short insulating distance between CuO_2 planes and exhibit higher critical current density [54]. The thin films prepared by this material has J_c(77K, 0T) in the range of 10^6-10^7 A/cm^2 [54,62]. Although these materials can be used for application due to their low anisotropy but these are not ideal due to their lower $T_c(0)$ as compared to other members of this homologous series. It is observed in monolayer thal-

lium based compounds that the critical temperature depends on the number of CuO_2 planes. As the number of CuO_2 planes increases from n=3 to either n=4 or 5, the $T_c(0)$ decreases because in n>3 phases there are inequivalent CuO_2 planes in which holes are inhomogeneously distributed which results in a lowering of critical temperature, Figure 2 [63,64]. Among the $Tl_1Ba_2Ca_{n-1}Cu_nO_{2n+2}$ superconductors family the n=3 member is important due to its higher critical temperature, excellent flux-pinning properties, higher critical current and irreversibility field H_{irr} [65–70]. The Tl-1223 was the first superconducting composition reported among the other members of this family [71]. The single-phase samples of Tl-1223 are difficult to prepare. The researchers have adopted different synthesis routes to achieve a phase pure material. One way of improving the phase purity of Tl-1223 compound is the substitution of Pb and (or) Bi for Tl, and Sr for Ba in the starting composition [69,72–77]. The addition of Pb and the variation in the Ca/Sr ratio is not only helpful in stabilizing the Tl-1223 phase but also results in higher critical temperature (T_c>120K), high J_c, H_{irr} field and strong flux pinning properties at 77K [52,68,78–81,82]. The critical current density in Pb and Sr substituted sample is of the order of 103-105 A/cm^2 [55,70]. The complete replacement of Ba by Sr lowers the transition temperature of Tl-1223 superconductors [83]. In the preparation of Tl-1223 compounds it is found that a starting composition deficient in thallium produces the highest percentage of Tl-1223 phase [8]. The high vapor pressure of Tl_2O_3 at synthesis temperatures also hinders the formation of Tl-1223 superconductors [84,85]. This problem can be overcome by employing the two zone processing technique in which independent control of partial pressure of Tl_2O_3, oxygen gas, sample temperature and composition could be varied [68,85,86]. The use of high-pressure synthesis technique is also helpful in achieving single phase of Tl-1223 superconductors with out any cationic substitutions [87,88]. In addition Tl-1223 samples prepared under high pressure have shown increase in the critical temperature, transport J_c, and high irreversibility field H_{irr}, Figure 8 [77,89]. The application of pressure improves the intergranular coupling and facilitates charge transport process, which results in higher J_c and H_{irr}. A factor, which can suppress the phase stability and superconductivity in Tl-1223, is the presence of carbon in the starting composition [51,88,90]. The carbon may go to the Tl site in the unit cell and as a result decreases the number of holes in CuO_2 planes and lowers the critical temperature [88], therefore, it is necessary to minimize the carbon content in the precursor powders. The carbon can also form non-superconductor phases in the form of carbonates of Ba and/or Ca. Figure 9 shows the lowering of the critical temperature of Tl-1223 superconductor with enhanced concentration of carbon in the starting composition. The use of TlF instead of Tl_2O_3

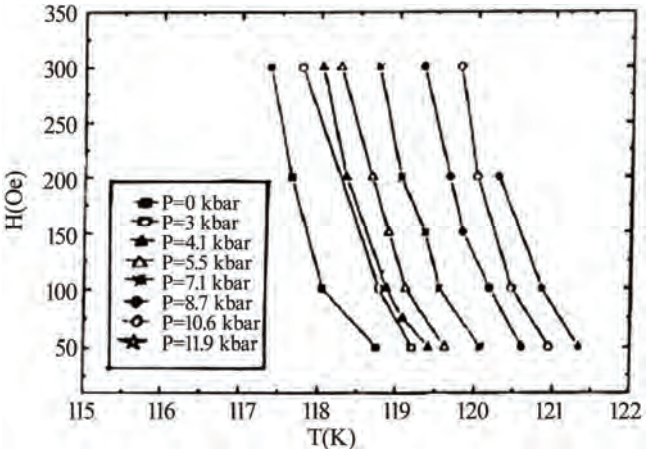

Figure 8. The shifting of irreversibility line of Tl-1223 superconductor to higher temperatures with the increased pressure [89]

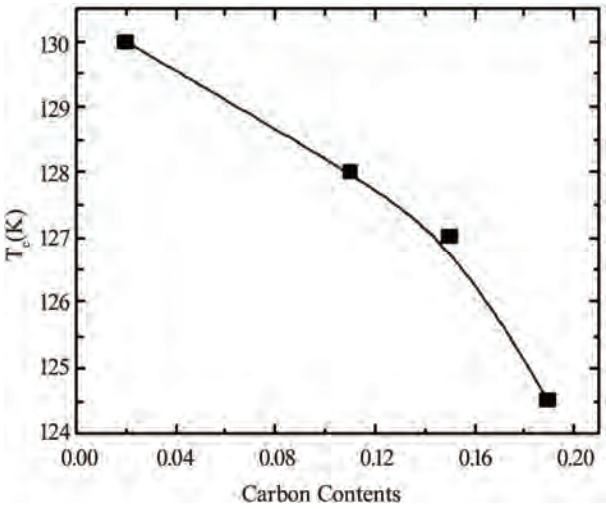

Figure 9. The decrease in critical temperature of Tl-1223 superconductor with increased carbon contents in starting composition [88]

in the starting composition of Tl-1223 enhances the formation of single phase Tl-1223 material with out any Pb or Srdoping and increases J_c(77K, 0T) and irreversibility field H_{irr} [90,91]. The thin films of Tl-1223 prepared by using TlF are found to have critical current density of 4.4×10^6 A/cm^2 at 77K in zero field [84]. Since the ionic radius of fluorine [F_{-1}(1.36Å)] is comparable to that of oxygen [O^{-2}(1.4 Å)] so fluorine most probably occupies the oxygen lattice site in the unit cell [92]. The holes concentration in the CuO_2 planes decreases when fluorine replaces oxygen in the Tl-1223 superconductor because of the more electronegative nature of F ion as compared to oxygen [93]. The carrier concentration approaches optimum level and $T_c(0)$ is increased. In Tl(Pb)Ba(Sr)Ca $CuOF_x$ composition, the critical temperature has been

enhanced with fluorine contents up to x=1 and a pure Tl-1223 phase with highest J_c was achieved with x=3 [85]. The samples of TBCCO (Tl-1223) superconductors with more than 95% purity can also be obtained by choosing the appropriate synthesis temperature and controlling the reaction time with out any substitutions [94]. Although most of the substitutions in Tl-1223 superconductors were made to improve the phase stability of these compounds but these doping can also control the carrier concentration and in turn the superconducting properties of these compounds. The rare earth cations (La, Sm, Pr, Eu) substitutions at the Ca sites in Tl-1223 superconductors have been found to lower the critical temperature and the phase stability of this compound [95–99]. But when one of the rare earth elements Ce was doped at Sr site the critical temperature was increased from 92K to 98K with the increased concentration of cerium. The increase in $T_c(0)$ was attributed to the improved coupling between the CuO_2 planes due to the decreased c-axis length [100]. The critical temperature and the critical current density of Tl-1223 superconductor decreases with low level doping concentration of 3d transition metals Co, Zn, Fe and Ni at Cu site and superconductivity disappears for higher concentrations of these elements [101–104]. The presence of these ions in CuO_2 planes acts as scattering centers, which resulted in the Cooper pair breaking, and destroys the superconducting state in Tl-1223 compounds. When the transition metal ions are substituted at the Tl site in the charge reservoir layer of Tl-1223 superconductor the critical temperature was decreased following the same mechanism mentioned earlier [105]. The thin films of thallium based superconductors are of interest for electronic devices due to their higher $T_c(0)$ and low surface resistance R_s [106]. Among the thallium-based compounds the thin films of single TlO layer materials (Tl-1223) are superior because of their higher $T_c(0)$ and J_c [107]. Thin films of Tl-1223 superconductors have critical current density in the range of 10^5-10^6 A/cm^2 at 77K (both in field cooled and zero field cooled samples) depending upon the deposition technique adopted [47,66,84,107–109].

3. Why Tl-1223 Superconductor is Superior

The Tl-based high T_c cuprates exhibit layered structure which consists of intergrowths along c-axis containing CuO_2 planes and rock salt type layers containing Tl cations. The insulating Tl-O layers separate the CuO_2 blocks in the crystal. The CuO_2 planes are found to be more favorable for superconductivity as compared to insulating charge reservoir block containing single or double Tl-O layers [110]. The superconducting properties like critical temperature, irreversibility field, critical current density and flux pinning in thallium-based compounds largely depend on the thickness of the insulating Tl-O layer and the strength of Josephson coupling between CuO_2 planes [23,49,50,53,111–115]. The presence of the Tl-O layers between the CuO_2 superconducting blocks yields anisotropy in the physical properties of these compounds. The anisotropy parameter is defined by $\gamma=\xi_{ab}/\xi_c$, $\gamma=\rho_c/\rho_{ab}$ or is the ratio of the effective carrier mass in the superconducting state. The anisotropy in these superconductors results in a shorter coherence length of cooper pairs along c direction as compared to the spacing between the CuO_2 layers which can reduce the critical current density and irreversibility field of these materials. The anisotropy parameter depends on the thickness of the insulating charge reservoir layer and the spacing between the individual CuO_2 planes, the Tl-based compounds with double Tl-O layers in the structure have large anisotropy as compared to the compounds with single Tl-O layer (γ=17 for (TlBi)-1212 and γ=104 for Tl-2212). The higher anisotropy degrades the superconducting properties in terms of lower technological critical temperature, $Z=T_c/\gamma^{1/2}$, critical current density J_c and irreversibility field, H_{irr}. The H_{irr} is an important physical quantity that characterizes a superconductor for its use in magnetic fields. The irreversibility field largely depends on the inter layer coupling strength [110].

$$H_{irr} \propto 1/\rho_c \times d_c$$

where d_c is the repeat distance of the structure along c direction and $\rho_c \propto \exp(d_i/d_o)$ d_i is the thickness of the insulating layer and do is the characteristic thickness of the material. The exponential dependence of H_{irr} on d_i shows that superconducting materials with large insulating spacing exhibit low irreversibility filed than the materials with smaller insulating spacing [53,116,117]. The irreversibility field 'H_{irr}' of Tl-1223 superconductor follows the sequence; H_{irr}(Tl-1223)>H_{irr}(Tl-2223/Tl-2212)> H_{irr}(Bi-2212) [116,117]. Figure 10 shows the comparison of irreversibility line of Tl-1223 and Tl-2223 superconductors and in Figure 11 the dependence of H_{irr} on the thickness of the unit cell along c-axis for different Tl-based compounds is shown. A higher irreversibility line is observed for Tl-1223 due to its lower anisotropy.

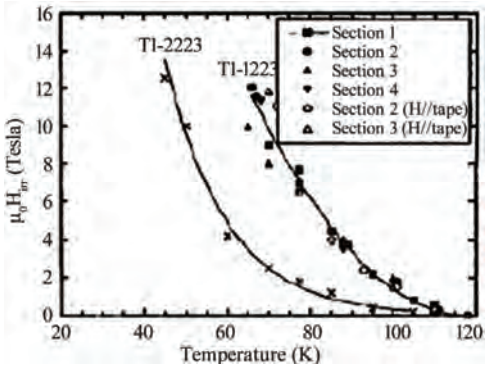

Figure 10. Comparison of irreversibility line of Tl-2223 and Tl-1223 superconductor [53]

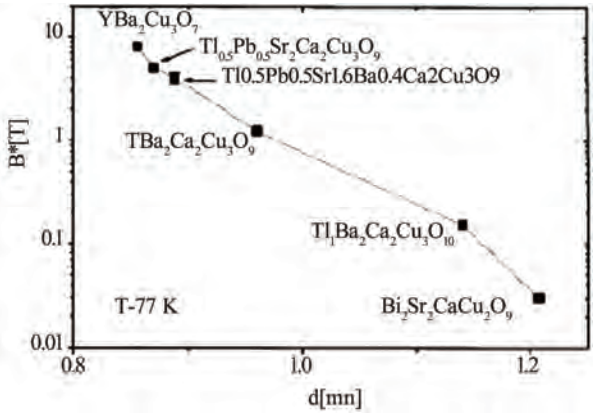

Figure 11. The irreversibility field versus thickness of charge reservoir block [52]

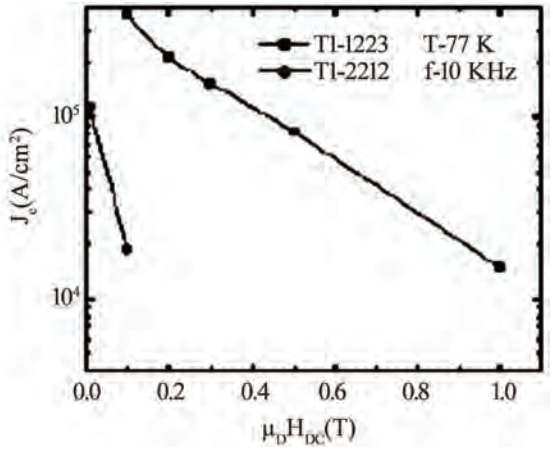

Figure 12. Dependence of critical current density of Tl-1223 and Tl-2212 superconductors on applied magnetic field [47]

The measured anisotropy parameter γ for Tl-1223 superconductors is 8 [53]. The interlayer coupling can also affect the critical current density of these superconductors. The Tl-1223 superconductors have been found to have higher J_c as compared to Tl-2212 and Tl-2223 compounds [47,49,50]. The Tl-1223 superconductors are very useful in electronic devices fabrication because the critical currents in these compounds decreases slowly as compared to double Tl-O layer compounds in the presence of external magnetic fields [47,55]. In Figure 12, a comparison of the magnetic field dependence of J_c(77K) of Tl-1223 and Tl-2212 is shown. The increase in the number of insulating layers in superconductors results in reduced Josephson coupling between conducting CuO_2 planes along the c-axis, which decreases the critical current density. The reduced interlayer coupling in double Tl-O layer compounds results in a shorter coherence length of cooper pairs along c-axis and hence the inferior superconducting properties. The small distance between Cu-O conducting planes may be the key to finding alternatives for attaining high critical current densities. Therefore, much attention is being given to Tl-1223 superconductors because they offer stronger interlayer coupling along c direction [48]. The coupling between CuO_2 planes of Tl-1223 compound can further be improved by replacing Ba by Sr and Tl by Pb or by the application of the external pressure which will be helpful in enhancing its superconducting properties [25,76].

4. $CuBa_2Ca_{n-1}Cu_nO_{2n+4}$ Superconductors

As the stronger coupling between CuO_2 planes lowers the anisotropy in high temperature superconductors and in turn enhances their superconducting properties i.e. $T_c(0)$, J_c and H_{irr}, any superconducting material having these properties will be very useful from application point of view. In the previous sections we have seen that the Tl-1223 superconductor has least anisotropy and higher $T_c(0)$ among all members of single Tl-O layer compounds, but the toxicity of Tl hinders their use in wide verity of applications. Therefore, the search for a superconductor material with low anisotropy and higher critical temperature was not stopped. A new family of superconductor materials, $CuBa_2Ca_{n-1}Cu_nO_{2n+2}$($n$=1,2,3…) [Cu-12($n$-1)$n$] prepared under high pressure (4-6 GPa), is thought to be the most promising due to its higher critical temperature and critical current density [118–124]. The members of Cu-12(n-1)n family has the same tetragonal structure as Tl-12(n-1)n compounds have copper in their charge reservoir layer, $CuBa_2O4_{n+\delta}$. Since copper is good conductor, therefore, the conducting charge reservoir layer of these compounds makes them least anisotropic as oppose to Tl-based superconductors. The members of Cu-based superconductors follow the formula Cu-12(n-1)n with n denoting the number of conducting CuO_2 planes; the higher number of CuO_2 planes are thought to have higher $T_c(0)$ since the optimum valency of copper for higher critical temperature is suggested to be z=2.33. The maximum increase of critical temperature is theoretically predicted for phase with n=11 [124]. The relationship between valence state z of copper and number of CuO_2 layers follows following empirical rule $z=2+4/(n+1)$ Among all the superconducting phases in this family the highest critical temperature is achieved in a phase with n=3 phase, Cu-1223 ($T_c(0)$~120K); in four CuO_2 plane Cu-based superconductor (Cu-1234) $T_c(0)$ is around 18K. These two compounds have least anisotropy (γ=5 and 1.6 respectively) and long coherence length along c-axis [123–126]. The high-pressure synthesis of these compounds is not economically viable but by introducing thallium (which acts as structure stabilizer and reaction rate accelerator) into the charge reservoir layer, the superconductor phases can easily be obtained by normal pressure synthesis. The substitution of Tl in Cu-12(n-1)n compounds results in emergence of a new subfamily $Cu_{1-x}Tl_x$-12(n-1)n which is the close derivative of these compounds. These com-

pounds are prepared under high as well as normal pressure and have superconducting properties very close to Cu-based compounds [124,127–130]. The members of this family have semi insulating charge reservoir layer $Cu_{1-x}Tl_xBa_2O_{4n-\delta}$ which slightly increases the anisotropy but their anisotropy remains lower than that of Tl-based compounds. A comparison of the anisotropy parameter and technological critical temperature for superconductors of different families is shown in Figure 13. The $Cu_{1-x}Tl_xBa_2Ca_2Cu_3O_{10-\delta}$ ($Cu_{1-x}Tl_x$-1223) superconductor of this family has higher critical temperature and critical current density [125]. This compound with anisotropy parameter (γ=5) has $Cu_{1-x}Tl_xBa_2O_{4-\delta}$ charge reservoir layer and three CuO_2 planes [131]. The c-axis length of $Cu_{1-x}Tl_x$-1223 is 15.89Å, which, lies between 14.79Å and 15.93Å of Cu-1223 and Tl-1223 superconductors [125]. The $Cu_{1-x}Tl_x$-1223 superconductor has been prepared both in the form of thin films and bulk samples [114–133]. The thin films of this compound have critical current density of the order of 10^7 A/cm^2 (77K, 0T) and 105 A/cm^2 (77K, 10T) [132]. The superconducting properties of $Cu_{1-x}Tl_x$-1223 can further be enhanced by post-annealing and substitution of different cations [125,128,134–138]. The $T_c(0)$ of this material increases by self-doping mechanism when post-annealed in nitrogen atmosphere. The self-doping mechanism is completed by the reduction of Tl^{+3} to Tl^{+1} via Tl^{+2}, Figure 14 [139–141].

Since the superconductivity is brought about by the carriers in conducting CuO_2 planes, therefore, the interplanar coupling plays an important role in bringing about the improved superconducting properties. One approach to enhance the interplaner correlation is to reduce the spacing between CuO_2 planes by replacing Ca with smaller sized ion. Magnesium (Mg) or Beryllium (Be) ions due to their smaller ionic radii as compared to Ca seems to be effective in bringing about such improved coupling possible The substitution of Mg or Be ion at Ca

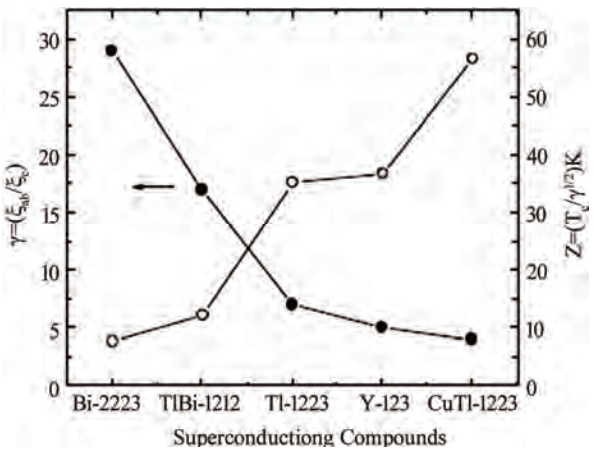

Figure 13. Comparison of anisotropy and technological critical temperature of different superconductors [126]

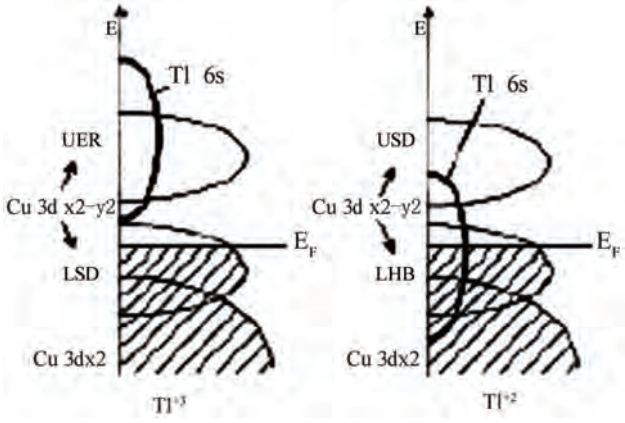

Figure 14. The energy level diagram of Tl6s level in $Cu_{1-x}Tl_x$-1223 superconductor before and after post-annealing in nitrogen [141]

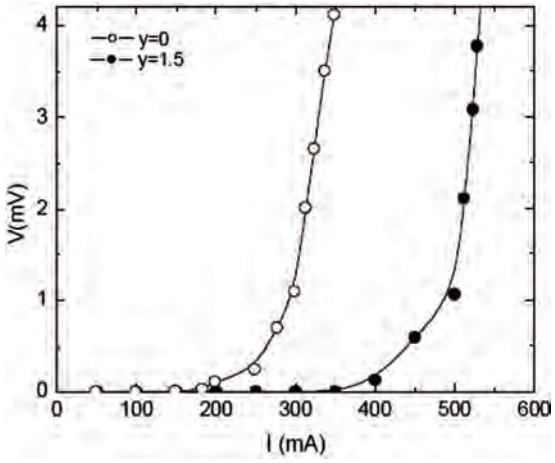

Figure 15. IV characteristics of $Cu_{0.5}Tl_{0.5}Ba_2Ca_{2-y}Mg_y$ $Cu_3O_{10-\delta}$ (y=0, 1.5) superconductor [142]

sites results in a material with highly correlated CuO_2 planes. The Fermi wave vector [$k_F=(3\pi^2N/V)^{1/3}$] depends on the volume of the unit cell therefore the decrease of the volume of unit cell with Mg/Be substitution increases k_F. The coherence length along c-axis [$\xi_c=\hbar\, k_F/m2\,\Delta$] is also increased, which decreases the anisotropy of the final compound [134–138]. The superconducting properties are improved ($T_c(0)$ and $J_c(H=0)$ increases) by substituting Mg or Be at Ca site in $Cu_{1-x}Tl_x$-1223. Figure 15 shows the increase of critical current of $Cu_{1-x}Tl_x$-1223 superconductor prepared at normal pressure by substituting Mg at Ca site; it has also enhanced the intergrain coupling witnessed from AC susceptibility measurements [142]. The variation of peak temperature T_P with applied DC magnetic field in χ' part of AC susceptibility shows an enhanced inter-grain coupling, Figure 16. On the other hand when Nb with higher electronegativity as compared to Mg and Be is substituted in $Cu_{1-x}Tl_x$-1223 superconductor at Ca site the $T_c(0)$ first increases and then de-

creases with the increase of Nb content. Similarly a decrease in magnitude of diamagnetism is observed with the increase of Nb concentration, Figure 17. The source of decrease in diamagnetism is the decreased density of carriers in conducting CuO_2 planes [143]. But when Pr is substituted at Ca sites the critical temperature decreases with the increased Pr contents. Since Pr has larger ionic radius oppose to Ca, it reduces the overlap of the cooper pair wave function in the two CuO_2 planes and therefore, reduces the interplaner coupling and increases anisotropy which results in lowering of $T_c(0)$ [138]. There is another member of Cu-12(*n*-1)*n* family which has carbon instead of Tl in the charge reservoir layer. The *n*=3 member of this family (Cu,C)-1223 has higher critical temperature and low anisotropy [144]. The critical temperature of this compound is 120K and lattice parameters a=3.862Å and c=14.80Å which are comparable to that of Cu-1223 superconductors [144,145]. But (Cu,C)-1223 does not have

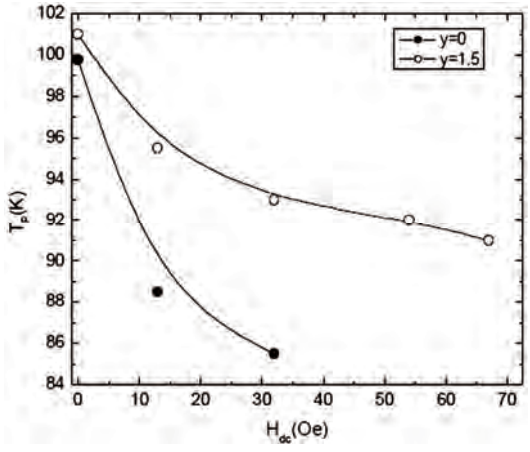

Figure 16. The peak temperature 'T_P' of // versus H_{dc} of $Cu_{0.5}Tl_{0.5}Ba_2Ca_{2-y}Mg_yCu_3O_{10-\delta}$(y=0, 1.5) superconductor [142]

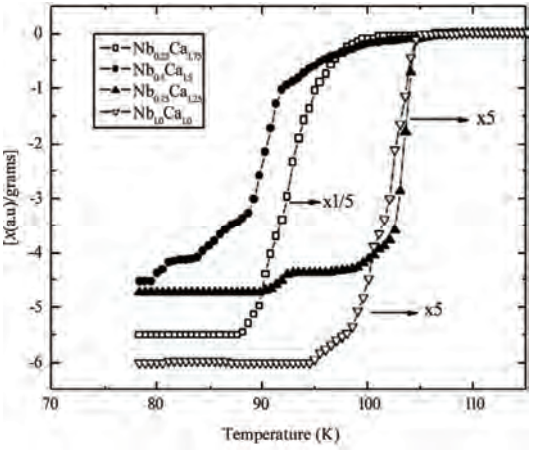

Figure 17. AC-susceptibility as a function of temperature of $Cu_{0.5}Tl_{0.5}Ba_2Ca_{2-y}Nb_yCu_3O_{10-\delta}$ (y=0.25, 0.5, 0.75, 1.0) superconductor samples [143]

the ability of significant $T_c(0)$ enhancement by self doping [146] because it has carbon in the charge reservoir layer in contrast to $Cu_{1-x}Tl_x$-1223 in which change of state of thallium promotes the optimum holes doping in CuO_2 planes.

5. Conclusions

It is concluded from the above detailed review of Tl-12(*n*-1)*n* and Cu-12(*n*-1)*n* compounds that the superconductors of these two families have low anisotropy as compared to other cuprate families. These compounds due to their lower anisotropy have the ability to carry very high current densities of the order of 104-106 A/cm^2 in applied magnetic fields and have got potential in device fabrication. In both these families the higher critical temperature is achieved in a compound with *n*=3 member. The Cu-1223has lower anisotropy than that of Tl-1223 but its preparation is possible only under high pressure (4GPa). The high pressure synthesis hinders the preparation of this compound for large scale applications. But the substitution of thallium at the copper site in the charge reservoir layer of Cu-1223 results in a new compound CuTl-1223, which has low anisotropy, higher critical temperature and critical current density. The substitution of thallium makes it possible to prepare this compound at normal pressure. We have also seen that the anisotropy of these compounds can be lowered by increasing the coupling between the CuO_2 planes. The increased inter-plane coupling is achieved by substituting smaller sized elements at Ca site, such as Mg and Be. This review article would be useful in the understanding and synthesis of new superconductors with low anisotropy and would help to enhance their superconducting properties.

REFERENCES

[1] Z. Z. Sheng and A. M. Hermann, Nature, Vol. 332, pp. 55, 1988.

[2] Z. Z. Sheng, A. M. Hermann, A. E. Ali, C. Almasan, J. Estrada, T. Datta, and R. J. Matson, Phys. Rev. Lett., Vol. 60, pp. 937, 1988.

[3] Z. Z. Sheng and A. M. Hermann, Nature, Vol. 332, pp. 138, 1988.

[4] Graziella Malandrino, Darrin S. Richeson, Tobin J. Marks, Donald C. De Groot, Jon L. Schindler, and Carl R. Kannewurf, Appl. Phys. Lett., Vol. 58, pp. 182, 1991.

[5] M. L. Chu, H. L. Chang, C. Wang, J. Y. Juang, T. M. Uen, and Y. S. Gou, Appl. Phys. Lett., Vol. 59, pp. 1123, 1991.

[6] W. L. Oslon, M. M. Eddy, T. W. James, R. B. Hammond, G. Gruner, and L. Drabeck, Appl. Phys. Lett., Vol. 55, pp. 188, 1989.

[7] M. Kikuchi, T. Kajitani, T. Suzuki, S. Nakajima, K. Hiraga, N. Kobayashi, H. Iwasaki, Y. Syono, and Y. Muto, Jpn. J. Appl. Phys., Vol. 28, pp. L382, 1989.

[8] S. S. P. Parkin, V. Y. Lee, E. M. Engler, A. I. Nazzal, T. C. Huang, G. Gormau, R. Savoy, and R. Beyer, Phys. Rev.

Lett., Vol. 60, pp. 2539, 1988.

[9] I. K. Schuller and J. D. Jorgensen, Mater. Res. Bull. XIV, pp. 27, 1989.

[10] A. W. Sleight, M. A. Subramanian, and C. C. Torardi, Mater. Res. Bull. XIV, pp. 45, 1989.

[11] C. Martin, C. Michel, A. Maignan, M. Hervieu, and B. Raveau, C. R. Acad. Sci. Ser.2, Vol. 307, pp. 27, 1988.

[12] Chan Park and Robert L. Synder, J. Am. Ceram. Soc., Vol. 78, pp. 3171, 1995.

[13] J. B. Parise, J. Gopalkrishnan, M. A. Subramanian, and A. W. Sleight, J. Solid State Chem., Vol. 76, pp. 432, 1988.

[14] Y. Tang, B. Lin, D. Zhou, W. Zhu, F. Chen, N. Li, K. Chen, and G. Lu, Mod. Phys. Lett. B, Vol. 3, pp. 853, 1989.

[15] D. S. Ginley, J. F. Kwak, R. P. Hellmer, R. J. Baughman, E. L. Venturini, M. A. Mitchell, and B. Morosin, Physica C, Vol. 156, pp. 592, 1988.

[16] W. L. Olson, M. M. Eddy, T. W. James, R. B. Hammond, G. Gruner, and L. Drabeck, Appl. Phys. Lett., Vol. 55, pp. 188, 1989.

[17] W. Y. Lee, V. Y. Lee, J. Salem, T. C. Huang, R. Savoy, D. C. Bullock, and S. S. P. Parkin, Appl. Phys. Lett., Vol. 53, pp. 329, 1988.

[18] D. S. Ginley, J. F. Kwak, R. P. Hellmer, R. J. Baughman, E. L. Venturini, and B. Morosin, Appl. Phys. Lett., Vol. 53, pp. 406, 1988.

[19] K. K. Verma, G. D. Verma, R. S. Tiwari, and O. N. Srivastava, Jpn. J. Appl. Phys., Vol. 29, pp. L880, 1990.

[20] W. Y. Lee, J. Salem, V. Lee, D. Deline, T. C. Huang, R. Savoy, J. Duran, and R. L. Sandstrom, Physica C, Vol. 160, pp. 5117, 1989.

[21] H. L. Chang, C. Wang, M. L. Chu, T. M. Uen, and Y. S. Gou, Jpn. J. Appl. Phys., Vol. 28, pp. L631, 1989.

[22] H. S. Koo, W. M. Hurng, W. H. Lee, T. Y. Tseng, M. Chen, and J. R. Lo, Appl. Phys. Lett., Vol. 62, pp. 3354, 1993.

[23] D. Thopart, J. Hejtmanek, D. Pelloquin, C. Martin, and A. Maignan, Physica C, Vol. 336, pp. 143, 2000.

[24] Z. Zhang, C. C. Chen, C. M. Lieber, B. Morosin, D. S. Ginley, and E. L. Venturini, Phys. Rev. B, Vol. 45, pp. 987, 1992.

[25] D. T. Jover, R. J. Wijngaarden, R. Griessen, E. M. Haines, J. L. Tallon, and R. S. Liu, Phys. Rev. Lett., Vol. 54, pp. 10175, 1996.

[26] Ph. Galez, Th. Hopfinger, J. L. Soubeyroux, M. Lomello-Tafin, Ch. Opagiste, Ch. Bertrand, and J. L. Jorda, Physica C, Vol. 372, pp. 1137, 2002.

[27] S. H. Liou and C. Y. Wu, Appl. Phys. Lett., Vol. 60, pp. 2803, 1992.

[28] S. Matsuda, S. Takeuchi, A. Soeta, T. Suzuki, K. Aihara, and T. Kamo, Jpn. J. Appl. Phys., Vol. 27, pp. 2062, 1988.

[29] T. S. Kayed, Cryst. Res. Technol., Vol. 38, pp. 946, 2003.

[30] A. Soeta, T. Suzuki, S. Takeuchi, T. Kamo, K. Usami, and S. Matsuda, Jpn. J. Appl. Phys., Vol. 28, pp. L1186, 1989.

[31] S. N. Bhatia, P. Chowdhury, S. Gupta, and B. D. Padalia, Phys. Rev. B, Vol. 66, pp. 214523, 2002.

[32] Z. Z. Sheng, L. Sheng, H. M. Su, and A. M. Hermann, Appl. Phys. Lett., Vol. 53, pp. 2686, 1988.

[33] R. M. Hazen, L. W. Finger, R. J. Angel, C. T. Prewitt, N. L. Ross, C. G. Hadidiacos, P. J. Heaney, D. R. Veblen, Z. Z. Sheng, A. El Ali, and A. M. Hermann, Phys. Rev. Lett., Vol. 60, pp. 1657, 1988.

[34] F. Goutenoire, A. Maignan, G. Van Tendello, C. Martin, C. Michel, M. Hervieu, and B. Raveau, Solid State Commun., Vol. 90, pp. 47, 1994.

[35] A. Poddar, B. Bandyopadhyay, and B. Chattopadhyay, Physica C, Vol. 390, pp. 120, 2003.

[36] Y. Idemoto, M. Matsuzawa, N. Koura, K. Takeuchi, J. W. Richardson Jr., and Chun- K. Loong, Solid State Commun., Vol. 131, pp. 513, 2004.

[37] T. Tatsuki, A. Tokiwa-Yamamoto, T. Tamura, X. J. Wu, Y. Moriwaki, S. Adachi, and K. Tanabe, Physica C, Vol. 273, pp. 65, 1996.

[38] Y. X. Jia, C. S. Lee, and A. Zettl, Physica C, Vol. 234, pp. 24, 1994.

[39] C. Y. Huang, H. H. Tai, and M. K. Wu, Mod. Phys. Lett. B, Vol. 3, pp. 525, 1989.

[40] M. Yang, Y. H. Kao, Y. Kin, and K. W. Wong, Phys. Rev. B, Vol. 50, pp. 13653, 1994.

[41] A. Podder, P. Mandal, A. N. Das, and B. Ghosh, Phys. Rev. B, Vol. 44, pp. 2757, 1991.

[42] Misra, Y. Song, P. P. Crooker, J. R. Gaines, and A. H. Cardona, Appl. Phys. Lett., Vol. 59, pp. 863, 1991.

[43] P. Bramley, S. M. Morley, C. R. M. Grovenor, and B. Pecz, Appl. Phys. Lett., Vol. 66, pp. 517, 1995.

[44] D. Weaver, M. E. Reeves, G. P. Summers, and R. J. Soulen, Appl. Phys. Lett., Vol. 63, pp. 252, 1993.

[45] W. L. Holstein, L. A. Parisi, D. W. Face, X. D. Wu, S. R. Foltyn, and R. E. Muenchausen, Appl. Phys. Lett., Vol. 66, pp. 517, 1995.

[46] A. H. Cardona, H. Suzuki, T. Yamashita, K. H. Young, and L. C. Bourne, Appl. Phys. Lett., Vol. 62, pp. 411, 1993.

[47] Sundaresan, H. Asada, A. Crisan, J. C. Nie, H. Kito, A. Iyo, Y. Tanaka, M. Kusunoki, and S. Ohshima, IEEE Trans. Appl. Supercond., Vol. 13, pp. 2913, 2003.

[48] J. Miller, J. G. Hu, J. D. Hettinger, K. E. Gray, J. E. Tkaczyk, J. Deluca, P. L. Karas, J. A. Sutliff, and M. F. Garauskas, Appl. Phys. Lett., Vol. 63, pp. 556, 1993.

[49] J. Y. Juang, J. H. Horng, S. P. Chen, C. M. Fu, K. H. Wu, T. M. Uen, and Y. S. Gou, Appl. Phys. Lett., Vol. 60, pp. 885, 1995.

[50] A. Sundaresan, H. Asada, A. Crisan, J. C. Nie, H. Kito, A. Iyo, T. Tanaka, M. Kusunoki, and S. Oshima, Physica C, Vol. 388, pp. 473, 2003.

[51] Iyo, Y. Ishiura, Y. Tanaka, P. Badica, K. Tokiwa, T. Watanabe, and H. Ihara, Physica C, Vol. 370, pp. 205, 2002.

[52] W. Mexner, J. Hoffmann, S. Heede, K. Heinemann, H. C. Freyhardt, F. Ladenberger, and E. Schwarzmann, Z. Phys. B, Vol. 101, pp. 181, 1996.

[53] N. Zheng, J. D. Johnson, A. R. Jones, A. M. Campbell, W.

Y. Liang, T. Doi, M. Okada, and K. Higashyama, J. Appl. Phys., Vol. 77, pp. 5287, 1995.

[54] R. T. Liu, S. L. Yan, L. Fang, and M. He, Supercond. Sci. Technol., Vol. 14, pp. 948, 2001.

[55] R. S. Liu, D. N. Zheng, J. W. Loram, K. A. Mirza, A. M. Campbell, and P. P. Edwards, Appl. Phys. Lett., Vol. 60, pp. 1019, 1992.

[56] T. Jover, H. Wilhelm, R. J. Wijngarden, and R. S. Liu, Phys. Rev. B, Vol. 55, pp. 11832, 1997.

[57] R. S. Liu, P. P. Edwards, Y. T. Huang, S. F. Wu, and P. T. Wu, J. Solid State Chem., Vol. 86, pp. 334, 1990.

[58] R. S. Liu and P. P. Edwards, Physica C, Vol. 185, pp. 655, 1991.

[59] R. Abd-Shukor, B. Yatim, and R. S. L. Lau, J. Mater. Sci. Lett., Vol. 16, pp. 818, 1997.

[60] R. Abd-Shukor and K. S. Tee, J. Mater. Sci. Lett., Vol. 17, pp. 103, 1997.

[61] R. Abd-Shukor and N. A. N. Jaffar, J. Mater. Sci., Vol. 10, pp. 677, 1999.

[62] M. P. Siegal, E. L. Venturini, P. P. Newcomer, B. Morosin, D. L. Overmyer, F. Dominguez, and R. Dunn, Appl. Phys. Lett., Vol. 67, pp. 3966, 1995.

[63] H. Kotegawa, Y. Tokunga, K. Ishida, G. Q. Zheng, Y. Kitwka, A. Iyo, Y. Tanaka, and H. Ihara, Phys. Rev. B, Vol. 65, pp. 18504, 2002.

[64] H. Yamauchi and M. Karppinen, J. Supercond., Vol. 11, pp. 43, 1998.

[65] A. Iyo, Y. Aizawa, Y. Tanaka, M. Tokumoto, K. Tokiwa, T. Watanabe, and H. Ihara, Physica C, Vol. 357, pp. 324, 2001.

[66] O. Heiml, G. Gritzner, S. Tonies, H. W. Weber, J. Keckes, and B. Ortner, Supercond. Sci. Technol., Vol. 15, pp. 1592, 2002.

[67] R. E. Gladyshevskii, E. Bellingeri, F. Marti, and R. Flukiger, J. Supercond., Vol. 11, pp. 109, 1998.

[68] M. Paranthaman, J. R. Thompson, A. Goyal, A. J. Pedraza, and M.Kroeger, Appl. Phys. Lett., Vol. 67, pp. 294, 1995.

[69] A. M. Panich, S. D. Goren, L. Frenkel Ben-Yakar, M. Eder, and G. Gritzner, Physica C, Vol. 356, pp. 129, 2001.

[70] Hase, N. Hamada, A. Iyo, N. Terada, Y. Tanaka, and H. Ihara, Physica C, Vol. 357, pp. 153, 2001.

[71] L. P. Cook, W. Wong-Ng, and P. Paranthaman, J. Res. Natl. Inst. Stand. Technol., Vol. 101, pp. 675, 1996.

[72] T. Kaneko, T. Wada, H. Yamauchi, and S. Tanaka, Appl. Phys. Lett., Vol. 56, pp. 1281, 1990.

[73] A. Kikuchi, K. Inoue, and Tachikawa, Physica C, Vol. 337, pp. 180, 2000.

[74] Z. F. Rent and J. H. Wang, Appl. Phys. Lett., Vol. 61, pp. 1715, 1992.

[75] Chiang, C. Y. Shei, S. F. Wu, and Y. T. Huang, Appl. Phys. Lett., Vol. 58, pp. 2435, 1991.

[76] S. Adachi, T. Shibata, T. Tatsuki, T. Tamura, K. Tanabe, S. Fujihara, and T. Kimura, Physica C, Vol. 324, pp. 15, 1995.

[77] W. Konig, M. Mair, and G. Gritzner, J. Supercond., Vol. 11, pp. 107, 1998.

[78] Y. T. Huang, S. F. Wu, C. K. Chiang, and W. H. Lee, Appl. Phys. Lett., Vol. 57, pp. 2354, 1991.

[79] M. Enengl, E. Kuzmann, Z. Homonnay, and G. Gritzner, Physica C, Vol. 377, pp. 565, 2002.

[80] T. Kamo, T. Toi, A. Soeta, T. Yuasa, N. Inoue, K. Aihara, and S. Matsuda, Appl. Phys. Lett., Vol. 59, pp. 3186, 199.

[81] T. Doi, T. Nabatame, T. Kamo, and S. P. Matsuda, Supercond. Sci. Technol., Vol. 4, pp. 488, 1991.

[82] R. Zalecki, A. Kolodziejczyk, J. Chmist, W. Konig, and G. Gritzner, Physica C, Vol. 341, pp. 2049, 2000.

[83] S. Matsuda, S. Takeuchi, A. Soeta, T. Suzuki, K. Aihara, and T. Kamo, Jpn. J. Appl. Phys., Vol. 27, pp. 2062, 1988.

[84] R. J. McNeely, J. A. Belot, B. J. Hinds, T. J. Marks, J. L. Schindler, X. F. Zhang, and D. J. Miller, Appl. Phys. Lett., Vol. 71, pp. 1243, 1997.

[85] T. L. Aselage, E. L. Venturini, and S. B. Van Deusen, J. Appl. Phys., Vol. 75, pp. 1023, 1994.

[86] T. L. Aselage, E. L. Venturini, S. B. Van Deusen, T. J. Headley, M. O. Eatough, and J. A. Voigt, Physica C, Vol. 203, pp. 25, 1992.

[87] Oshima, T. Atou, M. Kikuchi, and Y. Syono, Physica C, Vol. 282, pp. 827, 1997.

[88] A. Iyo, Y. Tanaka, Y. Ishiura, M. Tokumoto, K. Tokiwa, T. Watanabe, and H. Ihara, Supercond. Sci. Technol., Vol. 14, pp. 504, 2001.

[89] J. L. Gonzalez, E. V. L. de Mello, E. S. Yugue, M. T. D. Orlando, and E. Baggio-Saitovitch, Physica C, Vol. 384, pp. 102, 2003.

[90] Y. S. Sung, X. F. Zhang, P. J. Kostic, and D. J. Miller, Appl. Phys. Lett., Vol. 69, pp. 3420, 1996.

[91] A. Kikuchi, T. Kinosita, N. Nishikawa, S. Komiya, and K. Tachikawa, Jpn. J. Appl. Phys., Vol. 27, pp. L167, 1995.

[92] M. Engel and G. Gritzner, Supercond. Sci. Technol., Vol. 16, pp. 956, 2003.

[93] N. M. Hamdan, Kh. A. Ziq, and A. S. Al-Harthi, Physica C, Vol. 314, pp. 125, 1999.

[94] Th. Hofinger, M. Lomello-Tafin, J. L. Jorda, Ph. Galez, M. Couach, R. E. Gladyshevskii, and J. L. Soubeyroux, Physica C, Vol. 351, pp. 53, 2001.

[95] M. H. Eder and G. Gritzner, Supercond. Sci. Technol., Vol. 18, pp. 87, 2005.

[96] A. I. Abou-Aly, I. H. Ibrahim, and R. Awad, J. Mater. Sci., Vol. 35, pp. 2893, 2000.

[97] A. I. Abou-Aly, R. Awad, and N. H. Mohammad, J. Mag. & Magnetic Materials, Vol. 226, pp. 328, 2001.

[98] Gritzner, M. Eder, A. Cigan, J. Manka, G. Plesch, and V. Zrubec, Physica C, Vol. 366, pp. 169, 2002.

[99] E. Kuzmann, M. Mair, Z. Klencar, A. Vertes, Z. Homonnay, and G. Gritzner, Physica C, Vol. 319, pp. 12, 1999.

[100] N. M. Hamdan and J. Low Temp. Phys., Vol. 117, pp. 1187, 1999.

[101] S. Isber, R. Awad, A. I. Abou-Aly, M. Tabbal, and J. M. Kaouar, Supercond. Sci. Technol., Vol. 18, pp. 311, 2005.

[102] M. Enengl, E. Kuzmann, Z. Homonnay, and G. Gritzner, Physica C, Vol. 377, pp. 565, 2002.

[103] Y. Li, E. Baggio-Saitovitch, Y. B. Wang, G. H. Cao, N. Chen, Z. X. Zhao, and L. Wei, Physica C, Vol. 315, pp. 129, 1999.

[104] M. Kubberger and G. Gritzner, Physica C, Vol. 390, pp. 263, 2003.

[105] R. Awad, N. S. Aly, I. H. Ibrahim, A. I. Abou-Aly, and A. I. Saad, Physica C, Vol. 341, pp. 685, 2000.

[106] W. L. Holstein, L. A. Parisi, C. Wilker, and R. B. Flippen, Appl. Phys. Lett., Vol. 60, pp. 2014, 1992.

[107] K. F. Renk and G. Saemann-Ischenko, Appl. Phys. Lett., Vol. 65, pp. 1451, 1994.

[108] Chou, H. S. Chen, A. R. Kortan, L. C. Kimerling, F. Thiel, and M. K. Wu, Appl. Phys. Lett., Vol. 58, pp. 2836, 1991.

[109] A. Piehler, R. Low, J. Betz, R. Schonberger, and K. F. Renk, J. Appl. Phys., Vol. 74, pp. 6437, 1993.

[110] V. handy, A. Maignan, C. Martin, F. Warmont, and J. Provost, Phys. Rev. B, Vol. 56, pp. 130, 1997.

[111] P. Marsh, R. M. Fleming, M. L. Mandich, A. M. Desantolo, J. Kwo, M. Hong, and L. J. Martines-Miranda, Nature, Vol. 334, pp. 141, 1988.

[112] Mihailovic, T. Mertelj, K. F. Voss, A. J. Heeger, and N. Herron, Phys. Rev. B, Vol. 45, pp. 8016, 1992.

[113] Scherbel, M. Mans, H. Schneidenind, U. Kaiser, J. Biskupek, F. Schmidl, and P. Seidel, Phys. Rev. B, Vol. 70, pp. 104507, 2004.

[114] T. Nabatame, S. Koike, O. B. Hyun, I. Hirabayashi, H. Suhara, and K. Nakamura, Appl. Phys. Lett., Vol. 65, pp. 776, 1994.

[115] H. Takei, H. Kugai, Y. Torii, and K. Tada, Physica C, Vol. 210, pp. 109, 1993.

[116] T. Nabatame, J. Sato, Y. Saito, K. Aihara, T. Kamo, and S. Matsuda, Physica C, Vol. 193, pp. 39, 1992.

[117] M. Paranthaman, M. Foldeaki, R. Tello, and A. M. Hermann, Physica C, Vol. 219, pp. 413, 1994.

[118] Q. Jin, S. Adachi, X. J. Wu, H. Yamauchi, and S. Tanaka, Physica C, Vol. 223, pp. 238, 1994.

[119] X. J. Wu, S. Adachi, C. Q. Jin, H. Yamauchi, and S. Tanaka, Physica C, Vol. 223, pp. 243, 1994.

[120] X. J. Wu, C. Q. Jin, S. Adachi, and H. Yamauchi, Physica C, Vol. 224, pp. 175, 1994.

[121] H. Ihara, Adv. Supercond., Vol. 7, pp. 255, 1995.

[122] H. Ihara, Solid State Phys., Vol. 35, pp. 301, 2001.

[123] M. Karppinen, H. Yamauchi, Y. Morita, M. Kitabatake, T. Motohashi, R. S. Liu, J. M. Lee, and J. M. Chen, Journal of Solid State Chemistry, Vol. 177, pp. 1037, 2004.

[124] H. Ihara, K. Tokiwa, H. Ozawa, M. Hirabayashi, A. Negishi, H. Matuhata, and Y. S. Song, Jpn. J. Appl. Phys., Vol. 33, pp. L503, 1994.

[125] H. Ihara, K. Tanaka, Y. Tanaka, A. Iyo, N. Terada, M. Tokumoto, M. Ariyama, I. Hase, A. Sundaresan, N. Hamada, S. Miyashita, K. Tokiwa, and T. Watanabe, Physica C, Vol. 341, pp. 487, 2000.

[126] H. Ihara, Physica C, Vol. 364, pp. 289, 2001.

[127] Tokiwa, H. Aota, C. Kunugi, K. Tanaka, Y. Tanaka, A. Iyo, H. Ihara, and T. Watanabe, Physica B, Vol. 284, pp. 1077, 2000.

[128] Tanaka, A. Iyo, N. Terada, K. Tokiwa, S. Miyashita, Y. Tanaka, T. Tsukamoto, S. K. Agarwal, T. Watanabe, and H. Ihara, Phys. Rev. B, Vol. 63, pp. 064508, 2001.

[129] T. Shibata, T. Tatsucki, S. Adachi, K. Tanabe, S. Fujihara, and T. Kimura, Physica C, Vol. 353, pp. 200, 2001.

[130] Nawazish A. Khan, Y. Sekita, H. Ihara, and A. Maqsood, Physica C, Vol. 377, pp. 43, 2002.

[131] Tanaka, A. Iyo, Y. Tanaka, K. Tokiwa, M. Tokumoto, M. Ariyama, T. Tsukamoto, T. Watanabe, and H. Ihara, Physica B, Vol. 284, pp. 1081, 2001.

[132] H. Ihara, Y. Sekita, F. Tateai, N. A. Khan, K. Ishida, E. Harashima, T. Kojima, H. Yamamoto, K. Tanaka, Y. Tanaka, N. Terada, and H. Obara, IEEE Trans. Appl. Supercond., Vol. 9, pp. 1551, 1999.

[133] A. Khan, Y. Sekita, F. Tateai, T. Kojima, K. Ishida, N. Terada, and H. Ihara, Physica C, Vol. 320, pp. 39, 1999.

[134] Nawazish A. Khan and A. A. Khurram, Appl. Phys. Lett., Vol. 86, pp. 152502, 2005.

[135] Nawazish A. Khan and Shahid Nawaz, IEEE Trans. Appl. Supercond., Vol. 16, pp. 1, 2006.

[136] S. K. Agarwal, A. Iyo, K. Tokiwa, Y. Tanaka, K. Tanaka, M. Tokumoto, N. Terada, T. Saya, M. Umeda and H. Ihara, Phys. Rev. B, Vol. 58, pp. 9504, 1998.

[137] Nawazish A. Khan and G. Husnain, Physica C, Vol. 436, pp. 51, 2006.

[138] Nawazish A. Khan, Asim Javaid, A. A. Khurram, and Naghma Haider, Physica C, Vol. 425, pp. 90, 2005.

[139] T. Watanabe, S. Miyashita, N. Ichioka, K. Tokiwa, K. Tanaka, A. Iyo, Y. Tanaka, and H. Ihara, Physica B, Vol. 284, pp. 1075, 2000.

[140] Terada, K. Tanaka, Y. Tanaka, A. Iyo, K. Tokiwa, T. Watanabe, and H. Ihara, Physica B, Vol. 284, pp. 1083, 2000.

[141] H. Ihara, K. Tanaka, Y. Tanaka, A. Iyo, N. Terada, M. Tokumoto, F. Tateai, M. Kawamura, K. Ishida, S. Miyashita, and T. Watanabe, Physica B, Vol. 284, pp. 1085, 2000.

[142] A. A. Khurram and Nawazish A. Khan, Supercond. Sci. Technol., Vol. 19, pp. 679, 2006.

[143] A. Khan and A. Hussain, Physica C, Vol. 449, pp. 21, 2006.

[144] T. Kawashima, Y. Matsui, and E. Takayama-Muromachi, Physica C, Vol. 224, pp. 69, 1994.

[145] H. Kito, A. Iyo, M. Hirai, A. Crisan, A. Tokumoto, S. Okayasu, M. Sasase, and H. Ihara, Physica C, Vol. 378, pp. 329, 2002.

[146] M. Hirai, A. Iyo, H. Kito, A. Crisan, K. Tokiwa, T. Watanabe, J. Arai, and Y. Tanaka, Physica C, Vol. 388, pp. 427, 2003.

J. Electromagnetic Analysis & Applications, 2010, 2: 75-81
doi:10.4236/jemaa.2010.22011 Published Online February 2010 (www.SciRP.org/journal/jemaa)

Static Electric-Spring and Nonlinear Oscillations

Haiduke Sarafian

University College, The Pennsylvania State University, York, USA.
Email: has2@psu.edu

Received October 13th, 2009; revised November 18th, 2009; accepted November 25th, 2009.

ABSTRACT

The author designed a family of nonlinear static electric-springs. The nonlinear oscillations of a massively charged particle under the influence of one such spring are studied. The equation of motion of the spring-mass system is highly nonlinear. Utilizing Mathematica [1] *the equation of motion is solved numerically. The kinematics of the particle namely, its position, velocity and acceleration as a function of time, are displayed in three separate phase diagrams. Energy of the oscillator is analyzed. The nonlinear motion of the charged particle is set into an actual three-dimensional setting and animated for a comprehensive understanding.*

***Keywords*:** *Static Electric-Spring, Nonlinear Oscillator, Mathematica*

1. Introduction

Analysis of the kinematics and dynamics of a mechanical spring-mass system is a classic physics problem [2]. In this analysis the spring is idealized; it is assumed the spring is mass-less and linear. The first assumption is "justified" when the mass of the object outweighs the spring. The linearity for a coiled-shaped spring for most of the time is enforced by not stretching the spring beyond its plastic limit. Under these assumptions the equation describing the motion of the object is a second order linear differential equation; it is trivially solved with analytic sinusoidal solutions. This scenario is modified slightly when a nonlinear mass-less spring is considered. For instance, some 90 years ago, Duffing [3] initiated the notion of the nonlinear vibrator. Accordingly, an equation is proposed to describe the state of one such oscillator. Duffing's equation is given by, $\ddot{x}+\alpha\dot{x}+\beta x+\gamma x^3 = f(t)$; where, in addition to the linear spring term, βx, a cubic term, γx^3, is used to characterize the non-linearity. Damping and the source of the forced oscillation terms are given by, $\alpha\dot{x}$, and $f(t)$, respectively. The notion of Duffing's initiated nonlinear vibrator has found its applications in a wide range of scientific fields. Reference [4] for instance has sections devoted to the description of the Duffing equation. The latter reference also contains a wealth of bibliographic listed related articles. Recently, an electronic website [5] posted an animated description of the Duffing related issues. However, neither these references nor the author's thorough literature search could identify a source describing the oscillations of an *ideal*/*perfect* mass-less mechanical vibrator. The article that "best" aligns with one such mechanical oscillation is a suggested experiment given in [6]. The authors of the latter reference have claimed their proposed experiment would produce data that is compatible with the description of the Duffing equation. However, a careful analysis of their setup and suggested analysis reveals the mass of the elastic metal strip is ignored. This leads to expect disconnect between the data and the proposed theory.

Motivated with identifying the missing practical design of mechanical oscillations of an *ideal/perfect* mass-less oscillator, the author designed a spring made of a static electric field, and called it an electric-spring. The point is a spring made of an electric field is a mass-less spring. In other words, there is no need to make assumptions justifying the smallness of the spring's mass. This makes the spring *ideal*. Furthermore, knowing the fact that the strength and the orientation of a static electric field is a function of the distribution of the static electric charge makes the number of the designs limitless. For the sake of transparency and simplicity, in this article we consider a circular charged ring with a uniform positive charge distribution. The field along the axis through the center of the ring and perpendicular to the plane of the ring sustains its direction; it orients itself along the symmetry axis heading outward from the center. The strength of the field however, varies as a function of distance from the center; interestingly, its variation is not linear. Placing a negatively charged particle along a horizontal frictionless axis of the ring exerts a force on the particle accelerating it toward the center of the ring. The particle sling shots through the center of the ring and slides to the opposite

side of it. On the other side of the ring because the field is reversed and reoriented, the particle decelerates and slides to a momentarily halt at a symmetrical opposite end. Since there is no loss of energy, continuous repetition of the movement is warranted and results in steady oscillations. The electric-spring in addition to being massless is nonlinear as well. Therefore, without idealizing the setup we are proposing a design resulting in perfect nonlinear oscillations. As mentioned earlier, in general, the shape of the nonlinear electric field is a function of shape of the configuration of the charge distribution. Hence, by replacing the ring with different geometrical shapes such as a square, a rectangle, an ellipse, an n-tagon, and etc. one may fabricate limitless practical nonlinear electric-springs.

This article is composed of seven sections. Section 1 addresses the introduction and motivations, Section 2 outlines the objectives. Section 3 deals with the analysis. Section 4 addresses the energy issues of the oscillations, Section 5 embodies the 3D animation and the accompanied *Mathematica* code, Section 6 describes the extended design features and Section 7, the last section, shares the conclusions and closing remarks.

2. Objectives

We begin with a positively charged ring of radius R. Assuming the ring is made of a conductor; its charge distribution is uniform. Along the symmetry axis of the ring, the electric field, intuitively and justifiably is oriented along the axis heading outward from the center extending on both sides of the ring. The field along the axis due to the symmetry of the ring is distance dependent only. For any off-axis point the field depends on other coordinates as well. Apply the superposition principal to the electric field for a point along the symmetry axis trivially calculates [7]:

$$E(x) = kQ\frac{x}{(R^2 + x^2)^{\frac{3}{2}}} \qquad (1)$$

We have assumed a right handed Cartesian coordinate system, and the ring is placed in the yz plane with the x axis stretching from left to right. The x is the distance from the center of the ring, Q is the charge on the ring and the value of $k=1/(4\pi\varepsilon_0) \equiv 9.0\times10^9$ in MKS units. A plot of $E/(kQ)$ for a 10 cm ring size is shown in Figure 1.

EfieldRing[x_]= $\frac{x}{(R^2+x^2)^{\frac{3}{2}}}$;

plotEfieldRing=Plot[EfieldRing[x]/.R→10×10^{-2},{x,-1,1}, PlotRange→All,PlotStyle→{Green,Thick},GridLines→ Automatic, AxesLabel→{"x(m)","E/(k Q)(1/m^2)"}]

Equation (1) is an asymmetric/odd function with respect to x. Its plot displayed in Figure 1 shows the field for

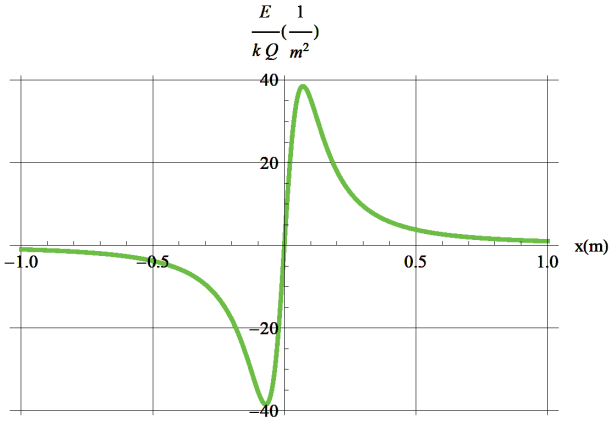

Figure 1. Display of E/(k Q) for a ring of radius R=10 cm along the symmetry axis vs. distance x from the center of the ring

x<0 is negative. This means the vector field $\vec{E}$ on both sides of the ring orients itself away from the center of the ring. The value of the electric field and its variation vs. distance indeed may be viewed as the characteristic of the electric force that would act on a charged particle if it were placed on the symmetry axis. Now we envision placing a negatively charged particle on the axis. Under the influence of such a nonlinear force the particle attractively accelerates toward the center of the ring. According to Figure 1, the electric field and therefore the electric force are entirely nonlinear. Its strength and magnitude varies quite differently vs. the strength of an idealized linear mechanical spring. For instance, one of the peculiar characteristics of the field as depicted in Figure 1 is its hump; at a certain distance from the center of the ring it becomes extremum. The abscissa of the latter is a function of the radius of the ring. These are:

dEfieldRing=D[EfieldRing[x],x]//Simplify;

Solve[dEfieldRing = = 0,x];{{x→-($\frac{R}{\sqrt{2}}$)},{x→ $\frac{R}{\sqrt{2}}$ }}

Therefore, one objectively may select a ring size, R, to control the position along the symmetry axis where the field is extremum and its impact is the maximum. We now utilize the field; we place a particle with a chosen mass and charge $\{m,q\}$ along the symmetry axis of the ring. The opposite "sign" of the charged particle, in our case study, a negative charge, experiences an attractive force toward the center of the ring. The electric force accelerates the particle. While sliding, it experiences a position-dependent and a variable nonlinear force. Assuming a frictionless slide, the particle makes it to the center of the ring. With its velocity at the center it slings shots to the opposite side. While sliding on the opposite side of the ring and because of the reoriented field the particle experiences a retarding position-dependent force,

decelerating it to a momentarily halt. The lack of friction preserves the energy of the particle, causing the movement to repeat itself endlessly. The particle therefore oscillates; however, because of the non-linearity of the imposed electric force the oscillation is nonlinear. The detailed analysis of the nonlinear oscillations along with related topics of interest follows.

3. Analysis

To form the equation describing the motion of the particle we begin with Newton's second law, $\vec{F}_{net} = m\vec{a}$. The particle is characterized with $\{m,q\}$. At any given time the electric force is the only effective force acting on the particle, $\vec{F}_{net} \equiv \vec{F}_q = q\vec{E}(x)$, where $E(x)$ is subject to Equation (1). Newton's law yields,

$$\ddot{x}(t) + \frac{kQq}{m}\frac{x(t)}{(R^2 + x^2(t))^{\frac{3}{2}}} = 0 \qquad (2)$$

The over-dot is defined as the derivative of the variable with respect to time, *t*. Equation (2) describes the motion of the particle. It is quite different from the classic equation describing the linear oscillations of a linear spring-mass system. It is a highly nonlinear differential equation. As we pointed out in the Introduction, historically, the Duffing equation is used as a pivotal equation describing the non-linear oscillations. A careful analysis of the force at hand reveals its masked correlation with the Duffing force. To unveil the correlation we expand the second term of Equation (2) about the center of the ring. Aside from the constant coefficient this gives:

Series[$\frac{x}{(R^2+x^2)^{\frac{3}{2}}}$,{x,0,8}]//PowerExpand

$x/R^3-(3\,x^3)/(2\,R^5)+(15\,x^5)/(8\,R^7)-(35\,x^7)/(16\,R^9)+O[x]^9$

This shows our proposed mass-less electric-spring is an upgraded description of the Duffing force. The first two terms of the expanded function is known to describe a "soft" spring [5]; and that limits the scope of the Duffing force. Simply put, the author's electric-spring is a superstructure version of the Duffing spring; *i.e.* its unexpanded function as it is used in Equation (2) embodies infinite odd powers of the compressed/elongated electric spring's length; plus it describes an *ideal/perfect* mass- less entity.

Now we go back to Equation (2). At the outset, it is known that the Duffing equation given in the introduction has no analytic solution. For our superstructure case too, we were not surprised failing to solve Equation (2) analytically. We deploy *Mathematica*, but it also fails to solve symbolically. Lastly, we supply a set of practical initial conditions and by utilizing *Mathematica* we seek for a numeric solution. The code leading the numeric solution, along with the relevant computed kinematic quantities such as position, velocity and acceleration i.e. $\{x(t), v(t), a(t)\}$, respectively are given. The output is displayed. For the ring and the particle we assumed $\{R,Q\}=\{10.\times10^{-2}\ m, 4.0\ nC\}$, and $\{m,q\}=\{10.\ mg,\ 3.0\ nC\}$, respectively,

```
values={k→ 9. 10^9,R→10. 10^-2,Q→4. 10^-9,m→10. 10^-6,
q→3. 10^-9};

eqn=x"[t]+((k Q q )/m  x[t]/(R^2+x[t]^2)^(3/2) )/.values;

soleqn=NDSolve[{eqn  = = 0,x[0]  8(R/.values),x'[0] = =
0},x[t],{t,0,50}];
{positionx,velocityx,accx}={x[t]/.soleqn,D[x[t]/.soleqn,
{t,1}],D[x[t]/.soleqn,{t,2}]};
plotx=Plot[positionx,{t,0,50},AxesLabel→{"t,s","x,m"},
PlotStyle→Thick, GridLines->Automatic];plotv=Plot[ve-
locityx,{t,0,50},AxesLabel→{"t,s","v,m/s"},PlotStyle→
Thick, GridLines->Automatic];
plota=Plot[accx,{t,0,50},AxesLabel→{"t,s","a,m/s^2"},Pl
otStyle→Thick, GridLines->Automatic];
Show[GraphicsArray[{plotx,plotv,plota}],ImageSize→
500]
```

The far left graph of Figure 2 indeed confirms our speculated intuitive expected oscillations.

The particle oscillates about the origin, *i.e.* the center of the ring. A trained and experienced eye clearly would be able to distinguish the difference between the characteristic of this nonlinear oscillations vs. linear classic simple harmonic oscillations. From this plot alone one may deduce useful information such as period, which for the chosen utilized parameters is 32.0 s. The initial distance of the particle from the center of the ring is 8 R =0.8 m. It takes 8.0 s for the particle to make it to the center. At that

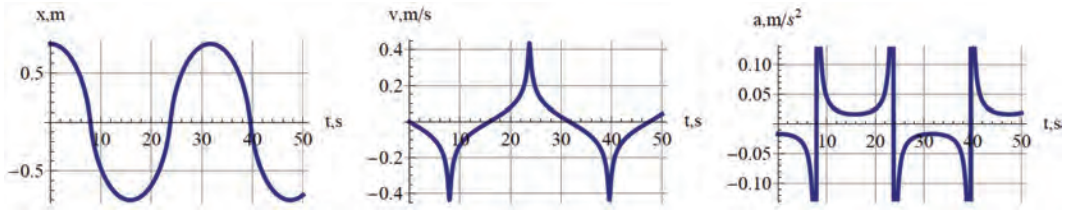

Figure 2. Display of the position x, velocity v and acceleration a of the charged particle vs. t, respectively from left to right

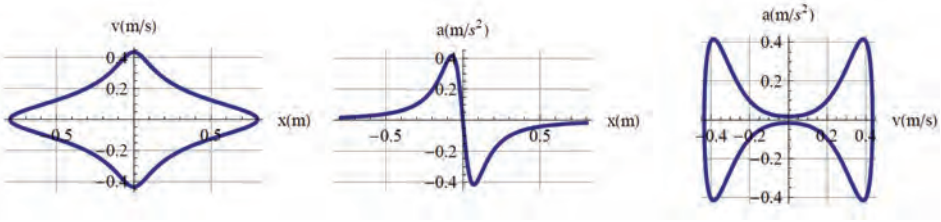

Figure 3. Plots of {x(t),v(t)}, {x(t),a(t)} and {v(t),a(t)} from left to right, respectively

instance, according to the center graph of Figure 2, the velocity of the particle is at maximum; its acceleration according to the far right graph of Figure 2 is at maximum. From this instant moving forward, the particle continues sliding to the left, while continually loosing speed. When the clock ticks 16.0 s its instantaneous speed plunges to zero; at that moment it reverses its motion speeds up, and accelerates toward the center of the ring.

To display the differences between the characteristics of the classic simple harmonic motion vs. our designed nonlinear oscillations, we display three phase diagrams. Utilizing Mathematica ParametricPlot we fold the time parameter and plot a set of three kinematic pairs: $\{x(t),v(t)\}$, $\{x(t),a(t)\}$ and $\{v(t),a(t)\}$.

```
plotxv=ParametricPlot[Flatten[{positionx,velocityx}],{t,
0,50},AxesLabel→{"x(m)","v(m/s)"},PlotStyle→Thick,
GridLines→Automatic,PlotRange→All];
plotxa=ParametricPlot[Flatten[{positionx,accx}],{t,0,50}
,AxesLabel→{"x(m)","a(m/s^2)"},PlotStyle→Thick,Grid
Lines→Automatic,PlotRange→All];
plotva=ParametricPlot[Flatten[{velocityx,accx}],{t,0,50}
,AxesLabel→{"v(m/s)","a(m/s^2)"},PlotStyle→Thick,Gri
dLines→Automatic,PlotRange→All];
Show[GraphicsArray[{plotxv,plotxa,plotva}],ImageSize
→500]
```

As one may speculate, the shapes displayed in Figure 3 are sensitive to the chosen parameters $\{R,Q\}$ and $\{m,q\}$. The interested reader may run the code for various parameters.

4. Energy of the Nonlinear Oscillator

In the analysis of the classic linear harmonic oscillations one displays the interplay of the kinetic and potential energies of the oscillator vs. time, *t*. For a conservative setting *i.e*. when the friction forces are ignored, the sum of these two energies over the span of the oscillations remains constant. Utilizing the same assumption, a nonlinear oscillator preserves its energy as well; however, the time dependent variation of its kinetic and the potential energies are quite different from the linear counter case. We utilize the solution of Equation (2). The potential and kinetic energies of the oscillators are: $PE=\frac{kQq}{\sqrt{R^2+x(t)^2}}$ and $KE=1/2\ mv(t)^2$, respectively.

$$\{PE,KE,totalEnergy\}=\{\ -kQq\frac{1}{\sqrt{R^2+positionx^2}}\ ,1/2\quad m\ velocityx^2,(1/2\quad m\quad velocityx^2\ -kQq\frac{1}{\sqrt{R^2+positionx^2}}\ )\}$$

```
//.values;
Plot[{10^7 PE,10^7 KE,10^7 totalEnergy},{t,0,20},PlotStyle
→{{Thick,GrayLevel[0.5]},{Thick,Black},{Thick,Dashi
ng[{0.02}],GrayLevel[0.2]}},PlotRange→All,AxesLabel
→{"t,s", "Energy,J"},GridLines Automatic]
```

For the sake of displaying the energies with a meaningful scale the energies are magnified by a factor of 10^7. According to Figure 4 and as we discussed in the previous section, the oscillator with an initial zero speed begins sliding toward the center of the ring. Since it is farthest from the ring, its potential and kinetic energies are at minimum and zero values, respectively. These are shown by the far left tails of the curves in Figure 4. While the oscillator accelerates toward the ring, its potential energy decreases and the speeding particle gains kinetic energy. When the oscillator is at the center of the ring, its potential energy is at minimum; conversely its kinetic energy is at maximum. At any given instance the sum of the values of the potential and the kinetic energies stays constant; the dashed horizontal line confirms the fact.

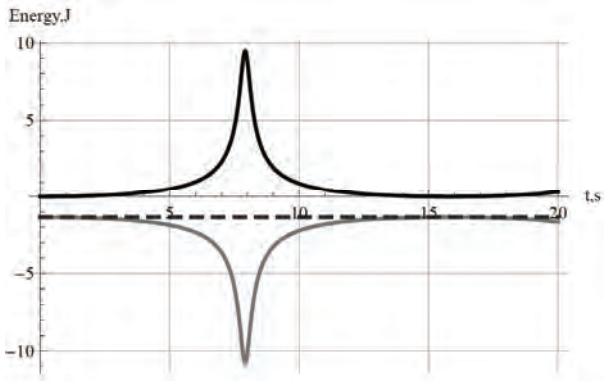

Figure 4. Display of the potential energy (the light gray curve), kinetic energy (the black curve) and the total energy (the dashed line) vs. time

5. 3D Real-Life Animation and the Art Work

A sinusoidal time dependent function describes the oscillations of a classic linear oscillator. As an example we may envision the swinging movement of a simple pendulum under gravity's pulls. How does a nonlinear oscillator swing? Applying the solution of Equation (2) and utilizing Mathematica's animation feature we compose a code to bring the nonlinear oscillations to life. The animation depicts a positively charged ring in red, a negatively charged particle in blue, and the electric field/force in green. The released particle from its initial positive position on the x-axis moves toward the ring. For the chosen ring size, the maximum value of the field/force occurs in the vicinity of its center; at $x = \frac{R}{\sqrt{2}}$. The animation clearly shows the impact of the nonlinear field. i.e., when the particle makes it to the maximum field, the field jerks the particle and radically changes its movement.

```
plot3d1=ParametricPlot3D[{0,x, √(1-x^2) },{x,-1,1},Plot-
Style→{Red,Thick},PlotRange→{-1,1},AxesLabel→
{"x","y","z"}];
plot3d2=ParametricPlot3D[{0,x,- √(1-x^2) },{x,-1,1},Plot-
Style→{Red,Thick},PlotRange→{{-1,1},{-1,1},{-1,1}},
AxesLabel→{"x","y","z"}];
Show[{plot3d1,plot3d2}];
plotlinex=ParametricPlot3D[{t,0,0},{t,-1,1},PlotRange
→{{-1,1},{-1,1},{-1,1}},PlotStyle→Thick];
plotliney=ParametricPlot3D[{0,t,0},{t,-1,1},PlotRange
→{{-1,1},{-1,1},{-1,1}},PlotStyle→{Dashing[0.02],Thi
ck}];
plotlinez=ParametricPlot3D[{0,0,t},{t,-1,1},PlotRange
→{{-1,1},{-1,1},{-1,1}},PlotStyle→{Dashing[0.02],Thi
ck}];
Show[{plot3d1,plot3d2,plotlinex,plotliney,plotlinez}];
EfieldRing3D=ParametricPlot3D[{x,0,1/40Evaluate[Ef-
ieldRing[x]/.values]},{x,-1,1},PlotStyle→{Green(*Gra-
yLevel[0.5]*),Thick}];
Manipulate[Show[{plot3d1,plot3d2,plotlinex,plotliney,
plotlinez,Graphics3D[{Blue,Sphere[{positionx[[1]]/.t→
τ ,0,0},0.05]}],EfieldRing3D},FaceGrids→{{0,0,1},{0,0,
-1}},FaceGridsStyle→Directive[Black,Dashed,Thickn-
ess[0.003]]],{τ,0,50,0.1}]
DynamicModule[{τ=0},Show[{plot3d1,plot3d2,plotlin-
ex,plotliney,plotlinez,Graphics3D[{Blue,Sphere[{positio-
nx[[1]]/.t→τ,0,0},0.05`]}],EfieldRing3D},FaceGrids→{
{0,0,1},{0,0,-1}},FaceGridsStyle→Directive[Black,Das-
hed,Thickness[0.003`]]]]
```

6. Extended Design Possibilities

Utilizing the concepts described in the previous section, one may readily fabricate limitless electric-springs. Without deviating too far from what we have already described, we introduce a charged double-ring electric-spring. For instance, by adjusting the values of the charge densi-

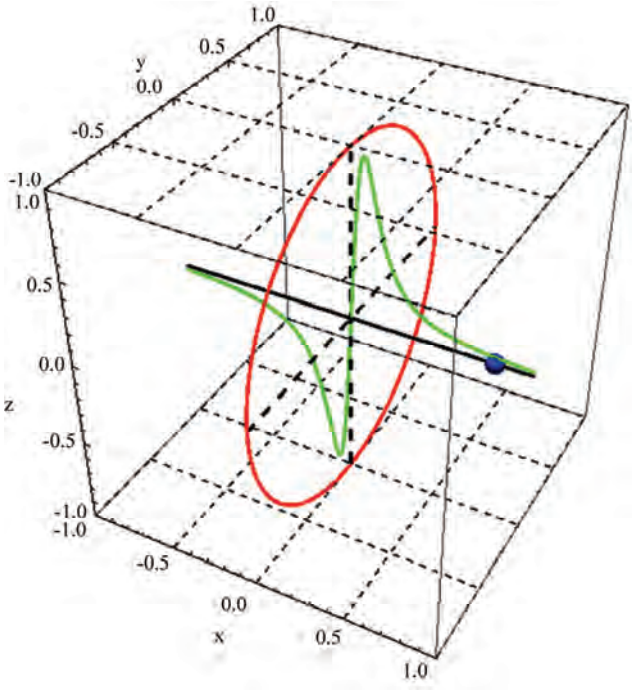

Figure 5. A snapshot of animated movement of a negatively charged particle (the black dot), within the electric field (the light grey signal) of a positively charged ring (the black circle)

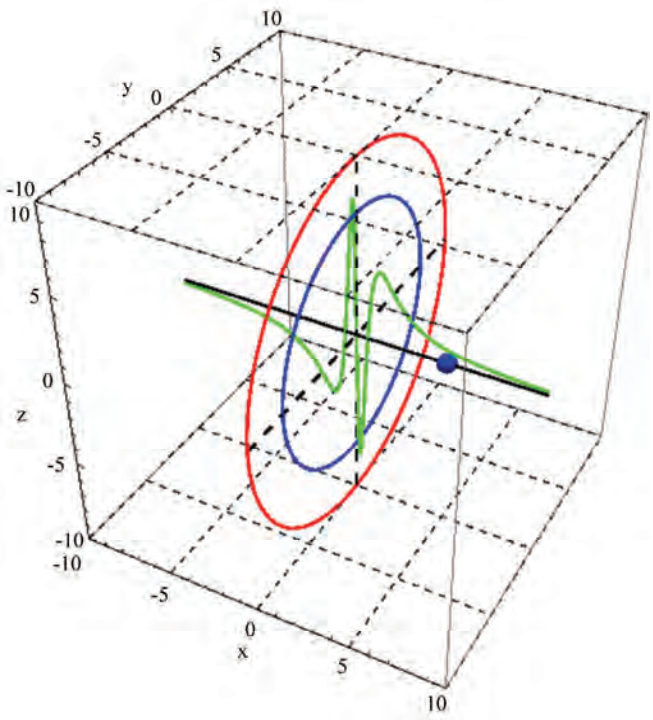

Figure 6. A snapshot of the motion of the negatively charged particle (the black ball), and the double-ring. The outer ring is positively charged, the inner ring is negatively charged, and each ring has its own linear charge densities. The electric field along the common ring axis is in light grey

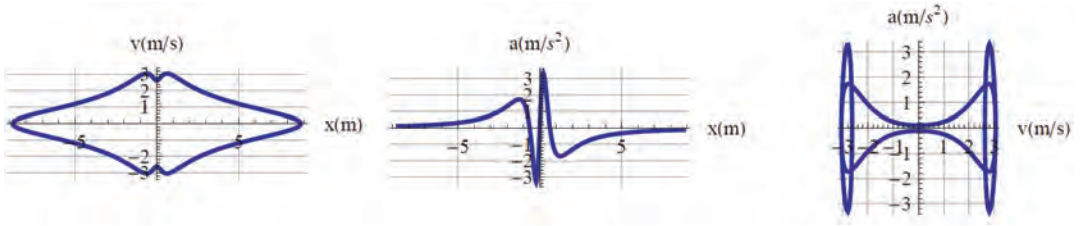

Figure 7. Plots of {x(t),v(t)}, {x(t),a(t)} and {v(t),a(t)} are displayed in left, center and right diagrams, for the charged double-ring, respectively

ties of the rings, e.g. a positive density for the outer ring and a negative density for the inner ring, we were able to produce a double hump electric field. In Figure 6, the field is depicted in green. The positions of the humps are a function of the rings' radii. By choosing a set of appropriate radii one may set the abscissa of the humps at desired positions. The field of the double-ring electric- spring shown in Figure 6 is distinctly different from the one shown in Figure 1. Utilizing the former we form the equation describing the movement of a negatively charged particle. The equation of motion is similar to Equation (2). However, because of the shape of the electric field the solution of the equation and therefore the description of the motion is distinctly different from what we have shown in the previous section. We compose a Mathematica code and animate the motion. This is shown in Figure 6.

Applying the solution of the equation of motion we plot three phase diagrams similar to the ones displayed in Figure 3. These are shown in Figure 7.

Comparing Figure 7 with Figure 3, one clearly sees the drastic differences. The impact of the double-ring on the oscillations of the oscillator is significant. The most notable impacts are displayed in the far left and the far right plots of Figure 7.

7. Conclusions and Remarks

In this article the author introduces a perfect mass-less static electric-spring design resulting nonlinear mechanical oscillations. The core idea of the design is based on the configuration of the electric field of a suitable static charge distribution. Utilizing the symmetry of a circular ring, it is shown that the field along the axis of the ring

has the desired characteristic. The magnitude of the field along the axis varies non-linearly with distance making the force that acts on the particle nonlinear as well. It is also shown how the design is modified. For instance the details of a coplanar charged double-ring is discussed and exhibits an interesting non-linearity behavior. A thorough literature search reveals no such practical designs have been proposed earlier. Furthermore, based on the aforementioned detailed discussions one realizes that the number of blue print electric-spring designs are limitless. Therefore, one may design springs to meet any practical needs. The available literature on the mechanical nonlinear physics phenomenon mostly is discussed from a purely theoretical view. In this article we have shown practical and applicable applications. We also would like to point out that in our study because of the slowness of the motion of the charged particle justifiably we ignored the effects of electromagnetic radiation of the oscillator.

REFERENCES

[1] S. Wolfram, "The Mathematica book," 5th Ed., Cambridge University Publications, 2003.

[2] E.g. J. Marion, "Classical dynamics of particles and systems," 4th Ed., Harcourt College Publishers, 1995.

[3] G. Duffing, "Erzwungene schwingungen bei veranderlicher eigen-frequenz," F. Vieweg und Sohn, Braunschweig, 1918.

[4] S. Strogatz, "Nonlinear dynamics and chaos," Perseus Publishing, 1994.

[5] http://wow.scalped.orgy/article/Duffing_oscillator.

[6] R. H. Ennis and G. C. McGuire, "Nonlinear physics with Mathematica for scientists and engineers," Published by Birdhouse, Hard Spring, Peg 605, 2001.

[7] E.g. J. D. Jackson, "Classical electrodynamics," 3rd Ed., Wiley, 2005.

J. Electromagnetic Analysis & Applications, 2010, 2: 82-90
doi:10.4236/jemaa.2010.22012 Published Online February 2010 (www.SciRP.org/journal/jemaa)

Scientific Research

Implementation of a Higher Quality dc Power Converter

Nader N. Barsoum

Curtin University of Technology, Miri, Malaysia.
Email: nader.b@curtin.edu.my

Received September 3rd, 2009; revised October 8th, 2009; accepted October 15th, 2009.

ABSTRACT

*Many single and three-phase converters are well developed, and covered up in most of electric markets. It is used in many applications in power systems and machine drives. However, an exact definite output signal from the dc side still not recognized. The waveforms of output voltage and current demonstrate an imperfect dc signal and constitute losses, harmonic distortion, low power factor, and observed some ripples. An approximately perfect rectifier bridge is the aim of this research. Perhaps it gives the ability to identify the parameters of the converter to obtain, as much as possible, a perfect dc signal with less ripple, high power factor and high efficiency. Design is implemented by simulation on Power Simulator PSIM, and practically, a series regulator LM*723 *is applied to provide regulating output voltage. Comparisons of both simulation and hardware results are made to observe differences and similarities.*

***Keywords*:** *Simulation, Microcontroller, Converter, Feedback, Power Factor, Design*

1. Introduction

In industrial application, Direct Current (dc) is used for controlling application such as Programmable Logic Controller (PLC), Microcontroller, dc motor and many commercial and domestic appliances [1–4]. Rectifier has become a popular power source [5–7] for these appliances because of its reduced cost and relatively low sensitivity to supply voltage variations under normal operating conditions. Stability is the key issue in these applications as it involves certain precision and decision making [8]. These systems are usually employed in automotive and aerospace applications [6,9] where tiny little error in the supply (unstable dc) might cause a large disaster.

The processed output voltage, current as well as frequency, will be as desired by the load. If the power processor's output can be regarded as a voltage source, the output current and the phase angle relationship between the output voltage and the current depend on the load characteristic. Also, normally, a feedback controller will be provided to perform comparison to the output of the power processor unit with a desired reference value, and the controller minimizes the error between the two.

Generally, design of converter that can be considered as a good design, should cover few essential aspects [10]. One of them will have to be efficient, which can be considered as the ultimate goal of design in power electronic. Besides that, a few current issues can be directly and indirectly affected the course of a design of a converter. One of these significant issue is the line quality, whereby is critical to ensure that the utility lines and transformer would supply undistorted wave voltage to customers. The source and line inductances play an important role in the line quality issue. With the presence of the reactive power to the line, it increases the volt-ampere rating. Thus, the input ac line voltage becomes distorted from the higher peak currents. As a result, high reactive components are being used. This is a drawback because a poor power factor causes heavy expenses to the user.

Besides that, the growing concern regarding harmonic pollution of the power distribution system creates awareness for clean ac line current and a power factor close to unity. The phase angle of the fundamental harmonic current [2,5] with respect to the line voltage is a very important parameter that determines the power factor. These issues are some of the critical aspects that should be taken into consideration when designing a good converter.

Power factor correction is achieved by the addition of capacitor in parallel with the connected motor circuits and can be applied at the starter, or applied at the switchboard or distribution panel. The resulting capacitive (leading) current is used to cancel the inductive (lagging) current flowing from the supply.

The microcontroller program performs this. The microcontroller is programmed in such a way that it will perform the checking the phase difference every 1/2MHz

second (microcontroller running on 2MHz crystal) and calculate out the phase different between the current and voltage waves. The calculated value will be converted into signal to activate appropriate capacitor to correct the power factor [2,11,12].

Capacitors are installed parallel to the source, waiting for the signal from the microcontroller. When microcontroller sends signal, the signal will be amplified via MOSFET and activate a relay. The relay hence will turn on the capacitor. The feedback circuit is designed in such a way that the system is allowed to be a capacitive system but not an inductive system.

2. Implementation of Single Phase Converter

2.1 Step-Up Converter with Feedback Control

To further improve the output signal generated, by means of current shaping, it can be archived through step-up converter with feedback control applied at dc side of the rectifier to replace the LC filtering component. With this arrangement, it is possible to shape the input current drawn by the rectifier bridge to be sinusoidal and in phase with the input voltage. For the purpose of better illustration, Figure 1 shows the circuit configuration. At the input side, the input current i_s is desired to be sinusoidal and in phase with input voltage V_s, also, at the full bridge rectifier output, i_L and absolute value of V_s will have the same waveform as well. For the theoretical analysis below, the power loss of the rectifier bridge and the step-up converter will be neglected due to the fact that the losses are somewhat small.

Thus, we have, for $\hat{V}_S = \sqrt{2}V_S$ and $\hat{I}_S = \sqrt{2}I_S$, the input power can be expressed as:

$$P_{in}(t) = \hat{V}_S \left|\sin \omega t\right| \hat{I}_S \left|\sin \omega t\right| = V_S I_S - V_S I_S \cos 2\omega t \quad (1)$$

The average value of current I_d can be expressed as:

$$I_d = I_{load} = \frac{V_S I_S}{V_d} \quad (2)$$

Also, the current through the capacitor is:

$$i_C(t) = -\frac{V_S I_S}{V_d} \cos 2\omega t = -I_d \cos 2\omega t \quad (3)$$

From these expressions, the ripple in V_d can be determined by means of estimation, as shown in Equation (4):

$$V_{d,ripple}(t) \approx \frac{1}{C_d} \int i_C \, dt = \frac{I_d}{2\omega C_d} \sin 2\omega t \quad (4)$$

The step-up converter shown in Figure 1 is operating in current-regulated mode, as our main purpose is to shape the input current of the step-up converter. The feedback control, represented in block diagram, is shown in Figure 2. This feedback control serves as the purpose of comparing the output generated with a reference value, in order to minimize the error between these two.

i_L* shown in Figure 2 is the reference value of the current i_L in the step-up converter. The amplitude of i_L* should be such that as to maintain the output voltage at a reference level of V_d*, in spite of the variation of load and the fluctuation of the line voltage from its nominal value. The waveform of i_L* is obtained by means of measuring absolute value of V_s by a resistive potential divider and multiplying it with the amplified error between the reference value V_d* and the actual measured value of V_d. On the other hand, the actual current i_L is sensed, usually by measuring the voltage across a small resistor inserted in the return path pf i_L. The status of the switch in the step-up converter is controlled by comparing the actual current i_L and i_L*.

If constant frequency is applied for this feedback control, the ripple current can thus be expressed as:

$$I_{rip} = -\frac{(V_d - |V_S|)|V_S|}{f_S L_d V_d} \quad (5)$$

In terms of maximum ripple current, it can be expressed as:

$$I_{rip,\max} = \frac{V_d}{4 f_S L_d} \quad (6)$$

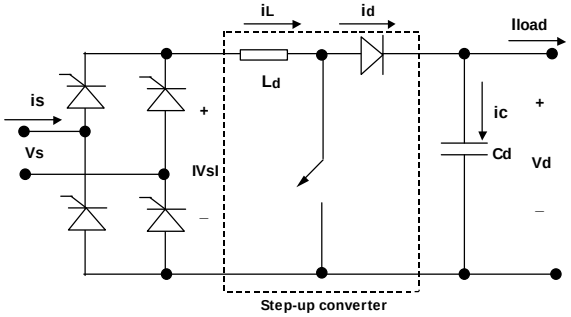

Figure 1. Step-up converter for current shaping

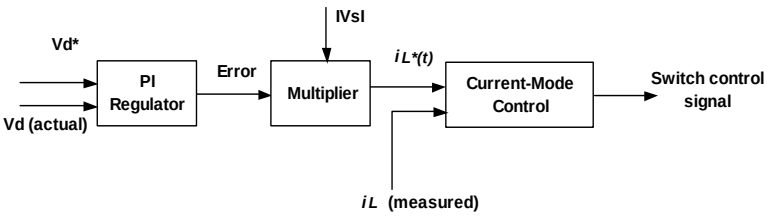

Figure 2. Feedback control block diagram

The step-up converter topology is well suited for the input current shaping method because when the switch is off, the input current directly feeds the output stage.

2.2 Complete Design with Step-Up Converter at dc Side

The feedback controller shown above operates by comparing the output generated with a reference value set. In simulation, the actual output current is sensed by a current sensor connected at dc side of the rectifier, and this actual value of I_d is sent to negative probe of the summer. The reference value of I_d is transmitted through positive probe of summer. The comparison of signal will take place at the comparator, with signal generated from PI controller and triangular wave.

For better reference, Figure 3 shows the complete design of single-phase controlled rectifier with step-up converter and feedback control implemented in PSIM.

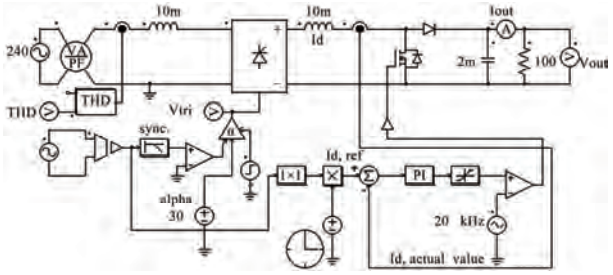

Figure 3. Thyristor converter with step-up converter

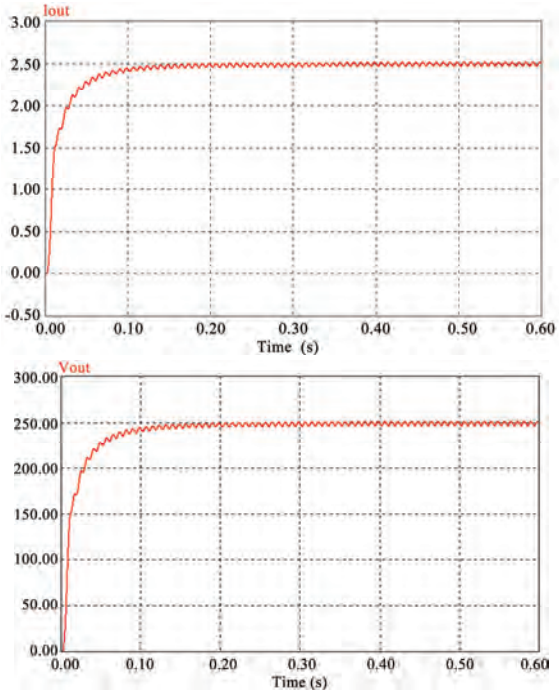

Figure 4. Waveforms for output voltage and output current

2.3 Simulation Results

Simulation is carried out based on similar parameters applied on rectifier design without step-up converter in order to observe the difference between these two designs. Similarly, for better illustration, simulation results corresponding to firing angle of 30º are shown in Figure 4.

2.4 Comparison of Results

Comparison between the two types of rectifier design configuration is given in Table 1. It shows some of the essential parameters corresponding to firing angle of 0˚.

The table indicates that thyristor converter with step-up converter and feedback control shows an improvement in overall aspects. In terms of THD, it improved from 49% to 21%. While as for power factor produced, it increased from 0.81 to 0.98.

2.5 Design of Hardware

In hardware manner, the variable dc output will be controlled by means of applying a regulator chip LM723 to control the output voltage generated. This design method is rather different than the design approach implement in simulation. One of the reasons for this is that an exact solution for hardware implementation based on design in simulation has not yet been found; these reasons will be outlined in more details in problems encountered and suggestions for further development. For this practical design, in terms of rectifying component, Diode Bridge will be applied for this hardware implementation. For better illustration, the circuit diagram for the practical design is shown in Figure 5.

For this particular design, the input voltage V_s is equal to 18V, which is stepped down by a transformer, not shown in the figure. Diode D1, D2, D3 and D4 forms the diode bridge, KP206G. Also, another diode, IN539 is applied at dc side. One of the functions for this diode is to act as a feedback blocker, whereby it steers any current that might be coming from the device under power around the regulator to prevent the regulator from damages. These sorts of reverse current usually occur when the rectifier is been powered down.

2.6 Operation Analysis

Basically, this practical rectifier design applies a different

Table 1. Comparison of results

Parameters	Types of rectifier configuration	
	Without Step-up Converter	With Step-up converter and feedback control
Output voltage	200V	246.5V
Ripple voltage	4.3V (2.15%)	3V (1.21%)
THD	49%	21%
Power Factor	0.81	0.98

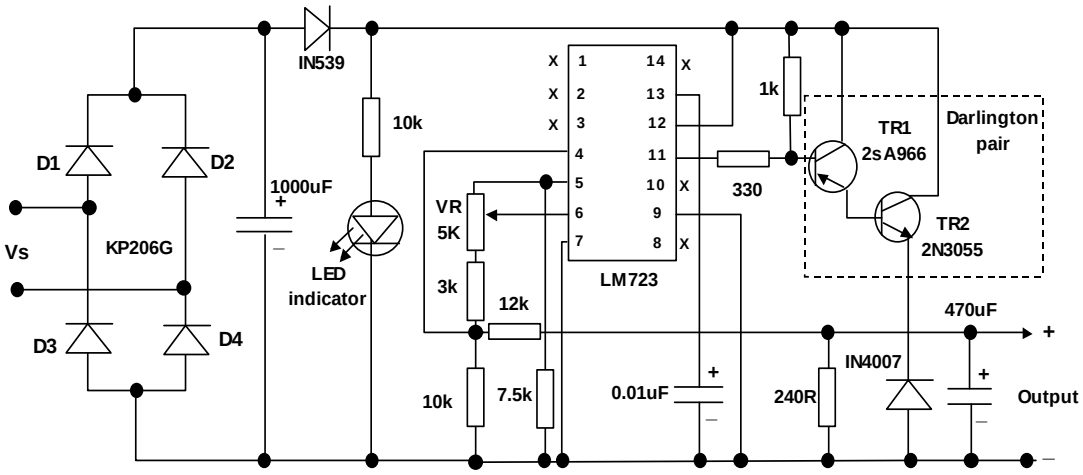

Figure 5. Circuit diagram of practical converter design

comparable approach to implement in simulation. Referring to Figure 5, with the use of the transformer, to steps down the input voltage to 18V. The voltage rectified by the diode bridge to produce unfiltered dc output voltage. This unfiltered dc output voltage will contain big ripple and is pulsating. This pulsating output voltage will then been filtered by the capacitive filter of 1100 μF capacitor in order to manageable for the regulator.

As noticed in Figure 5, there's only capacitive filtering applied to the design, this is due to the fact that in low-power applications, the inductor required for rectification design could be a costly item, that's the main reason most low-power converters dispense with the inductor and apply a direct capacitive filtering method. With no load, the dc voltage across the terminals of the filter is going to be 18 to 30 volts.

The regulation is obtained using the Darlington pair (TR1 and TR2). They in turn are controlled by the 723 regulator. 723 has its own internal highly regulated voltage reference supply (pin 6). Internally the 723 compare this reference voltage to the output of the power supply and it is varied by means of variable resistor VR, shown in Figure 5. This sets the output voltage. The regulation process evolves around pin 11 and pin 6 of LM723 regulator. Pin 11 of 723-regulator control voltage supply, and this V_C will trigger the base of TR1, which is 2SA966, PNP transistor, which will act as a simple amplifier to increase the current available to drive the base of the pass transistor, i.e. TR2 2N3055. This explains the function of Darlington transistor pair applied.

Capacitance of 0.01μF connected to frequency component (pin 13) of 723-regulator function as a transient response improver, which improves the response of the regulator when it is operating during high frequencies. Regulated dc output, will be filtered again by capacitance of 470μF to produce an output voltage that contains a minimum ripple and close to pure dc voltage. Necessary protective device have all been installed in this practical design such as fuses, metering component for voltage and current, not shown in the figure. Note here, these metering component are meant for as a guideline as the accuracy of these meters might be a ±1V difference for the case of voltmeter. Therefore, for better accuracy, a multimeter should be used.

Figure 6 shows an overall view of practical design. Note, TR2 and 2N3055 are mounted on a huge heat sink. This step is necessary, as the heat sink installed will helps to dissipate the massive flow of heat generated to the pass transistor.

2.7 Comparison of Results

As design implemented from hardware manner, which applied the diode bridge as main conversion component, for comparison purpose, we compare the results from design in the simulation corresponding to firing angle of 0°. Table 2 shows results from both of the design. It shows that the design implemented in simulation use 20V as

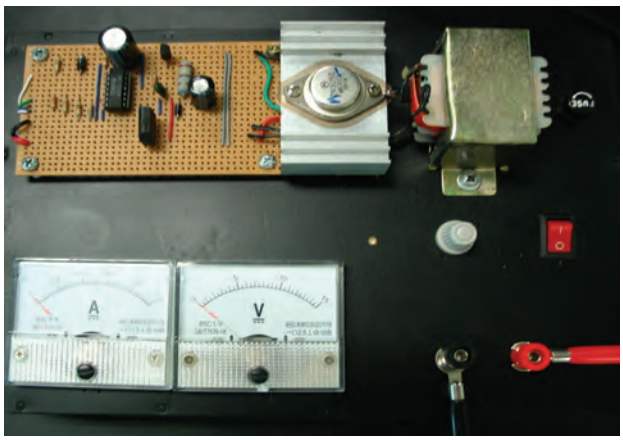

Figure 6. Overall view of practical design implemented

Table 2. Comparison of results

Parameters	Design method	
	Design from simulation (firing angle = 0°)	Practical Design
Input Voltage	20V	18V
Output Voltage	37.7V	15.8V
Ripple voltage	1.24V (3.3%)	800mV (5.06%)
Output Current	0.37A	0.18A
Output power	13.9W	2.84W
THD	30.2%	47.7%
Power Factor	0.96	0.90

input voltage, as main concern is on low power application. While in hardware design, the input voltage is in 18V, which is stepped down by a step down transformer. 18V secondary side voltage is one of the common rates of voltage used in terms of low voltage application.

Results shown clearly indicate that the simulation have gain advantages over the practical design. These are shown through power factor produced and total harmonic distortion created. However, the difference in terms of power factor and ripple voltage didn't show a big difference. The only major difference comes from the total harmonic distortion.

Note that when comes to comparison of results from simulation and practical manner, some slight discrepancies should be taken into account. This is due to the fact that from simulation point of view, generally ideal components are used and so they have theoretical constraints associated with them, which is possible to differ slightly from the actual physical component. As for practical converter, there might be losses in the process of stepping down voltage as well as where conversion from ac to dc takes place. Besides that, each of the components, particularly resistors and diode used, all contribute to losses generated.

3. Implementation of Three Phase Converter

3.1 Feedback Control Loop

As far as power factor and total harmonic distortion is concern, inductors are added at the source to compensate the capacitive value produced by the capacitor at the filtering device. This solution is being taken one step further to install a feedback control device to compensate the inductive value produced by the load in case the converter is used for a dc motor. Thus, a feedback control loop is proposed to improve the power factor of the system. This is shown in Figure 7.

Power factor correction is achieved by adding capacitors in parallel with the connected motor circuit and can be applied at the starter or the switchboard or distribution panel. The resulting capacitive current is leading current and it is used to compensate the lagging inductive current flowing from the supply.

This correction task is carried out by micro-controller, which is specially designed to perform the checking and correcting the incoming voltage and current. External comparator MCP6024 is used to convert the analogue signal to 2-bit digital signal. The converted signal is then input into the microcontroller to perform phase difference analysis.

Signals that are about to be input into the microcontroller are phase-shifted voltage and the voltage that represents the current. Phase-shifted voltage is obtained near the load for the voltage at the load will represent the voltage's phase shift. Voltage's phase is taken as variable while the current's phase is taken as constant. If the load is capacitive, the voltage's phase is lagging the current's phase. If the load is inductive, the voltage phase is leading the current phase.

The microcontroller will observe the voltage phase. When the microcontroller detected a '1' for voltage, it will then observe the current phase (represented by voltage across the load). If the current is not detected, it will return a '1' and activate capacitor A from the capacitor bank. After that, it will check both the voltage and current phases again. If the current phase is again not detected when the voltage phase is detected, it will return another '1' and now, activate capacitor B. The whole process will repeat until the capacit or E in the capacitor bank is activated, or, the current is detected when the voltage phase is detected. The process algorithm is shown

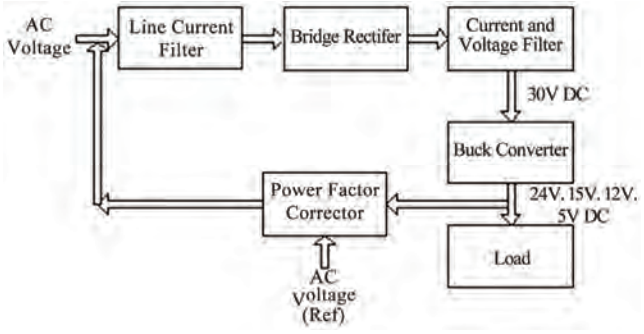

Figure 7. Feedback controlled three phase converter

in Figure 8. Every time when there is a change in the load (manually), then the power factor corrector has to be reset in order to function properly. The power factor correction algorithm is being implemented in MATLAB simulation. The program enables the user to input the load inductance and the program will return the number of capacitor of the dedicated value needed. It can also display the uncompensated and the compensated waveforms. The output is shown in Figure 9.

In Figure 9, the load used is 10 kΩ and the load inductor is 1 mH. There are 99 capacitors rated 100 pF needed to compensate the inductance. It is understood that the compensation could not be 100% because the signal is being sampled with Nyquist sampling rate. The program is written in such a way that the microcontroller will ensure that the system is capacitive rather then inductive.

3.2 Integration of Designs

The designs are being integrated together to form a complete ac-dc converter with high power factor, low harmonic distortion and low voltage ripple. This is shown in Figure 10 following Figure 7.

It is noticed that the 1M Ω resistor at the output of the rectifier circuit is being removed. This is to allow the current to flow completely into the load circuit without any additional current drawn over unnecessary load.

The duty cycle D of the Buck converter is set to four mode of operation, namely, 0.167, 0.4, 0.5 and 0.8. These duty cycles will give 5V, 12V, 15V and 24V respectively.

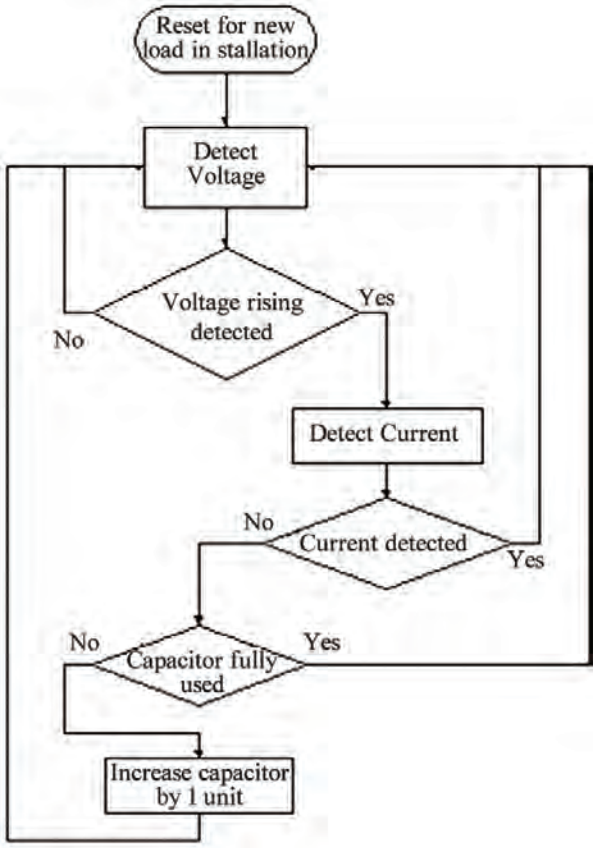

Figure 8. Power factor corrector flowchart

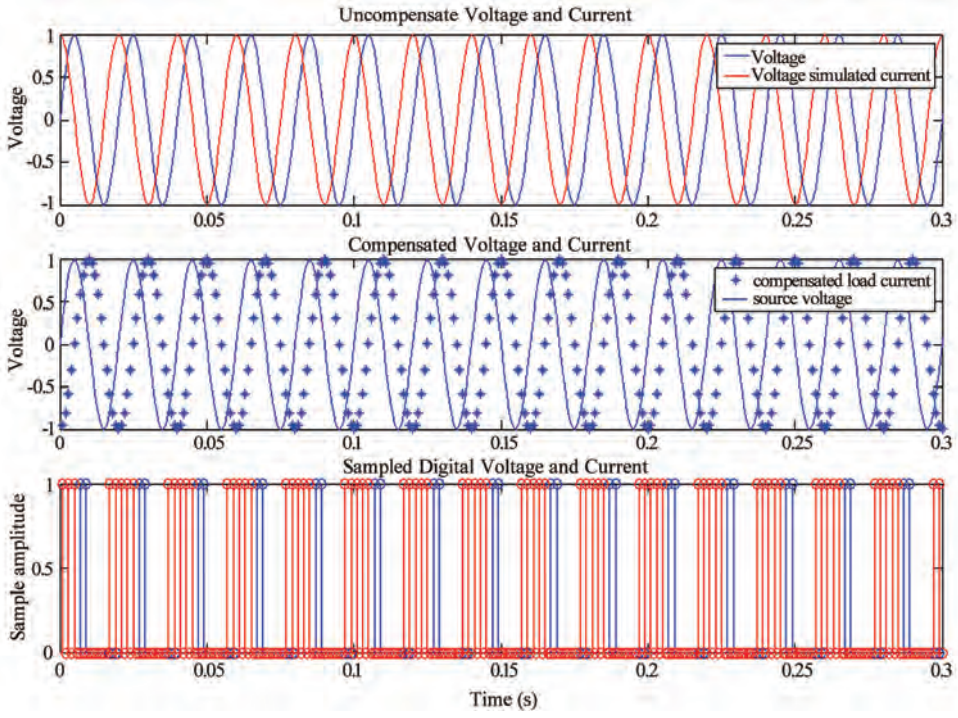

Figure 9. Power factor correction made onto the inductive system

It is also noticed that the source rms line voltage is being step up to 23V. This is because, the diodes used are no longer ideal diode, and a 0.7V voltage drop is introduced across the diode. Increasing the source voltage to 23V rms will ensure that the four duty cycle operation modes will achieve the desired output.

3.3 Simulation

At D=0.8, the desired output is 24V and 10kΩ sample load is placed at the output of the ac-dc converter. The output current and voltage is shown in Figure 11:

The output is being evaluated in frequency domain as is shown in Figure 12.

It is noticed that the output current and voltage shows an extremely low ripple and the rise time is less than 0.4 seconds. In frequency domain, the frequency component is less than 200Hz, which means, the harmonic of the output is extremely low, even the fundamental frequency (300Hz) is almost completely reduced.

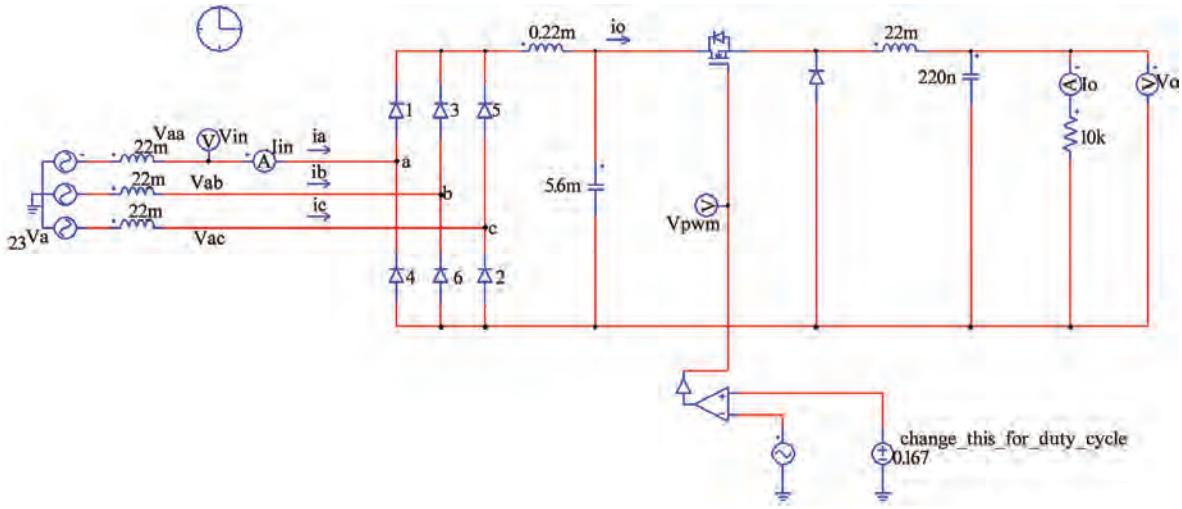

Figure 10. Integration of the rectifier and Buck converter

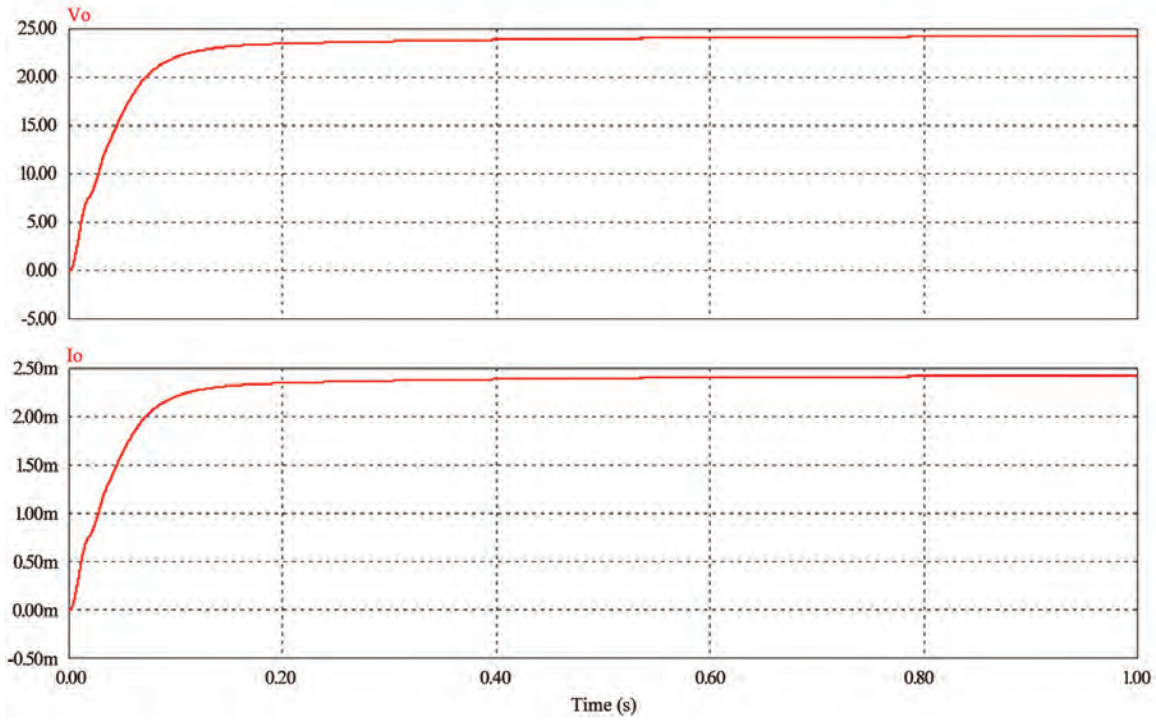

Figure 11. Output current and voltage waveform with D=0.8

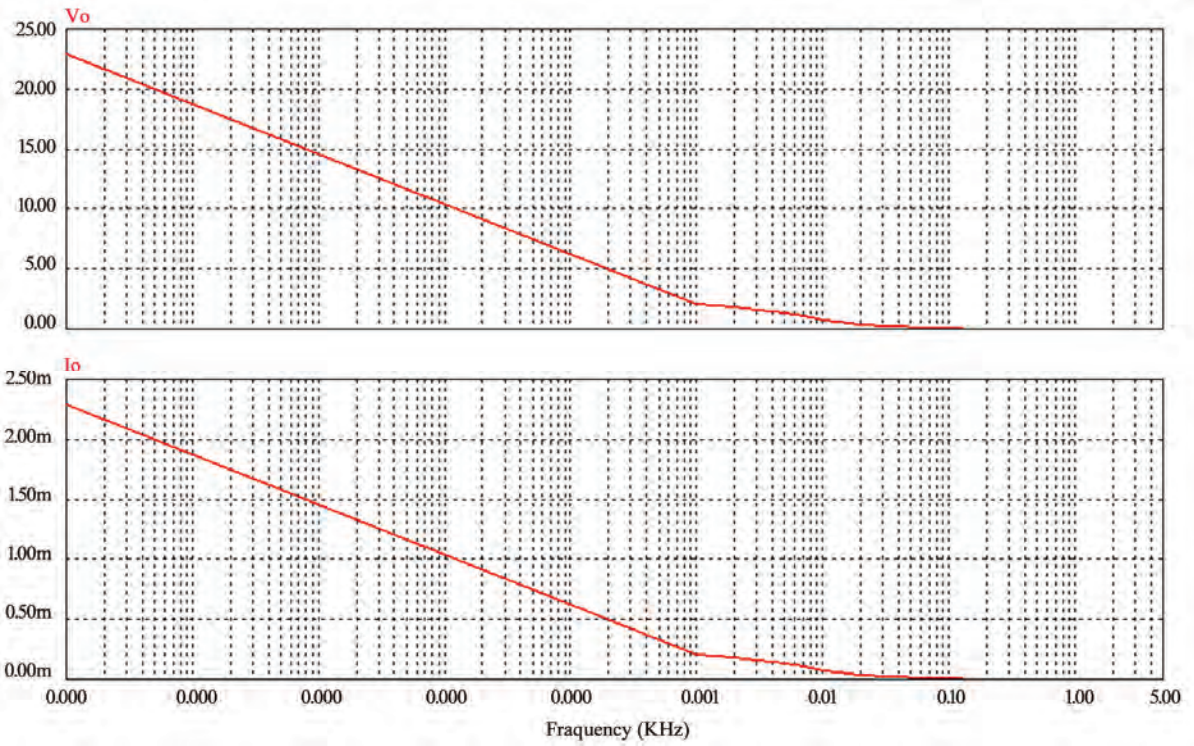

Figure 12. Output current and voltage in frequency domain with D=0.8

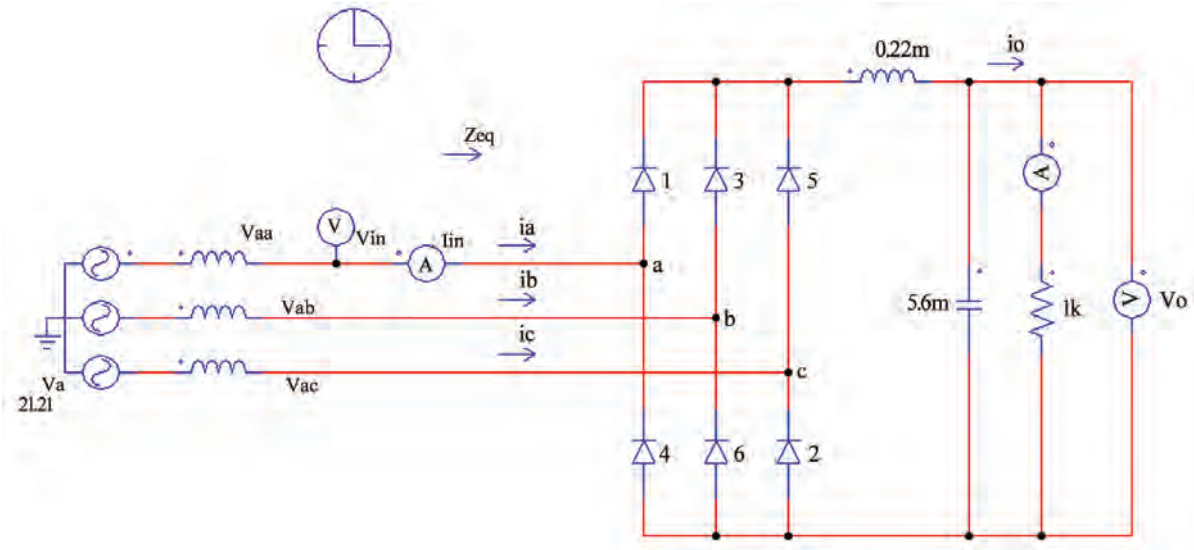

Figure 13. Three-phase rectifier with THD reduction

3.4 Implementation

Implementation is done up to the LC filter stage. The schematic that is being implemented is shown in Figure 13 with resistance value of 1.2M Ω. The constructed hardware is given in Figure 14

Table 3 shows the input voltage, output voltage, ripple voltage, and the efficiency.

It is noticed that the efficiency is increasing while the input rms voltage increase. The voltage drop is to overcome the cut-in voltage across the diode. There is some voltage drop observed across the filter inductor due to the change of the current. The voltage drop across the inductor is very small as the current stabilized over a short period of time.

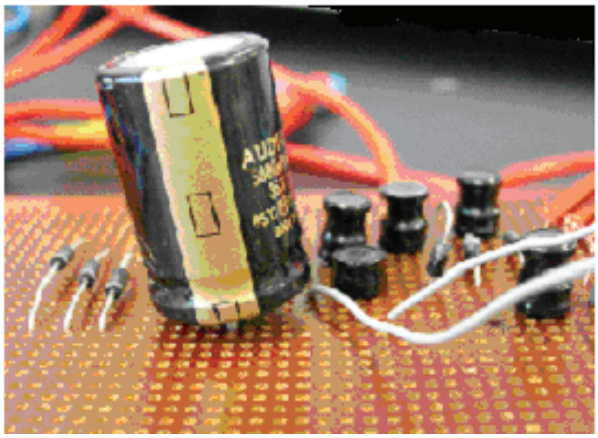

Figurer 14. Hardware implementation of the rectifier

Table 3. Tabulated simulation output

Vin (rms)	V_{out} (V)	V_r(mV)	V_r	Efficiency
2	1.3	12.96	0.978%	46.87%
4	4.2	41.18	0.992%	73.38%
6	7.0	67.81	0.972%	82.22%
8	9.8	93.61	0.955%	86.64%
10	12.6	123.88	0.981%	89.29%
12	15.5	152.06	0.984%	91.06%
15	19.7	197.31	1.002%	92.83%

As the input voltage increases, the efficiency increases because the voltage drop across the diode is a fix value.

The difficulty encountered during the simulation is that the inductor used could not sustain high power such that the inductor will blow off when the input rms voltages exceed 15V. This can be improved by using bigger inductor. The capacitor filter used could sustain 35V.

4. Conclusions

The design development stages in simulation from studies of fundamental circuits to the development of final design, which utilizes the feedback controller at dc side of the converter to further, improve the current waveform and thus producing an output signal with less distortion and better power factor. This design is then been use as a reference to implement a design in practical manner.

This proves that the feedback controller applied with the step-up converter can help in producing a better output signal.

The goal to achieve low harmonic distortion, high power factor and low ripple voltage can be achieved. The implementation is of low cost and the components used are easy to obtain.

The development of the power factor corrector could be used in some other aspect such as three-phase air-conditional circuit, or three-phase induction motor. In order to activate the power factor corrector on the ac-dc converter circuit, more research needed to be done.

The converter's components are designed in such a way that it can sustain the load resistance from 10Ω to 100kΩ. The rise time is maintained to be less than 0.5 seconds and the output voltage and current are critically damped. This is to ensure that transient output would not damage the equipment connected to it.

REFERENCES

[1] N. N. Barsoum and W. K. Janng, "Programming of PIC micro-controller for power factor correction," CD Proceeding of Asia Modeling symposium AMS, Phuket, Thailand, pp. 14–18, 27-30 March 2007.

[2] N. N. Barsoum and F. Png, "High quality ac power with TRIAC inverter," CD Proceeding of Australian Universities in Power and Energy Conference AUPEC, Melbourne, Australia, 10-13 December 2006.

[3] P. Spasov, "Microcontroller technology: The 68HC11," 3rd Ed., Prentice Hall International, 1999.

[4] K. Ogata, "Modern control engineering," 4th Ed., Prentice Hall International, 2002.

[5] N. Mohan, T. M. Undeland, and W. P. Robbins, "Power electronics, converters, applications and design," John Wiley & Sons, Inc, 2003.

[6] L. Van Der Sluis, "Transients in power systems," John Wiley & Sons, Ltd, 2002.

[7] J. M. Bourgeois, "Circuit for power factor correction with regards to mains filtering," STMicroelectronics, Italy. Retrieved August 23rd, 2006 from http://www.st.com/stonline/proucts/literature/an/3727.htm.

[8] N. N. Barsoum and M. R. Harris, "Theorems of torque coefficients on stability for induction and reluctance machines," International Journal of Electrical Engineering Education IJEEE, Manchester Institute of Science and Technology UMIST, UK, Vol. 38, No. 3(7), pp. 260–275, 2001.

[9] N. N. Barsoum and S. K. Wong, "Implementation of an active converter for high quality dc power performance," Proceeding of International Conference on Electric Machines ICEM, in CD, Chania, Greece, 2-5 September 2006.

[10] D. A. Neamen, "Semiconductor physics and devices: Basic principles," 3rd Ed., McGraw-Hill International, 2003.

[11] Power Factor, LM Photonics Ltd. Retrieved September 8th, 2006 from http://www.lmphotonics.com/pwrfact.htm.

[12] http://www.uoguelph.ca/~antoon/circ/vps.htm.

J. Electromagnetic Analysis & Applications, 2010, 2: 91-97
doi:10.4236/jemaa.2010.22013 Published Online February 2010 (www.SciRP.org/journal/jemaa)

Effect of Temperature and Concentration of Ammonium Nitrate Solution on the Succeptibility of Mild Steel to Stress Corrosion Cracking

Fathia S. Mohammed[1], Salaheddin E. A. Abu Yahya[2], Alyaa G. Elramady[2]

[1]Department of Chemical Engineering, American University of Sharjah, Sharjah, United Arab Emirates; [2]The Petroleum Institute, Abu Dhabi, United Arab Emirates.
Email: fmohammed@aus.edu

Received August 16th, 2009; revised September 28th, 2009; accepted October 4th, 2009.

ABSTRACT

The effect of varying the temperature and the concentration of ammonium nitrate solution on the stress corrosion cracking (SCC) susceptibility of mild steel is studied. An increase in the temperature causes a decrease in the stress corrosion life. It appears that the susceptibility in the range 368 *K to* 380 *K was greater than at other temperatures. Near the boiling point corrosion and stress corrosion occurs, at the boiling point, the cracking was associated with a high rate of general corrosion. Microscopic examination after stress corrosion testing in* 10*Wt%,* 20*Wt%, and* 52*Wt% NH_4NO_3 solution revealed that in all cases there was severe intergranular attack, especially at the high concentration.*

***Keywords*:** *Stress Corrosion Cracking, Ammonium Nitrate Solution, Mild Steel, Constant Load Test, Temperature Effect, Concentration Effect*

1. Introduction

In an attempt to determine what chemical and electrochemical properties of the corroding solution are required for stress corrosion cracking, previous researchers determined the potentiostatic polarization curves for single crystals in de-aerated boiling, 55% Ca $(NO_3)_2$, 30% NaOH, and other solutions [1]. The results revealed that iron exhibits passive behavior near the free corrosion potential in nitrate solution only. Although the surface film at the corrosion potential was stable, it required a long time to be restored if it was damaged.

Szklarska [2] stated that passivation phenomena were essential for the occurrence of the stress corrosion cracking of mild steel in nitrate solution. It was reported [3] that the sequence of the reaction of corroding iron in NH_4NO_3 solution was as follows:

1) Formation of a soluble complex salt of iron with ammonia, this salt being Fe $(NH)_6$ $(NO_3)_2$.

2) Production of nascent hydrogen which acts as a reducing agent.

3) Reduction of nitrate ions to NO_2^- as the main corrosion product.

4) Oxidation of ferrous ions to ferric ions.

The most probable cycle of reactions was considered to be:

Cathodic: $2H^+ + 2e \rightarrow 2H$

Anodic: $Fe \rightarrow Fe^{++} + 2e$

Secondary Cathodic: $2H + NO_3^- \rightarrow H_2O + NO_2^-$

Polarization studies on iron electrodes indicate that Fe_3C particles or carbon in interstitial solution may act as efficient sites for cathodic discharge during the corrosion reaction [4]. Intergranular penetration occurred in nitrates solution, but such penetration was limited to a depth of two grain diameters [5].

Most of the work regarding grain boundary attack of unstressed low carbon steel by nitrates has been carried out in NH_4NO_3 solution. Engell and Baumel [1] did produce this type of attack in boiling Ca $(NO_3)_2$ but only with the aid of anodic polarization. General overall attack in NH_4NO_3 is due to the high depolarizing power of the oxidizing NO_3^- ions on the cathodic local areas, coupled with the complexing action of the NH_4^+ which facilitates the anodic reaction, i.e. iron dissolution of Fe^{++} ions. Thus, the correlation of results from NH_4NO_3 solution with those from solutions of other cations (e.g. Ca^{++}, Na^+, K^+) probably has little significance.

Flis [6] proposed that after a small amount of grain boundary penetration, regions of stress concentration were produced. When the resulting strain in these regions was sufficiently large, the oxide film would be ruptured and the strain rate would be high enough to prevent the

reformation of the protective film. Thus, the crack propagation proceeded by an electrochemical process.

Whilst the various mechanisms of stress corrosion cracking were seldom proposed originally for the cracking of ferritic steels, they have all been suggested at different times as explaining the phenomenon of stress corrosion cracking in these materials. However, all the mechanisms are interpreted from data on the effects of various environmental and metallurgical parameters on stress corrosion. The susceptibility of the steel was remarkably affected by the concentration of the nitrate solution, this was noticed when cracking of mild steel in various nitrate solutions occurred. Baker and Singleterry [7] studied the stress corrosion cracking in u-bend specimens of A1S1 4340 steel. They reported that KNO_3 solutions show a systematic decease in the time to failure with increasing concentration.

One of the reasons for the lack of appreciation of the chemical factors that affect SCC is the lack of understanding of the large influences that are produced by small change in the environment. A change of one unit of the pH changes the solubility of oxide by three order of magnitude for three valence ion such as Fe^{+3} and by two order of magnitude for a two valence ion such as Fe^{+2} [8].

Leferink [9] reported that the steel samples were subjected to aerated ammonium nitrate solution at 368 K with concentration ranging between 2% and 35%, after an exposure for 65 hours; cross sections of the steel were studied. When intergranular corrosion attack (IGA) occurs the steel was considered sensitive to ammonium nitrate within these concentrations.

2. Experimental Work

2.1 Material

The work was carried out on mild steel of the following composition (Wt%):

C	0.070
Mn	0.300
Si	0.093
S	0.044
P	0.019

The Material was supplied in the form of 19 mm diameters rods. Corroding solution was prepared by using ammonium nitrate.

2.2 Specimen Preparation

2.2.1 For Electrochemical Measurement

The steel rods supplied were hot-rolled at 1200 K to strip –4mm thick. This was reheated to 1200 K in the furnace for 900 s, cooled slowly to 850 K, and then allowed to cool to room temperature. Most of the oxide film was removed by pickling in 30% Hcl solution, and the surface was finally cleaned for cold-rolling by mechanical abrasion. The strip was reduced to 0.5 mm thick by cold-rolling.

Samples 20 mm by 13 mm were prepared. A 3 mm holes was drilled at one end to suspend the samples, then the specimen were degreased with ether, annealed at 1200 k for 3.6 ks after wrapping in thin foil to prevent oxidation. The specimens were attached to the holder and the whole assembly coated apart from an area of 100 mm^2 on one face.

2.2.2 For Stress Corrosion Testing

The steel rod was hot-rolled at 1200 k and swaged cold to approximately 10 mm diameter. It was then annealed at 1200 k for 900 s, furnace-cooled to 850 k, followed by air-cooling to room temperature. The specimens were machined from the rod as shown in Figure 1. They have a gauge length of 15.8 mm and a gauge diameter of 3.2 mm.

2.3 Apparatus

2.3.1 Electrochemical Measurements

For electrochemical measurements on unstressed specimens, a glass cell comprising two compartments was designed. The main compartment contained the working electrode and the platinum counter electrode. The reference compartments contained a saturated calomel electrode. The complete cell is shown in Figure 2. The two compartments were connected by a salt bridge with a Luggin capillary. The glass joints that carried the working and the counter electrodes also had a screw cap joint for the thermometer. There was another two openings in the main

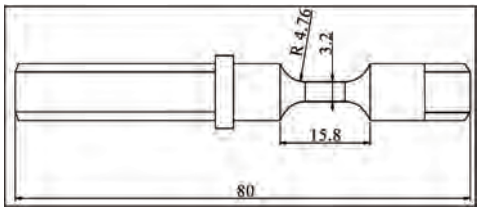

Figure 1. Stress corrosion test specimen (dimensions in mm)

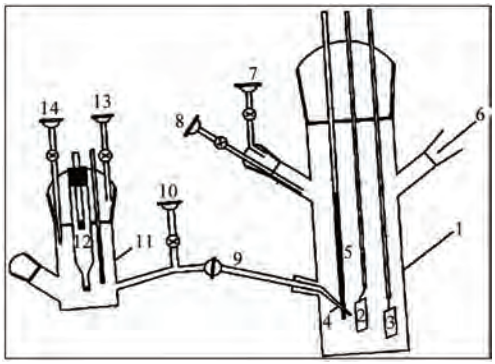

Figure 2. Electrochemical polarization cell (schematic): 1) Main compartment; 2) Specimen/working electrode; 3) Platinum electrode; 4) Luggin capillary; 5) Thermometer; 6) To condenser and gas outlet; 7, 13) Solution inlet; 8, 14) Gas inlet; 9) Salt bridge; 10) Gas Outlet; 11) Reference compartment; 12) Saturated calomel reference electrode

compartment, one for water condenser, and the other for gas and solution inlet, when working with de-aerated system. The reference compartment has a thermometer gas inlet and liquid inlet together with the saturated calomel electrode in one joint. The cell capacity was 0.4 dm^3 of test solution. Only the main compartment of the cell was immersed in an oil bath controlling the required temperature, the reference compartment being held at room temperature.

2.3.2 Stress Corrosion Measurements

The majority of the work was conducted using a constant load method. The tensile properties of the material were measured in triplicate, on an Instron Tensile Testing Machine. In all the constant load tests the load applied was 90% of the predetermined yield stress.

For electrochemical measurements on stressed specimens, a glass cell comprising of two compartments, the main compartment contained the stress corrosion specimen and the platinum counter electrode. The reference compartment contained saturated calomel electrode, similar to the reference compartment described before. The two compartments were connected by a salt bridge with a Luggin capillary. The capacity of the cell was 0.25 dm^3, and the details are shown in Figure 3. To identify the reproducibility of the polarization curves, measurements were performed for three or more samples in one solution condition. Some scatter in the open circuit potential (OCP) and the active-passive transition potentials were found in the polarization curves determined in some tests.

3. Results and Discussions

The entire stress corrosion test carried out under a constant load of 90% of the yield stress (206.5 MNm^{-2}).

In this work effect of temperature and concentration were considered.

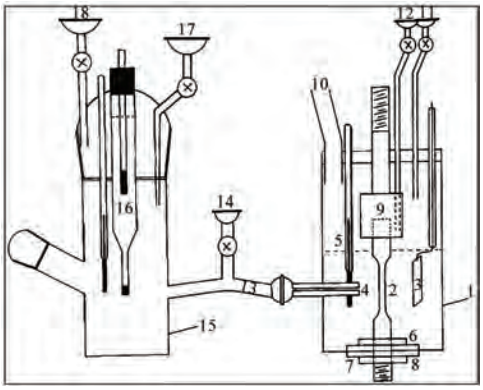

Figure 3. Stress corrosion test cell (schematic): 1) Main compartment; 2) Specimen/ working electrode; 3) Platinum electrode; 4) Luggin capillary; 5) Thermometer; 6) P.T.F.E nut; 7) Rubber washers; 8) Stainless steel nut; 9) Top shackle; 10) To condenser and gas outlet; 11, 18) Solution inlets; 12, 17) Gas inlets; 13) Salt bridge outlet; 14) Gas outlet; 15) Reference compartment; 16) Saturated calomel reference electrode

3.1 Effect of Temperature

3.1.1 Stress Corrosion Life

A solution of 52Wt% NH_4NO_3 at different temperature was used to determine the stress corrosion life. The results are summarized in Table 1.

Figure 4 shows the temperature dependence of stress corrosion life and general corrosion rate. This figure indicates that the stress corrosion life decreased as the temperature was increased. The general corrosion in 52Wt% NH_4N0_3 at the boiling point (383 K) was very severe, the gauge length of a stress corrosion specimen, left in such a solution for 108 ks without applied stress, dissolved to a point as shown in Figure 5. A similar specimen immersed in the solution at 368 K for about 1.3 Ms showed a reduction in Ultimate Tensile Stress (UTS) of only 13%, with maximum intergranular attack 3 grains in depth.

Table 1. Effect of temperature on stress corrosion life of mild steel in 52Wt% ammonium nitrate solution (stress= 206.5 MN m^{-2})

Temperature K	Number of Tests	Average Stress Corrosion Life ks	95% Confidence Limits of Life ks
303	2	>7300.0	-
323	3	352.0	±108.0
343	4	145.8	± 57.2
358	4	69.8	± 32.0
368	7	27.3	± 9.6
375	4	22.3	± 20.9
380	4	23.4	± 9.7
383	5	18.3	± 7.8

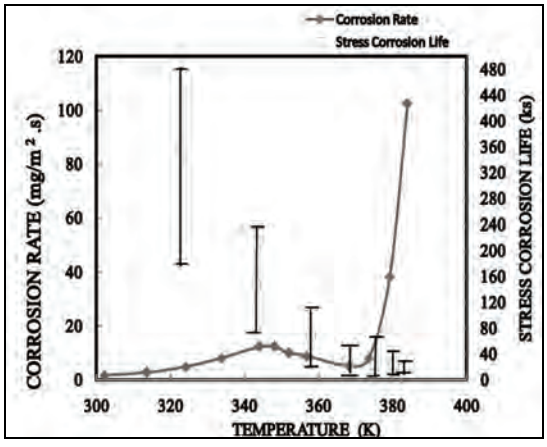

Figure 4. Effect of temperature on the general corrosion rate and stress corrosion life of mild steel in 52Wt% NH_4NO_3 solutions

Figure 5. Stress corrosion test specimen after 108 ks immersion in 52Wt% NH_4NO_3 solutions at boiling point (383 K). Very high general corrosion attack X 12

Microscopical examination of longitudinal sections of specimens stress corroded at different temperatures showed the features indicated in Table 2.

Length of the section: 6.6 mm.
Grain diameter: 40 µm.
Width of the section: 2.5 mm.
Type A: Just detectable intergranular attack,
Type B: Fine cracks,
Type C: Wide cracks,
Type D: Cracks visible to the naked eye.

Table 2. Effect of temperature on the stress corrosion of mild steel in 52Wt% ammonium nitrate solution

Temperature K	Average Stress Corrosion Life ks	Type of attack and No. of Locations				Maximum Depth of Penetration in Grains	Reduction in Diameter µm
		A	B	C	D		
323	352	3				1	-
343	145.8			7		6	203
358	698		3			6	76
368	27.3			6	1	44	8
375	22.3		3		1	15	-
380	23.4		4		1	18	-
383	18.3				3	-	228

It appears from Table 2 that the susceptibility in the range 368 K to 380 K was greater than at other temperatures. The higher susceptibility to cracking at higher temperature may be attributed to the nature of the corrosion product formed. Crack morphologies and crack features on the crack surface were observed by scanning electron microscope (SEM). Figure 6 shows the fracture surface morphology of specimen after stress corrosion failure in 52Wt% NH_4NO_3 solution at 368K which indicates high degree of intergranular attack. Previous work of Evans [10] showed that at high temperatures in the nitrate solution, anhydrous magnetite film that has high ionic conductivity is formed.

Our experiment illustrated that at the boiling point, the cracking was associated with a high rate of general corrosion while previous work reported that stress corrosion failure occurs only in hot and boiling nitrate solutions [1].

The 368 K was chosen as the test temperature because the stress corrosion life was reasonably short, with less scatter than at other temperatures, and the general corrosion attack was not severe.

Karthik *et al.* [11] reported that the temperature effect was hypothesized to be associated with oxygen presence, since the solubility at 333 K is greater than that at 368 K. These results confirm that the temperature effect in the presence of nitrate is associated with oxygen availability. Stress corrosion cracking usually occurs under the conditions where a component is exposed to a mildly corrosive environment while under stress (applied or residual) [12].

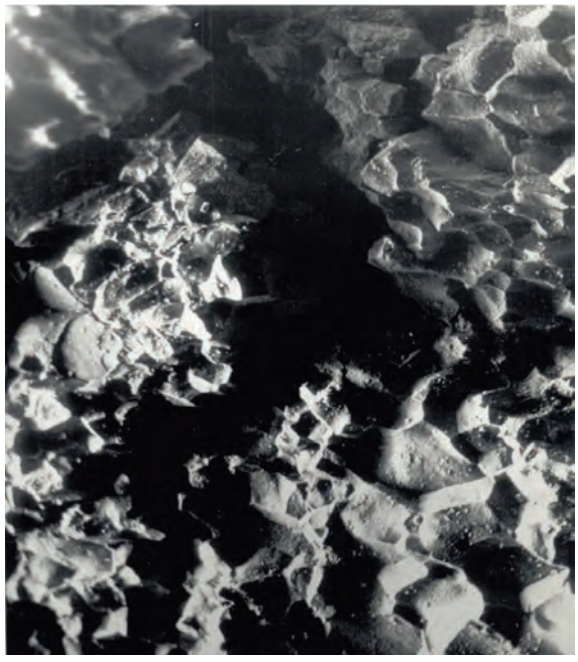

Figure 6. Fracture surface morphology of a specimen after stress corrosion failure in 52Wt% NH_4NO_3 solutions at 368 K, showing the high degree of intergranular attack X 250

Tang *et al.* [13] stated that a stress concentration is developed at the crack-tip and enhances significantly the local anodic dissolution. Also the presence of crack in steel would generate significant stress concentration, resulting in remarkable enhancement of local anodic dissolution rate.

3.1.2 Electrochemical Measurements of Mild Steel Specimen in Ammonium Nitrate Solution

1) Corrosion potential/time curves

Figure 7 shows variation of corrosion potential with time in 52Wt% NH_4NO_3 solutions at temperatures ranging from 298 K to 368 K.

At 368 K corrosion potential was nobler than at any other temperature. It appears that the aggressiveness of particular nitrate solution may well be indicated by measurement of the potential of metal in that solution. The corrosion potential behavior gives some indication of the processes which may be occurring. A lower general corrosion rate at higher temperature is indicated by the fact that the corrosion potential shifts to more noble values are greater at these temperatures. This shift could be due to the formation and growth of a Fe_2O_3 film on the corroding surface. At temperatures of 345 K and above, there was some oscillation in the corrosion potential before it attained a steady value. If the initial potential is considered, then the shortest life appears to correspond with nobler potential Figures 4 and 7.

2) Potentiodynamic polarization curves

Figure 8 shows the Potentiodynamic polarization curves in 52Wt% NH_4NO_3 solution at temperature ranging from 298 K to 368 K using a sweep rate of 0.33 $mV.s^{-1}$ starting approximately 350 mV more negative than the open circuit potential (OCP) and scanning in the noble direction to more than 1200 mV.

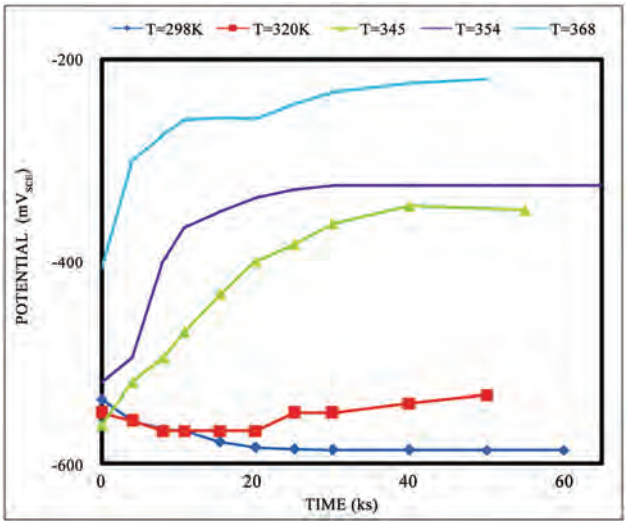

Figure 7. Effect of temperature on the corrosion potential/ time behavior of mild steel in 52Wt% ammonium nitrate solutions

These curves indicate that decreasing the temperature promoted the formation of a more protective passivating film. The increase in temperature to 368 K shifted the corrosion potential to a higher value and increases the active peak current. Edgemon *et al.* [14] perform tests using mild steel in simulated waste solutions which primarily composed of ammonium nitrate and when held at approximately 370 K. Data characteristic of uniform and stress corrosion cracking are presented.

3.2 Effect of Concentration

3.2.1 Stress Corrosion Life

The influence of concentration of ammonium nitrate solution at 368 K on the stress corrosion life is shown in Table 3 and is plotted in Figure 9. The life decreases as the concentration increased. Microscopic examination of specimens after stress corrosion testing in 10Wt%, 20Wt% and 52Wt% NH_4NO_3 solution revealed that in all cases, there was severe intergranular attack, especially at the high concentrations.

3.2.2 Electrochemical Measurements on Unstressed Specimens

1) Corrosion potential/time curves

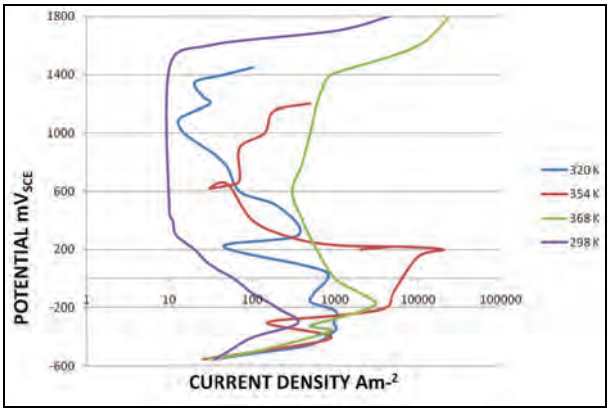

Figure 8. Effect of temperature on the Potentiodynamic polarization behavior of mild steel in 52Wt% ammonium nitrate solutions

Table 3. Effect of concentration of NH_4NO_3 solution on the stress corrosion life of mild steel at 368 K (stress=206.5 NM m^{-2})

Concentration of NH_4NO_3 Wt %	Number of Tests	Average Stress Corrosion Life ks	95% Confidence Limits of Life ks
10	4	45.0	± 30.0
20	9	60.5	± 23.7
30	4	27.4	± 16.6
40	4	27.4	± 13.0
52	7	27.3	± 9.6
70	4	20.9	± 9.4

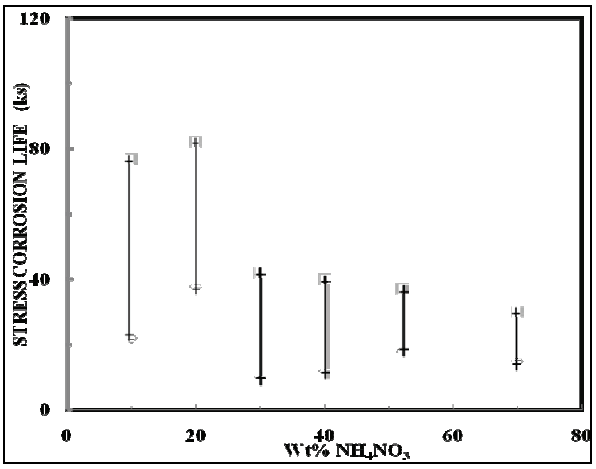

Figure 9. Effect of NH_4NO_3 concentration on the stress corrosion life of mild steel at 368 K

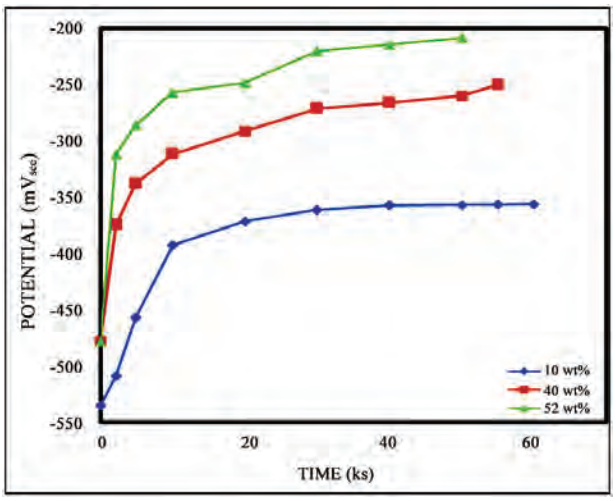

Figure 10. Effect of NH_4NO_3 concentration on the corrosion potential/time behavior of mild steel at 368 K

The variation of the corrosion potentials with time in 10Wt%, 40Wt%, and 52Wt% NH_4NO_3 solution at 368 K is plotted in Figure 10. At this temperature the oxide film apparently forms faster at high concentration and it has better protective properties. The corrosion potential became nobler as the concentration increased.

2) Potentiodynamic polarization curves

Figure 11 shows the Potentiodynamic polarization curves in different concentrations of ammonium nitrate solutions at 368 K using a sweep rate of 0.33 $mV.s^{-1}$ starting approximately 300 mV more negative than the (OCP) and scanning in the noble direction to more than +1400mV. There are wide active regions, high passivation potentials and the high critical passivation current at lower concentrations. In all concentrations there was a very high rate of attack, but the morphology differed. In the following sections 52Wt% NH_4NO_3 solution at 368 K was used as the aggressive environment. Preliminary work has shown that general corrosion was minimum at 368 K, a temperature at which the stress corrosion life was relatively short, with little scatter in the results Figure 4. The concentration of 52Wt% NH_4NO_3 was chosen as a compromise Figure 9, as too low concentration results in too long stress corrosion life, whilst the stress corrosion life in 70Wt% solution was approximately the same as that in 52Wt%.

At high concentrations, the passivating ability of the solution will increase, this means that the time required to produce a film having the critical properties required for crack initiation will decrease. These curves indicate a decrease in the stress corrosion life with increasing concentration as reported by previous workers for different nitrate solutions [7,14,15].

As a second stage of work, further areas in which investigation will be rewarding include:

a) The effect of PH level.

b) Oxygen concentration.

c) The stages of stress corrosion failure.

This will help to define and establish effective and efficient corrosion mitigation strategies such as using inhibitors to stop this phenomenon.

3) Potentiostatic polarization

The behavior of specimens under different applied potentials ranging from -500mV to +900mV in 52Wt% ammonium nitrate solution at 368 K was investigated and the current was recorded during the test.

In Figure 12, the current behavior with the applied potential can be divided into three groups:

a) (-500 to -150 mV) high initial current density, followed by very fast decrease which indicates a high tendency for passivation.

b) (Zero to +100 mV) the initial current density is very high and remains at this high value for approximately 1 ks subsequently there are some periodic reduction in the rate

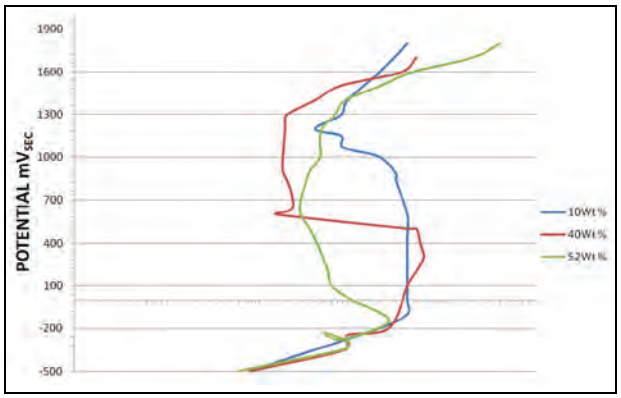

Figure 11. Effect of NH_4NO_3 concentration on the potentiodynamic anodic polarization behavior of mild steel at 368 K

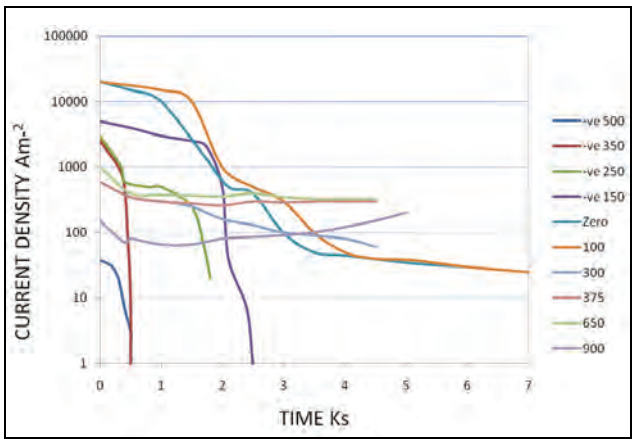

Figure 12. Potentiostatic anodic polarization behavior of mild steel in 52Wt% NH_4NO_3 solutions at 368 K

of current decrease at these potentials, with a relatively high value and current densities remain constant even after 6 ks. This indicates quite active conditions with very slow formation of oxide film, which are not favorable for stress corrosion, demonstrating that corrosion is probably occurring at these potential. Moderate decrease, indicates regions between active and passive state.

c) (+300 to 900 mV) Very slow decrease at the beginning, which indicates a very active state, followed by an approximately constant region.

4. Conclusions

The effect of temperature and concentration of ammonium nitrate solution on the stress corrosion life of mild steel is as follows:

1) An increase in temperature causes a decrease in the stress corrosion life. The relative roles of general corrosion and stress corrosion cracking in producing failure became difficult to separate at temperatures near the boiling point.
2) An increase in concentration (at 368 K) causes a decrease in the stress corrosion life.
3) The OCP of mild steel measured in 52% ammonium nitrate solution at 368 k was in the range -230 to -260 mV (SCE).
4) Stress corrosion cracking occurs only when the mild steel in particular solution conditions exhibits well defined active passive behavior.
5) Detailed study of the effect of pH level, oxygen concentration, stages of stress corrosion cracking failure and other factors is required. This will help in establishing effective corrosion mitigation to stop the stress corrosion cracking.

REFERENCES

[1] H. T. Engell and A. Baumel, In T. N. Rhodin (ed.), Physical Metallurgy of Stress Corrosion Fracture, Interscience Publishers, New York, pp. 341, 1959.

[2] Z. Szklarska-Smialowska, "Effect of potential of mild steel on stress corrosion cracking in ammonium nitrate solutions," Corrosion Journal, Vol. 20, pp. 198–201, 1964.

[3] M. Smialowski and Z. Szklarska, "Corrosion of iron in solutions containing ammonium nitrate," Corrosion Journal, Vol. 18, pp. 1–4, 1962.

[4] J. A. S. Green and R. N. Parkins, "Electrochemical properties of ferrite and cementite in relation to stress corrosion of mild steel in nitrate solutions," Corrosion Journal, Vol. 24, pp. 66–69, 1968.

[5] M. Henthorne and R. N. Parkins, "Some aspects of stress-corrosion cracking propagation in mild steel," Corrosion Science, Vol. 6, pp. 357–369, 1966.

[6] J. Flis and J. C. Scully, "Transmission electron microscopical study of corrosion and stress-corrosion of mild steel in nitrate solution," Corrosion Science, Vol. 8, p. 235–244, 1968.

[7] H. R. Baker and C. B. Singleterry, "Effect of some electrolytes on the stress corrosion cracking of AISI 4340 steel," Corrosion Journal, Vol. 28, pp. 340-344, 1972.

[8] R. W. Staehle, "Framework for predicting stress corrosion cracking," Proceedings of Environmentally Assisted Cracking: Predictive Methods for Risk Assessment and Evaluation of Materials, Equipment, and Structures, Orlando, STP1401, pp. 131–165, 2000.

[9] R. G. I Leferink and W. M. M. Huijberjts C., "Nitrate stress corrosion cracking in waste heat recovery boilers," Anti-Corrosion Method & Materials, Vol. 49, pp. 118–126, 2002.

[10] U. R. Evans, "The corrosion and oxidation of metal," Edward Arnold Ltd., London, pp. 324, 1960.

[11] Karthik Subramanian and John Mickalonis, "Anodic polarization behavior of low carbon steel in concentrated sodium hydroxide and sodium nitrate solutions," Electrochimica Acta, Vol. 50, pp. 2685–2691, 2005.

[12] S. J. Suess, "Case histories involving stress corrosion cracking of various alloys," Corrosion Journal, Vol. 64, pp. 401–419, 2008.

[13] X. Tang and Y. F. Cheng, "Micro-electrochemical characterization of the effect of applied stress on local anodic dissolution behavior of pipeline steel under near-neutral pH condition," Electrochemica Acta, Vol. 54, Issue 5, pp. 1499–1505, 2009.

[14] G. L. Edgemon, M. J. Danielson, and G. E. C. Bell, "Detection of stress corrosion cracking and general corrosion of mild steel in simulated defense nuclear waste solutions using electrochemical noise analysis," Journal of Nuclear Materials, Vol. 245, pp. 201–209, 1997.

[15] J. L. Nelson *et al.* "Hanford DST corrosion monitoring instrument tree," Corrosion, Paper No. 440, Houston, TX: NACE International, 1995.

J. Electromagnetic Analysis & Applications, **2010, 2: 98-103**
doi:10.4236/jemaa.2010.22014 Published Online February 2010 (www.SciRP.org/journal/jemaa)

Scientific Research

Compact Narrow Band Non-Degenerate Dual-Mode Microstrip Filter with Etched Square Lattices

P. K. Singhal, Suman Mathur, R. N. Baral

Department of Electronics, Madhav Institute of Technology and Science, Gwalior, India.
Email: pks_65@yahoo.com

Received September 11th, 2009; revised October 13th, 2009; accepted October 17th, 2009.

ABSTRACT

A compact narrowband non-degenerate dual-mode microstrip filter with square shape cuts is presented. The structure is developed by loading the conventional non-degenerate dual-mode resonator by open circuit stubs at two opposite corners. The filter bandwidth is controlled by only decreasing the higher cutoff frequency of the conventional type. With Square shape cuts, return loss is improved. A 20% fractional bandwidth filter is designed and implemented on FR4 material with 4.4 dielectric constant and 1.6 mm thickness at center frequency of 1.5 GHz with passband of 1.3 GHz to 1.6 GHz. Analysis has been achieved using the IE3D simulator. Experimental results do agree with simulations.

***Keywords*:** *Microstrip, Dual Mode, Narrowband Filter, Square Patch Resonator*

1. Introduction

Now-a-days compact microwave filters are widely used in various wireless communication applications. Dual-mode resonators have been used for such purposes. Each of dual-mode resonators act as a doubly tuned resonant circuit and therefore the number of resonators required for a given filter is reduced by half, resulting in a compact configuration. Dual-mode microstrip resonators have the advantages of low profile, simple fabrication, ease of integration in addition to low cost. The first microstrip dual-mode filter was presented by Wolff [1] in 1972. Degenerate modes based filters have been investigated in various topologies such as square patch [2], circular patch, triangular patch, square loop [3], circular ring [4] and meander shape [5]. Square and circular patches structures have negligible conductor loss but suffer from higher radiation loss. However, square loop and circular ring structures have less radiation loss but suffer from higher conductor loss, especially for thin strip conductors [2]. Degenerate dual mode filters have usually narrow bandwidth of (< %5). Filters with higher bandwidth up to 25% have been investigated using non-degenerate dual-mode structure [6–7].

2. Proposed Structure and Modes of Operation

The fields within a square patch resonator can be expanded by the TM^z_{mn0} modes [2], where 'z' is perpendicular to the ground plane. The two fundamental degenerate modes correspond to TM^z_{100} and TM^z_{010} and the first higher order mode correspond to TM^z_{110} [6]. These three modes can be excited simultaneously by a square shape resonator with feed lines, as shown in Figure 1. The simulated response is shown in Figure 2.

The etching of slots in square patch resonator as shown in Figure 3 decreases the resonance frequencies of the

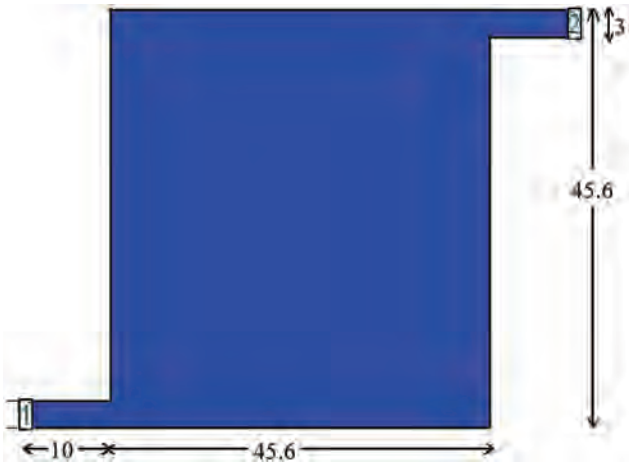

Figure 1. Layout of square patch resonator with feed lines (All dimensions are in mm)

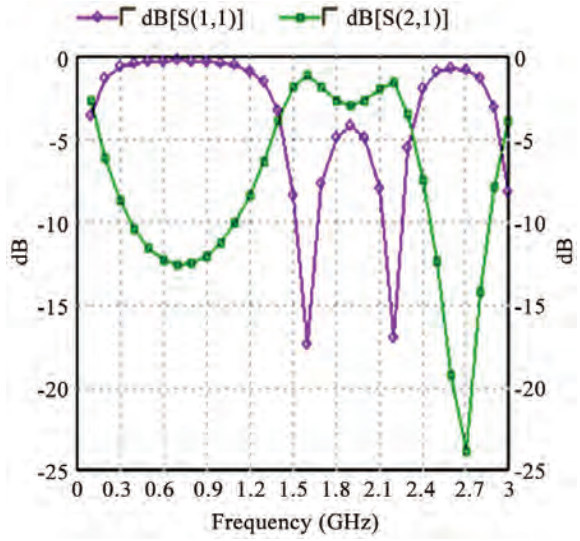

Figure 2. Simulated response of square patch resonator with feed lines

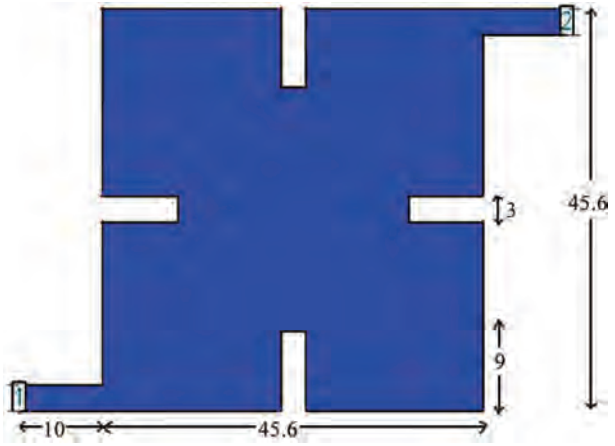

Figure 3. Layout of square patch resonator after etching slots (All dimensions are in mm)

three modes but the resonance frequency of the mode TM^{z}_{110} decreases faster. Therefore, band pass filter behavior can be obtained [7]. This is shown in Figure 4. The resultant size and bandwidth decreases as the slot length increases. The square patch has a length W, while the slots have equal lengths L and width S. The physical dimensions of the simulated patch are W = 45.6 mm, L = 9 mm and S = 3 mm. Denoting f_1 as the resonance frequency of the degenerate modes TM^{z}_{100} and TM^{z}_{010} and f_2 as the resonance frequency of the mode TM^{z}_{110}. The effect of the slots length L on the resonance frequencies f_1 and f_2 for the patch is that the two resonance frequencies, f_1 and f_2, decrease as L increases [7]. The difference f_2 - f_1 can be used as first approximation of the possible bandwidth of the filter. For L = 9 mm, a fractional bandwidth of about 33% can be obtained using the given parameters.

Based on this design configuration, it is difficult to achieve bandwidth less than this value. However, loading the patch by open circuit stubs as shown in Figure 5 will decrease the resonance frequency f_2 of the mode TM^{z}_{110} and approximately maintains the resonance frequency of the degenerate modes constant. Therefore, band pass filters with fractional bandwidth less than 25% can be achieved.

The layout of the filter with the stubs of width 1 mm and length 12 mm can be seen in Figure 5. The subsequent effect on the resonance frequencies f_1 and f_2 is

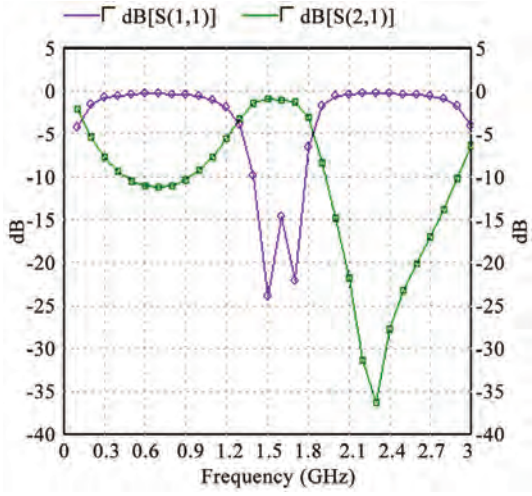

Figure 4. Simulated response of square patch resonator after etching slots

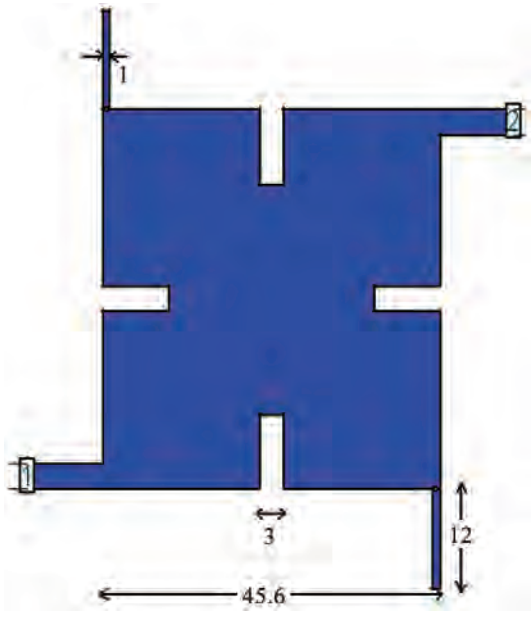

Figure 5. Layout of non-degenerate dual-mode filter with stubs of length 12 mm

shown in Figure 6. This analysis is carried out using the moments method IE3D simulator, on a conducting patch of W = 45.6 mm on a substrate of dielectric constant 4.4, with height 1.6 mm. The slot length and width used are 9 mm and 3 mm, respectively. These parameters have been chosen to fix f_1 at 1.3 GHz.

As described in the previous section, almost no effect is observed on the resonance frequency of the first two degenerate modes TM^z_{100} and TM^z_{010}. The resonance frequency of these modes f_1 is almost constant and equal to 1.3 GHz for stubs length of 0 to 18 mm. However, the first higher order mode TM^z_{110} is highly affected and its resonance frequency f_2 decreases. This variation allows the design of narrow band filter, with careful control of its bandwidth. Bandwidth selection can be obtained by first choosing f_1 and then finding the appropriate stub lengths for a specific value of f_2.

3. Filter Design Parameters

For the proposed narrowband band pass filter the design parameters are:

Dielectric Constant = 4.4,

Height of Substrate = 1.6 mm,

Corresponding length of the Square patch, W = 45.6 mm,

Corresponding width of the slots, S = 3mm,

Corresponding length of the slots, L = 9mm,

Corresponding width of the stubs, W_s = 1mm,

Corresponding length of the stubs, L_s = 16mm,

The layout of the non-degenerate dual-mode filter with stubs of length 16 mm is shown in Figure 7 and Figure 8 shows the fractional bandwidth obtained is about 20% in

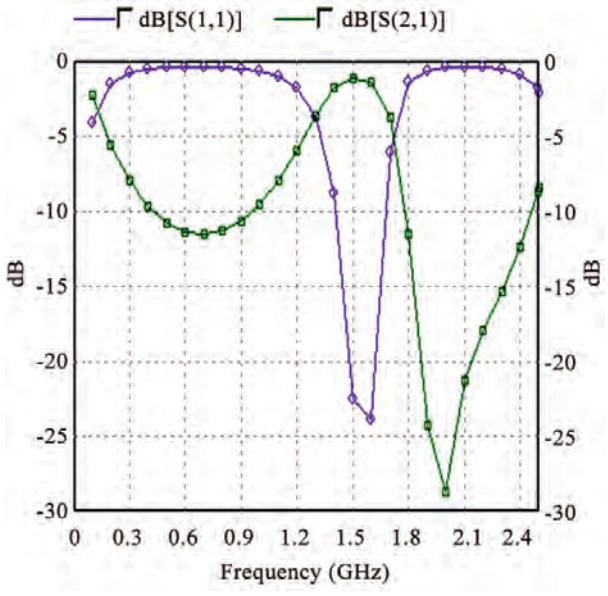

Figure 6. Simulated response of non-degenerate dual-mode filter with stubs of length 12 mm

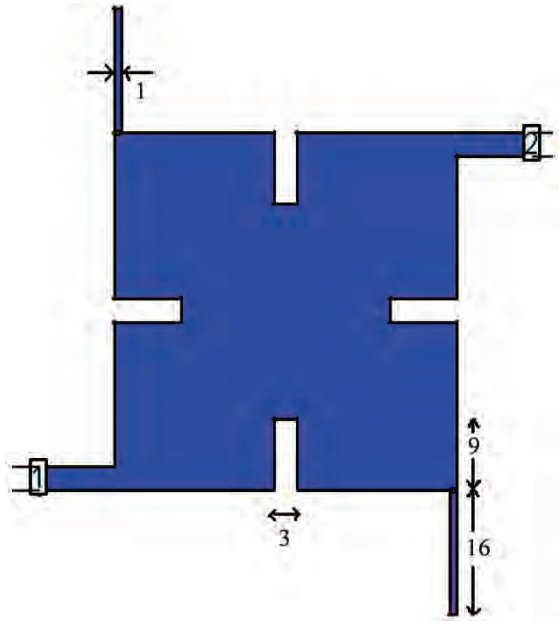

Figure 7. Layout of the dual-mode filter with stubs of length 16 mm

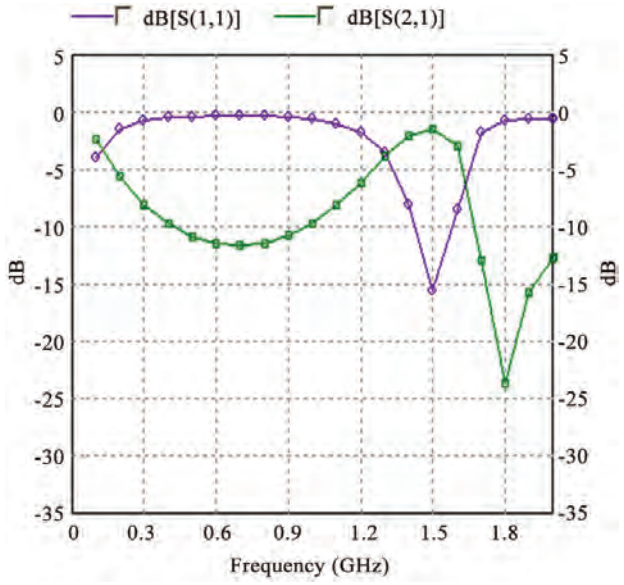

Figure 8. Simulated response of dual-mode filter with stubs of length 16mm

the passband 1.3 GHz -1.6 GHz and the return loss is found to be 15.11dB. The layout as shown in Figure 9, is obtained after etching one square lattice of dimension of 6 mm × 6 mm, on the center of the conventional non-degenerate dual mode filter. The corresponding return loss of the bandpass filter at the center frequency is found to be improved and becomes 22.56 dB. The fabricated layout is shown in Figure 10. The simulated and measured results are shown in Figures 11, 12.

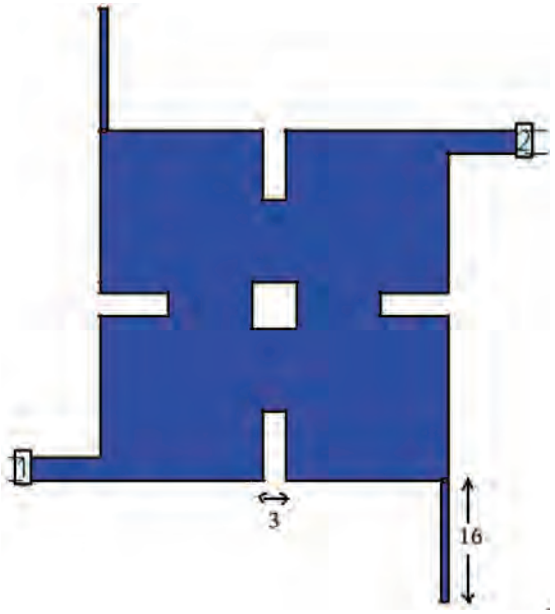

Figure 9. Layout of the non-degenerate dual mode filter with etching of one square lattice

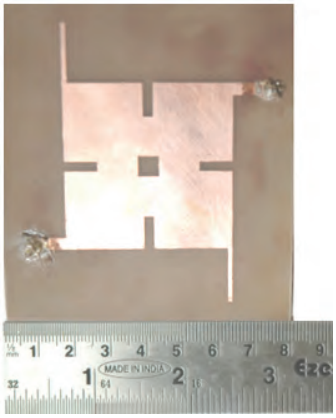

Figure 10. Photographed layout of non-degenerate dual mode filter with etching of one square lattice

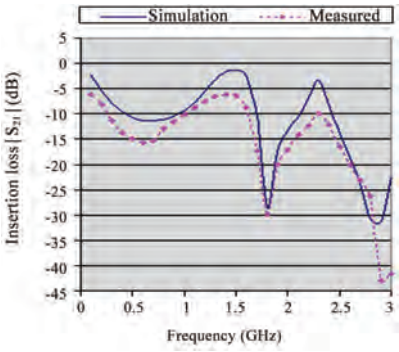

Figure 11. Simulated and measured results of insertion loss of non-degenerate dual mode filter with etching of one square lattice

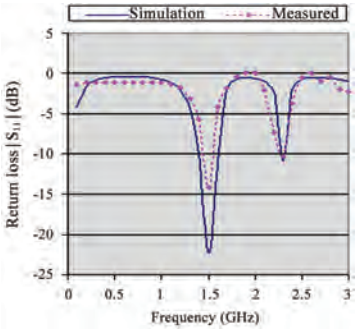

Figure 12. Simulated and measured results of return loss of non-degenerate dual mode filter with etching of one square lattice

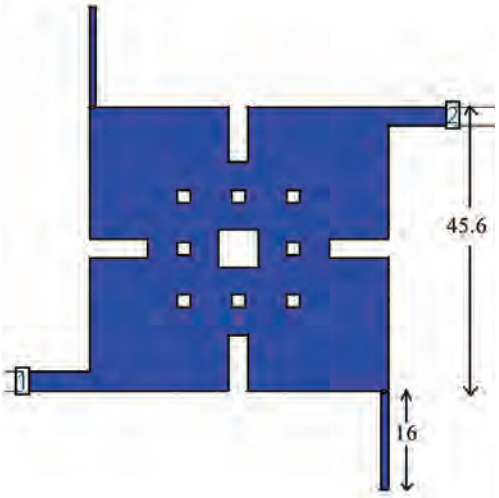

Figure 13. Layout of the non-degenerate dual mode filter with eight square lattices

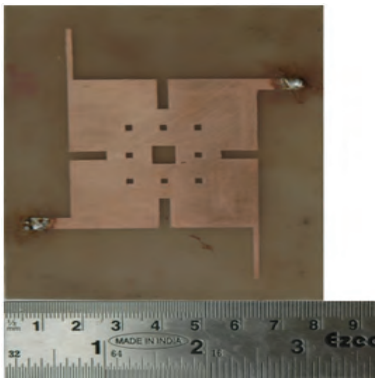

Figure 14. Photographed layout of the non-degenerate dual mode filter with eight square lattices

Now, with additional eight small square lattices of dimension 2mm × 2mm etched as shown in Figure 13, the frequency response can further be improved as shown in Figures 14, 15. The return loss now is 26.12 dB. Figure

16 shows the fabricated layout of the non-degenerate dual mode filter with eight square lattices.

Figure 17 shows the layout of non-degenerate dual mode filter with a carpet of square lattices of very small dimension 1mm × 1mm. It further improves the return loss to 30.06 dB which is shown in Figure 18.

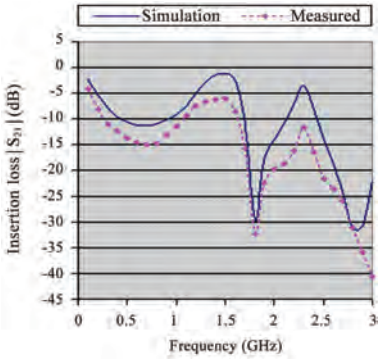

Figure 15. Simulated and measured insertion loss plots for non-degenerate dual mode filter with eight small square lattices

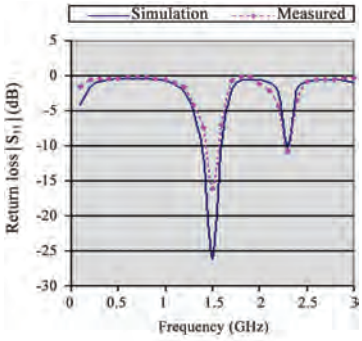

Figure 16. Simulated and measured return loss plots for non-degenerate dual mode filter with eight small square lattices

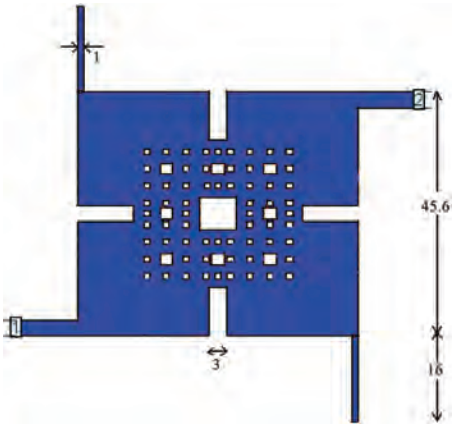

Figure 17. Layout of non-degenerate dual mode filter with carpet square lattices

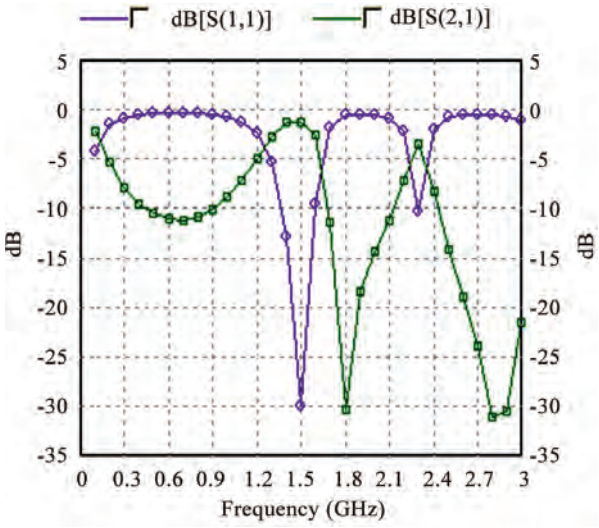

Figure 18. Simulated response of non-degenerate dual mode filter with carpet square lattice

4. Conclusions

A compact narrow band filter based on non-degenerate dual-mode resonator is proposed. The narrow bandwidth characteristic is achieved by loading the slotted square patch at opposite corners. Such loading affect only the higher cutoff frequency of the filter. The effect of this loading has been discussed.

For improved performance in terms of return loss for the narrowband band pass filter, square shape lattices of different dimensions etched on the conventional design. It significantly improves the return loss with 30.06 dB at the center frequency. Hence, a narrowband filter of fractional bandwidth 20% is designed and implemented with better performance on transmission and reception. Good agreement between simulated and measured responses is observed.

5. Acknowledgment

The authors thankfully acknowledge the financial support provided by All India Council of Technical Education, New Delhi, India.

REFERENCES

[1] I. Wolff, “Microsrtip bandpass filter using degenerate modes of microstrip ring resonator,” Electron Letter, Vol.8, No. 12, pp. 302–303, 1972.

[2] J. S. Hong and M. J. Lancaster, “Microstrip filters for RF/Microwave applications,” John Wiley & Sons, Inc., New York, 2001.

[3] J. S. Hong and M. J. Lancaster, “Bandpass characteristics of new dual-mode microstrip square loop resonators,” Electronic Letter, Vol. 31, pp. 891–892, 1995.

[4] J. C. Liu, C. S. Cheng, and L. Yao, “Dual-mode dou-

ble-ring resonator for microstrip band-pass filter design," Microwave Optical Technology Letter, Vol. 36, pp. 310–314, 2003.

[5] J. S. Hong and M. J. Lancaster, "Microstrip bandpass filter using degenerate modes of a novel meander loop resonator," IEEE Microwave Quided Wave Letter, Vol. 5, No. 11, pp. 371–372, 1995.

[6] A. F. Sheta, N. Dib, and A. Mohra, "Investigation of new non degenerate dual-mode microstrip patch filter," IEEE Proceedings-Microwave Antennas Propagation, Vol. 153, No. 1, pp. 89–95, 2006.

[7] A. F. Sheta, "Narrow band compact non-degenerate dual-mode microstrip filter," 25th National radio science conference (NRSC'08), Faculty of Engineering, Tanta University, 2008.

[8] G. Mattaei, L. Young, and E. M. T. Jones, "Microwave filters, impedance matching networks, and coupling structures," Artech House, Norwood, MA, 1980.

J. Electromagnetic Analysis & Applications, 2010, 2: 104-110
doi:10.4236/jemaa.2010.22015 Published Online February 2010 (www.SciRP.org/journal/jemaa)

Scientific Research

Low-Loss, Broadband and Tunable Negative Refractive Index Metamaterial

Yongjun Huang[1], Guangjun Wen[1], Tianqian Li[1], Kang Xie[2]

[1]School of Communication and Information Engineering, University of Electronic Science and Technology of China, Chengdu, China;
[2]School of Opto-Electronic Information, University of Electronic Science and Technology of China, Chengdu, China.
Email: yongjunh@uestc.edu.cn, wgj@uestc.edu.cn, keguai2007@163.com

Received October 10th, 2009; revised November 22nd, 2009; accepted November 28th, 2009.

ABSTRACT

This paper report on a low-loss, broadband, and tunable negative refractive index metamaterial (*NRIM*) *consisting of yttrium iron garnet* (*YIG*) *slabs and printed circuit boards* (*PCBs*). *The YIG slabs under an applied magnetic field provide a negative permeability and the PCBs provide a negative permittivity. The substrates of the PCBs decuple the interactions between the YIG slabs and wire array deposed on such substrates. The effective electromagnetic parameters of the NRIM and the conditions of exhibiting the negative refractive index character are analyzed theoretically. Then the negative transmission and negative refraction characters are investigated numerically and experimentally. The results indicate that the NRIM exhibits negative pass band within the X-band with a bandwidth of about 1 GHz and a peak transmission power of about* - 2.5 *dB. While changing the applied magnetic field from* 2300 *Oe to* 2700 *Oe, the measured pass band of NRIM shift from* 8.42 *GHz to* 9.50 *GHz with a* 2.7 *MHz/Oe step. The results open a sample way to fabricate the NRIM, further, the metamaterial cloak and absorber.*

***Keywords*:** *Metamaterial, Negative Refractive Index, Tunability, Low-Loss, Broadband*

1. Introduction

Since the negative refractive index metamaterial (NRIM) predicted by Veselago [1] was experimentally realized by Smith *et al*. [2] and verified by Shelby *et al*. [3] through negative refraction in a prism sample, much attention has been attracted on designing various NRIMs [4–9] and investigating applications [10,11]. Much of the fascination in NRIMs arises from their unusual electromagnetic properties such as the reversals of both Doppler shift and Cherenkov radiation [1], enhancement of evanescent wave [12], and subwavelength resolution imaging [13], etc. In the various NRIMs, most of them are realized by artificial metallic structures with metallic plasma resonance such as using wires to produce effective negative permittivity and using split-ring resonators (SRR) to provide effective negative permeability [2,14,15]. Recently, the investigations of electromagnetic cloak of invisibility based on the metallic plasma resonance structure metamaterial [16] have generated great interests [17]. However, most NRIMs proposed to date are based on immutable structure of the unit cell and result in a narrow band and not at all tunable.

In order to fabricate a broadband and tunable NRIM, the SRR structure resulting in the narrow band and untunability must be replaced by some other structures or materials. Some researchers proposed ferrimagnet based NRIM, that is, substitute ferrimagnet such as yttrium iron garnet (YIG) for the SRR structure to obtain the negative permeability [18–22]. Dewar gave the theoretical expressions of the effective parameters and analyzed the interaction of the ferrites and wires [18]. Cao *et al*. numerically investigated the electromagnetic wave propagation properties of the NRIM [19]. However such model cannot be fabricated easily in actually. Cai at al. proposed a simple way to fabricate the NRIM with ferrimagnet slabs and wire array [20]. Zhao *et al*. and He *et al*. fabricated the NRIM sample and investigated experimentally the negative transmission and tunability characters [21,22]. However, these authors mentioned above did not directly measure the refraction index character. They did not optimize the parameters so that the NRIM exhibits a low loss and reflection. And the most important thing is that they did not investigate the strategies for minimizing the loss when the NRIM is fabricated experimentally. Since the loss is a serious problem when the NRIM is used in engineering areas, we need to determine ways to reduce it, especially at high frequencies.

The aim of this work is to provide a low-loss, broadband, and tunable NRIM consisting of YIG slabs and

printed circuit boards (PCBs). The YIG slabs under applied magnetic field give rise to a negative permeability and the PCBs provide a negative permittivity. This NRIM is designed because there are some advantages. For instance, it can be easily fabricated with YIG slabs and PCBs. The thickness of the wire depositing on PCBs has a very small value so that the frequency band in which the refraction index is negative can be achieved to far infrared and optical frequencies. And the interaction between YIG slabs and wires can be easily reduced by using the substrate layers.

In this paper we present the model of the NRIM and give the fabricated parameter values based on the theoretical analysis. Then we give the approximate theoretical results of the effective permeability and permittivity of the NRIM. The EM transmission properties are numerically investigated by using ANSOFT's High Frequency Structure Simulator (HFSS) tools. In the end we experimentally investigate the negative transmission, tunability, and negative refraction properties by testing the NRIM sample in X-band rectangular waveguide.

2. Design and Fabrication

To design a low-loss, broadband, and tunable NRIM, the ferrimagnet is used to replace the SRR structures to provide the negative permeability. The PCBs are used to obtain the negative permittivity. The ferrimagnet has some particular properties. For instance, the loss in ferrimagnet is much smaller than typical conductor SRR [2], the effective permeability of ferrimagnet under the applied magnetic field is negative within a broad frequency band, and the frequency band of negative permeability can be dynamically and continuously tuned by changing the applied magnetic field. So the ferrimagnet is a desirable candidate to fabricate the tunable NRIM. However, the ferrimagnet under applied magnetic field would damage the negative permittivity of wire array. It can be reduced by using an insulating and nonmagnetic dielectric material [18] and the dielectric material must also be low-loss.

Consequently, based on the above analysis, the schematic of the NRIM is designed and presented in Figure 1. The structure parameters are also designed properly by numerical optimization. The yttrium iron garnet (YIG) slabs are used to give rise to negative permeability. Each slab has a dimension of 22.86 × 10.16 × 1 mm^3, a saturation magnetization of 1830 Gs (1 Gs = $10^3/(4\pi)$ A/m), and a line width of about 22 Oe (1 Oe =$10^3/(4\pi)$ A/m). The substrates of PCBs, which are made from RT/duriod 5880 glass microfiber reinforced PTFE composites, are used to reduce the interaction between YIG slabs and wire array. Each PCB has a dimension of 22.86 × 10.16 ×0.254 mm^3. The wires depositing on the substrates have a dimension of 0.2 × 10.16 × 0.018 mm^3 and periodic distance of 1.508 mm along the *x* axis. There are one layer PCB and one layer substrate in per two YIG slabs, as shown in Figure 1, so the NRIM is a two-dimension periodic structure in the *x* axis and *z* axis. The sizes of YIG slabs, substrates, and wires presented above are specially designed so that the wires dimension is much smaller than the periodic lattice space and the substrates dimension is near the geometric mean of wires dimension and periodic distance. The above parameter values are chosen because it can minimize the interaction of YIG slabs and wire arrays [18].

3. Theories

In this section we briefly show the theoretical analysis of the NRIM presented in Section 2. We mainly focus on the effective permeability and permittivity which describe the macroscopical characters of the composite NRIM. Dewar have analyzed the theoretical results of the effective permeability of the ferrimagnet under applied magnetic field and the effective permittivity of the wire array surrounded with a dielectric material in the ferrimagnetic host [18]. Although the NRIM mode presented here is not the same as mode presented in Ref. [18], the same formula can be used to analyze the mode presented in this paper because the thickness of PCBs is much smaller than YIG's and the effective radius of wire is much smaller than the thickness of PCBs. So assuming a transverse electromagnetic (TEM) wave propagates along the *x*(-*z*) axis with the electric field along the *y* axis and the magnetic field along the *z*(*x*) axis and assuming a applied magnetic field parallel to the wires (the *y* axis), the effective permeability and permittivity of the NRIM presented here can be given by [18]

$$\frac{\mu_{eff}}{\mu_0} = \frac{(H + M_S)^2 - (\omega/\mu_0\gamma)^2}{H(H + M_S) - (\omega/\mu_0\gamma)^2} \tag{1}$$

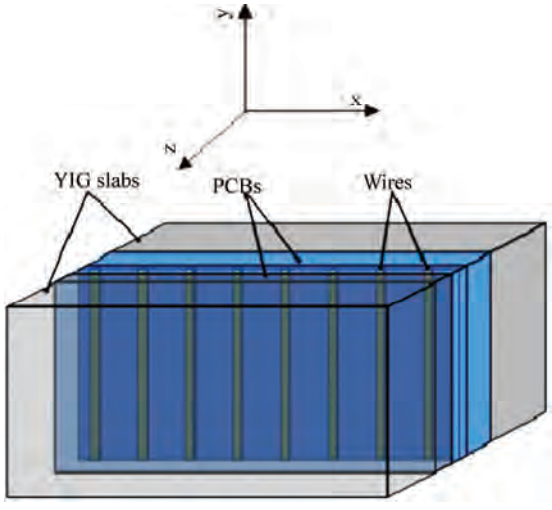

Figure 1. The schematic of NRIM consisting of ferrites and PCBs

$$H = H_0 - i(\omega/\mu_0\gamma)(4\pi\Lambda/\mu_0\gamma M_S) \quad (2)$$

$$\frac{\varepsilon_{eff}}{\varepsilon_0} = \frac{\varepsilon_f}{\varepsilon_0} - \frac{\sigma_{eff}/\omega\varepsilon_0}{i + (\frac{\omega a^2 \sigma_{eff}}{2\pi})(\mu_0 \ln\frac{r_2}{r_1} + \mu_{eff}(\ln\frac{a}{r_2} - 1.6))} \quad (3)$$

Here *Ms* is saturation magnetization of YIG. γ is gyromagnetic ratio. Λ is a phenomenological damping parameter describing loss intrinsic to the magnetic material [18]. H_0 is the applied magnetic field. ε_f is the permittivity of ferrite. σ_{eff} is the effective conductivity of wire arrays. ε_0 is the permeability of air. ω is the angular frequency. r_1 is the radius of the wire. r_2 is the radius of the insulated layer. And a is the periodic lattice constant. Using the equations presented above and parameter values presented in Section 2, the effective permeability and permittivity are calculated and shown in Figure 2.

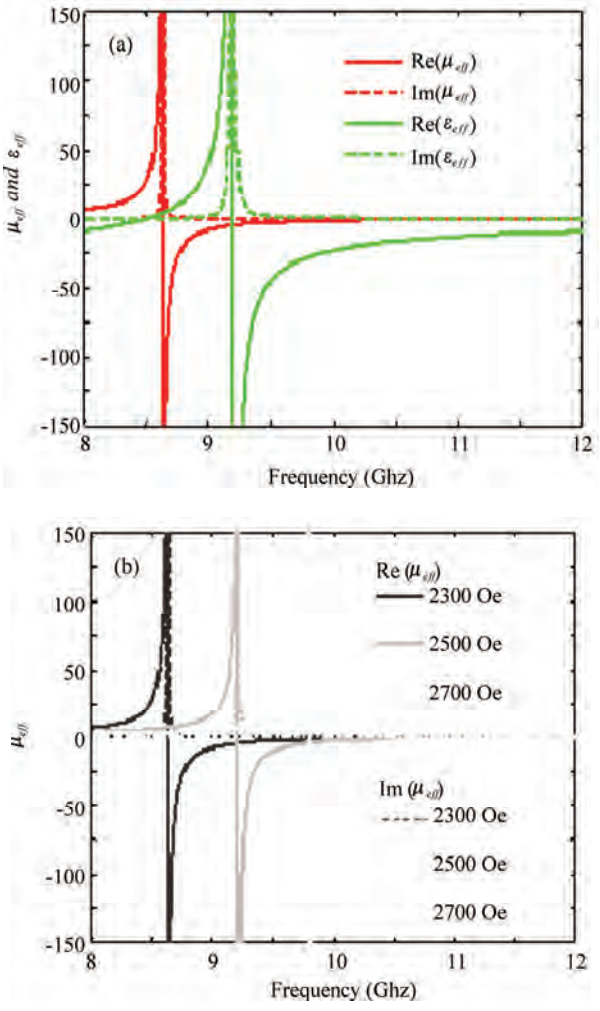

Figure 2. (a) The calculated effective permeability and permittivity by using the Equations (1)-(3). The other parameters are $\Lambda = 10^7$, $H_0 = 2300$ Oe. (b) The calculated effective permeability under different applied magnetic fields

It can be found from Figure 2(a) that both the effective permeability μ_{eff} and permittivity ε_{eff} exhibit typical resonant character. In the broad range from 9.18 GHz to 11.5 GHz both the real part of μ_{eff} and ε_{eff} are negative, so the EM wave can be propagated in such medium. Moreover the bandwidth can be expanded further by choosing different YIG slabs and designing dimensions of the wire array. The image parts of the two parameters, which show the loss in the medium, are much smaller and approximately equal to 0. Moreover, as shown in Figure 2(b), the resonant frequencies of μ_{eff} increase from 8.66 to 9.85 GHz as H_0 rises from 2300 to 2700 Oe. So the NRIM presented in this paper can be tuned by changing the applied magnetic field.

4. Results

In this section, we first investigate numerically the EM properties of the designed NRIM shown in Figure 1 by using ANSOFT's High Frequency Structure Simulator (HFSS) tools, and then measure experimentally the transmission properties and refraction character.

4.1 Simulated Results

To numerically simulate the transmission properties of the NRIM under the incidence of TEM waves, we use a planar waveguide system with a cross section of 22.86 × 10.16 mm^2. The NRIM is put at the middle of planer waveguide with the perfect E boundaries at up and down sides and the Master and Slave boundaries at the left and right sides. Here we simulate two cases.

Case (1): An EM wave propagated along the *z* axis with an electric field along the *y* axis and magnetic field along the *-x* axis, and a dc applied magnetic field along the *y* axis. The parameter values used to simulation are the same as Section 3. The simulated magnitudes of S_{11} and S_{21} of the NRIM under the applied magnetic field of 2300 Oe are shown in Figure 3(a) (black line).

Case (2): The EM wave propagated along the *x* axis with the electric field along the *y* axis and the magnetic field along the *z* axis, and the dc applied magnetic field along the *y* axis. The parameters values are the same as Section 3 too. The simulated magnitudes of the S_{11} and S_{21} of the NRIM under the applied magnetic field of 2300 Oe are shown in Figure 3(a) (light grey line).

At the same time, the magnitudes of the S_{21} of the NRIM in Case (2) under a series of values of the applied magnetic fields are simulated and are shown in Figure 3(b). In Case (1), the propagation direction of the EM wave is perpendicular to the YIG slabs, while in Case (2), the propagation of the EM waves is parallel to the YIG slabs.

In Case (1), as shown in Figure 3(a) (black lines), the NRIM under the applied magnetic field of 2300 Oe exhibits a transmission pass band in which the center frequency is about 10.2 GHz, the peak transmission power

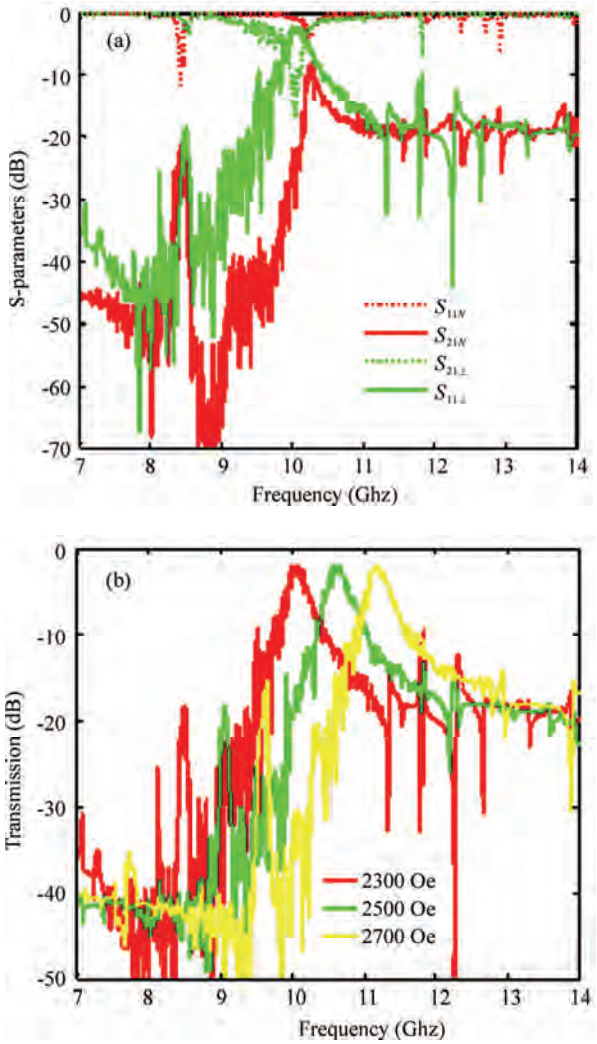

Figure 3. (a) The numerically simulated results of the NRIM in Case (1) (red lines) and Case (2) (green lines). The magnitudes of S_{11} and S_{21} of the NRIM under the applied magnetic field of 2300 Oe are presented. (b) The magnitudes of the S_{21} of the NRIM under a series of values of the applied magnetic field in Case (2)

is about -8 dB, and the bandwidth is about 1 GHz. The green lines in Figure 3(a) show the transmission character corresponding to the Case (2). There is a pass band at 10 GHz with a transmission power of -2.5 dB and a bandwidth of 1 GHz. From the two cases we can know that the NRIM presented in this paper exhibits obviously a pass band with a very low loss and broad frequency band. Moreover, the loss and reflection in Case (2) are smaller than in Case (1). We can also know from Figure 3(a) that there is another transmission pass band at 8.4 GHz. The unexpected pass band can be explained as follows. As shown in Figure 2(a), both the permeability and permittivity are positive at the range of 8.42 GHz – 8.63 GHz. So the composite medium can transfer EM waves too in such range with a positive character. This is due to the interaction between the YIG slabs and wires. Figure 3(b) shows the tunability of the NRIM under different applied magnetic fields in Case (2). The peak of transmission shift from 10 GHz to 11.2 GHz while changing the applied field from 2300 Oe to 2700 Oe.

The simulated results show that the loss of the composite presented here is much smaller than other NRIMs [2,4–9]. The loss of NRIM is generally come from ohmic loss of wires and dielectric loss of substrates. Replacement of the cut-ring structures [2] with ferrites can reduce the loss since ferrites can be less lossy than typical conductors. Choosing bigger wires or superconductors and low-loss substrates can further reduce the loss. The transmission bandwidth of NRIM is determined by the forbidden bandwidth of YIG, namely the ferromagnetic resonance (FMR) and ferromagnetic antiresonance (FMAR) frequencies [18]. It is well known that the FMR frequency and FMAR frequency are given by [18]

$$f_{FMR} = (\frac{\mu_0 \gamma}{2\pi})\sqrt{H(H+M_S)} \quad (4)$$

$$f_{FMAR} = (\frac{\mu_0 \gamma}{2\pi})(H+M_S) \quad (5)$$

So the bandwidth can be expanded and the center frequency can be improved by choosing the YIG slabs of bigger saturation magnetization. From Equations (1)–(3) we can also know that the tunability of the NRIM is dependent on the tunability of negative permeability in the YIG slabs. The wire array has a negative permittivity within a wide frequency region below the plasma frequency [14]. So the region of negative index of the NRIM can be tuned from the low frequency to the plasma frequency of wire array.

4.2 Experimental Results

In order to confirm experimentally the conclusions presented in Section 3 and the numerical results presented above, we fabricated the NRIM sample to measure experimentally the transmission character and also fabricated the prism-shaped prototype to determine the refractive index via the Snell's law.

In practice, the NRIM sample consisting of YIG slabs and PCBs is shown in Figure 4(a). The fabricated sizes are the same as Section 2. We experimentally investigate the transmission character of the NRIM by measuring the scattering parameters. The NRIM sample was put at the middle of X-band waveguide, the waveguide was connected to a vector network analyzer Agilent N5230A (40 MHz–40 GHz). An EM wave propagated along the *x* axis with an electric field along the *z* axis and magnetic field along the *y* axis. An electromagnet was used to generate the external magnetic field along the *z* axis. The transmission coefficient S_{21} of the NRIM sample and the YIG

slabs under the applied magnetic field of 2500 Oe and PCBs were measured using the network analyzer at X-band, were shown in Figure 4(b). To demonstrate the tunability of the NRIM we also have carried out measurements of transmission coefficient in different applied magnetic fields, and the results were shown in Figure 4(c).

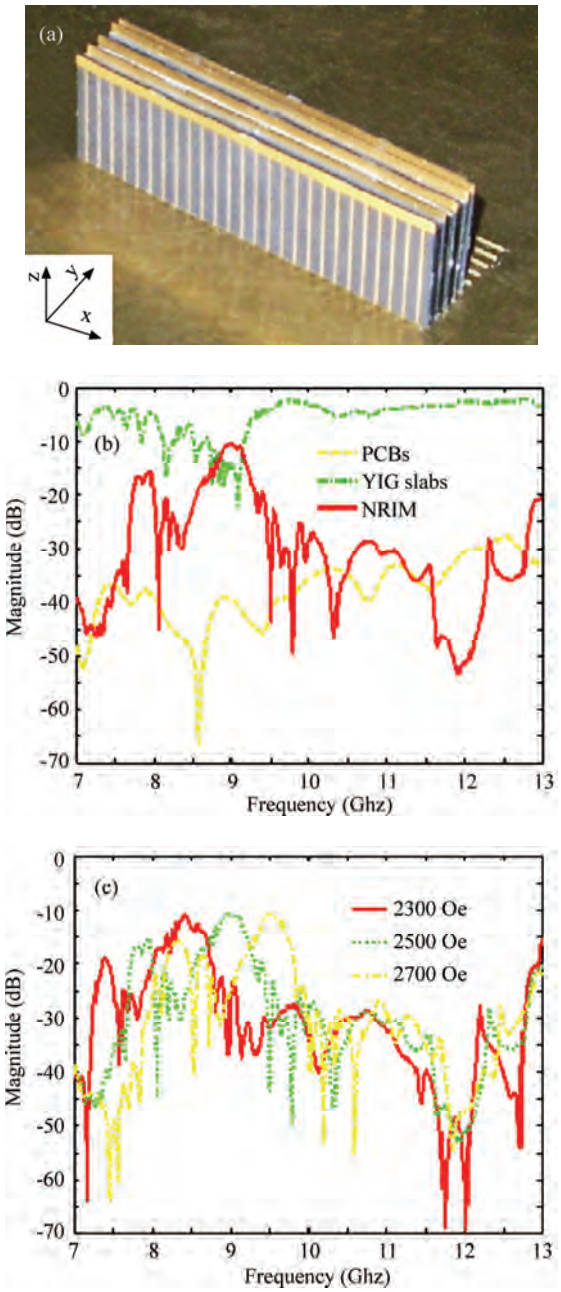

Figure 4. (a) The fabricated NRIM sample. The fabricated sizes are the same as Section 2. (b) The measured transmission results of the NRIM under the applied magnetic field of 2500 Oe in the X-band waveguide. (c) The magnitudes of the S_{21} of the NRIM under a series of values of the applied magnetic field

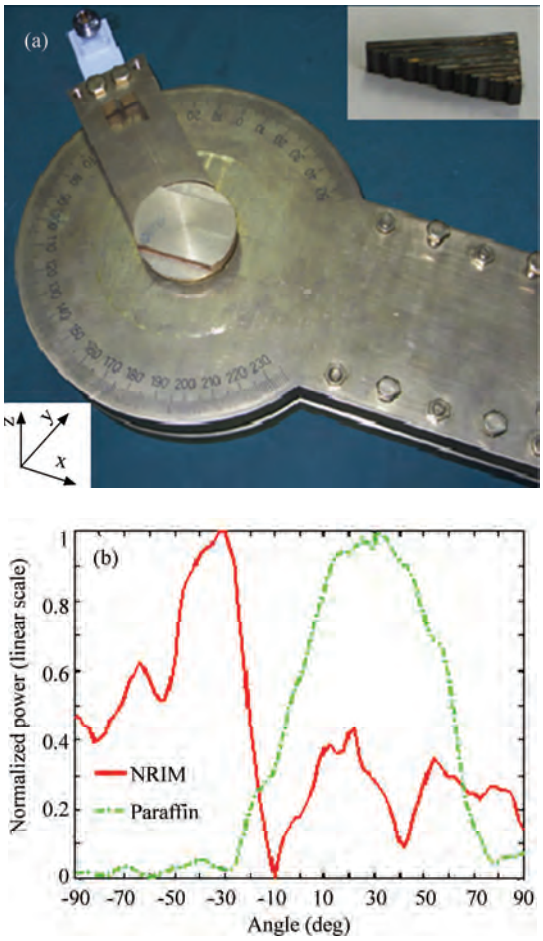

Figure 5. (a) The fabricated prism-shaped NRIM sample and the refraction measured system. (b) The measured refractive angle of the NRIM sample under the applied magnetic field of 2300 Oe and paraffin sample in the same condition

It can be seen from Figure 4(b) that there is a pass band within the forbidden band of both the YIG slabs and PCBs under the field of 2500 Oe. The peak transmission power is about -10.5 dB at 9 GHz and the bandwidth is about 1 GHz. These experimental results are confirming the simulated results indicated in subsection 4.1 very well. But the measured transmission frequency band of NRIM sample is lower than the simulated frequency band. This is because that the experimental measured condition cannot achieve the ideal simulated condition and the applied magnetic field is not completely act on YIG slabs. The measured tunability [Figure 4(c)] of NRIM sample under different fields indicate that, while changing the field from 2300 Oe to 2700 Oe, the magnitude of S_{21} shifted from 8.42 GHz to 9.50 GHz with the sensitively tuning rate of 2.7 MHz/Oe.

For the refraction experiment, we fabricated a prism-shaped NRIM sample inserted in Figure 5(a) and a refraction measured system [3] shown in Figure 5(a). The

sample was placed between the two circular copper plates. The top plate had a pivot in the center, about which an attached X-band microwave waveguide could be rotated to measure transmitted power at arbitrary refraction angles. A beam of incidence microwaves whose electric field was polarized such that it was uniform and parallel to the wires propagated through the sample and encountered the second surface of the prism, the refraction interface, and was refracted into a direction. To measure the exit angle, we rotated the waveguide assembly in 2° steps and recorded the transmitted power spectrum over the entire X-band range at each step, using an Agilent N5230A vector network analyzer. The normal to the NRIM refraction surface was at an angle of 18.43° with respect to the normal of the incident surface. Experiments were performed with a prism-shaped NRIM sample under the field of 2300 Oe as well as with a similarly shaped paraffin sample as a control.

As can be seen in Figure 5(b), at 8.3 GHz, the microwaves were refracted to negative angles of the normal for the NRIM sample. The positive refraction of paraffin sample was shown in Figure 5(b) too. The paraffin data show refraction as would be predicted for $n_{Paraffin} = 1.5 \pm 0.1$, whereas for the NRIM, the measured exit angle of $\theta = -32°$ implies that $n_{NRIM} = -1.6 \pm 0.1$.

5. Conclusions

In conclusion, a low-loss, broadband, and tunable negative refractive index metamaterial consisting of YIG slabs and PCBs is designed and fabricated. Both the simulated and experimental properties of NRIM are investigated. The simulated scattering parameters of the NRIM indicate that there is a pass band in the X-band and the bandwidth is about 1 GHz and the pass band can be shifted by changing the magnetic field. Besides, the experimentally measured scattering parameters show that there is a pass band within the forbidden band of both the YIG slabs and PCBs. The magnitude of S_{21} shifted from 8.42 GHz to 9.50 GHz with the sensitively tuning rate of 2.7 MHz/Oe when changing the applied magnetic field from 2300 Oe to 2700 Oe. Both the simulated results and the experimentally measured results verify the correctness of the designed NRIM. The results open a sample way to fabricate NRIM, further, the metamaterial cloak and absorber.

6. Acknowledgments

This work was supported by the National Science Foundation of China under Grant Nos. 60571024, 60771046, and 60588502.

REFERENCES

[1] V. G. Veselago, "The electrodynamics of substances with simultaneously negative values of permittivity and permeability," Soviet Physics Uspekhi, Vol. 10, pp. 509–514, 1968.

[2] D. R. Smith, W. J. Padilla, and D. C. Vier, "Composite medium with simultaneously negative permeability and permittivity," Physics Review Letters, Vol. 84, pp. 4184–4187, 2000.

[3] R. A. Shelby, D. R. Smith, and S. Schultz, "Experimental verification of a negative index of refraction," Science, Vol. 292, pp. 77–79, 2001.

[4] R. W. Ziolkowski, "Design, fabrication, and testing of double negative metamaterials," IEEE Transaction on Antennas and Propagation, Vol. 57, pp. 1516–1528, 2003.

[5] H. Chen, L. Ran, J. Huangfu, X. Zhang, K. Chen, T. M. Grzegorczyk, and J. A. Kong, "Left-handed materials composed of only S-shaped resonators," Physics Review E, Vol. 70, 057605-1-4, 2004.

[6] G. V. Eleftheriades, A. K. Iyer, and P. C. Kremer, "Planar negative refractive index media using periodically L-C loaded transmission lines," IEEE Transaction on Microwave Theory and Techniques, Vol. 50, pp. 2702–2712, 2002.

[7] L. Liu, C. Caloz, C. Chang, and T. Itoh, "Forward coupling phenomena between artificial left-handed transmission lines," Journal of Applied Physics, Vol. 92, pp. 5560–5565, 2002.

[8] M. Notomi, "Theory of light propagation in strongly modulated photonic crystals: Refractionlike behavior in the vicinity of the photonic band gap," Physical Review B, Vol. 62, pp. 10696–10705, 2000.

[9] P. V. Parimi, W. T. Lu, J. S. Derov, J. Sokoloff, J. S. Derov, and S. Sridhar, "Negative refraction and left-handed electromagnetism in microwave photonic crystals," Physics Review Letters, Vol. 92, 127401-1-4, 2004.

[10] S. Lim, C. Caloz, and T. Ttoh, "Electronically scanned composite right/left handed microstrip leaky-wave antenna," IEEE Microwave Wireless Components Letters, Vol. 14, pp. 277–279, 2004.

[11] H. Tao, N. I. Landy, C. M. Bingham, X. Zhang, R. D. Averitt, and W. J. Padilla, "A metamateial absorber for the terahertz regime: Design, fabrication and characterization," Optics Express, Vol. 16, pp. 7181–7188, 2008.

[12] D. Qiang and G. Chen, "Enhancement of evanescent waves in waveguides using metamaterials of negative permittivity and permeability," Applied Physics Letters, Vol. 84, pp. 669–671, 2004.

[13] K. Aydin and E. Ozbay, "Left-handed metamaterial based superlens for subwavelength imaging of electromagnetic waves," Applied Physics A, Vol. 87, pp. 137–141, 2007.

[14] J. B. Pendry, A. J. Holden, W. J. Stewart, and I. Youngs, "Extremely low frequency plasmons in metallic mesostructures," Physics Review Letters, Vol. 76, pp. 4773–4776, 1996.

[15] J. B. Pendry, A. J. Holden, D. J. Robbins, and W. J. Stewart, "Magnetism from conductors and enhanced nonlinear phenomena," IEEE Transaction on Microwave Theory and Techniques, Vol. 47, pp. 2075–2084, 1999.

[16] D. Schurig, J. J. Mock, B. J. Justice, S. A. Cummer, J. B. Pendry, A. F. Starr, and D. R. Smith, "Metamaterial electromagnetic cloak at microwave frequencies," Science, Vol. 314, pp. 977–980, 2006.

[17] H. Chen, Z. Liang, P. Yao, X. Jiang, H. Ma, and C. Chan, "Extending the bandwidth of electromagnetic cloaks," Physics Review B, Vol. 76, 201104-1-4, 2007.

[18] G. Dewar, "The applicability of ferromagnetic hosts to nanostructures negative index of refractive (left-handed) materials," Proceedings SPIE, Vol. 4806, pp. 156–166, 2002.

[19] Y. J. Cao, G. J. Wen, K. M. Wu, and X. H. Xu, "A novel approach to design microwave medium of negative refractive index and simulation verification," Chinese Science Bulletin, Vol. 52, pp. 433–439, 2007.

[20] X. B. Cai, X. M. Zhou, and G. K. Hu, "Numerical Study on Left-Handed Materials Made of Ferrite and Metallic Wires," Chinese Physics Letters, Vol. 23, pp. 348–351, 2006.

[21] H. J. Zhao, J. Zhou, Q. Zhao, B. Li, L. Kang, and Y. Bai, "Magnetotunable left-handed material consisting of yttrium iron garnet slab and metallic wires," Applied. Physics Letters, Vol. 91, 131107-1-3, 2007.

[22] Y. X. He, P. He, S. D. Yoon, P. V. Parimi, F. J. Rachford, V. G. Harris, and C. Vittoria, "Tunable negative index metamaterial using yttrium iron garnet," Journal of Magnetism and Magnetic Materials, Vol. 313, pp. 187–191, 2007.

J. Electromagnetic Analysis & Applications, 2010, 2: 111-115
doi:10.4236/jemaa.2010.22016 Published Online February 2010 (www.SciRP.org/journal/jemaa)

Research on the Effect of High Power Microwave on Low Noise Amplifier and Limiter Based on the Injection Method

Dong Chen [1], Liming Xu [1], Bisheng Zhang [1], Hongge Ma [2]

[1]Naval Academy of Armament, Beijing, China; [2]Institute of Applied Electronics, CAEP, Mianyang, China.
Email: lieutengin_cd@yahoo.com.cn

Received September 21st, 2009; revised November 3rd, 2009; accepted November 9th, 2009.

ABSTRACT

The reliability of electronic device is threatened in high power microwave (*HPM*) *environment. In accordance with the situation that the emulation is ineffective in evaluating the accuracy and precision of the HPM effect to electronic device, the experimental method is used to resolve the problem. Low Noise Amplifier* (*LNA*) *and Limiter are selected as the objects for the experiments, the structural characteristic of the front-end of radar receiver is described, the phenomena and criterion are elaborated and analyzed using injection method due to its ability to get an accurate threshold avoiding the complex coupling, the basic principle of injection experiment is demonstrated, and the method and process of effect experiment about Low Noise Amplifier and Limiter are also explained. The experimental system is established, and the system is composed of low power microwave source such as TWT, test equipment for obtaining the effect parameters, and some of auxiliary equipments as camera, optical microscope or electron microscopy, attenuator, detector, and directional coupler etc. The microwave delivered from source is adjusted to the power infused by attenuator, and pour in the decanting point of effecter via directional coupler, then the couple signal created by directional coupler is input to the recording instrument after detecting by detector, finally the power of effecter is obtained. The value of power, which damages the effecter in the microwave pulse environment, is classified at the index of sensitivity, and the threshold is obtained by power diagnose and wave test. Some regular understandings of the HPM effect to electronic device are obtained based on the results of the experiments. It turns out that the index of electronic device is influenced significantly by the energy via front door coupling, the MOSFET made up of GaAs is the most wearing part to HPM in LNA, the damage threshold of LNA is about 40dBm under single pulse while in repetitive pulse the value is from 33.3dBm to 43.9dBm according to different wave band. The damage threshold of Limiter is about 56dBm to80dBm.*

***Keywords*:** *High Power Microwave, Low Noise Amplifier, Front Door Coupling, Injection Experiment*

1. Introduction

Nowadays electronic equipments are facing the proliferating threats from HMP, thus require the equipments which have outstanding performance and complex structure should have much higher reliability. The high gain aerial is widespread used in modern radar and satellite communication system, in this case the electromagnetic energy coupled in front-door is much higher than coupled in back-door, so the front-end of radar receiver and satellite communication system is the most vulnerable part under the threat of HPM.

The limitation of emulation in analyzing and evaluating the HPM effect to electronic device caused by the complex structure of electronic equipment and incomplete description of damage mechanism of HMP lead to weakness on analysis [1,2]. The effect experiment is in a sense the most intuitive and efficient method to analyze the effect of electromagnetic on electronics, the threshold of sensitive components is determined by microwave effect experiment, and the result is the necessary data for analyzing the electromagnetic performance of system and hardening electromagnetic pulse. It is very important to carry out the experimental study of effect of electromagnetic on electronic devices and components for hardening the electronic system especially for military use.

2. Methodology

2.1 The Principle of Injection Experiment

The injection method is the popular means to solve the problem about the electromagnetic effect on components

and element circuit. The effect quantification of components is obtained by using this method. The microwave shall act on the effecter through the front door, and then an accurate threshold is gotten due to neglecting the complex coupling, thus applied in analyzing mechanism, principle and predicting the effect of front door coupling. The simulation research on effect mechanism is contribute to understand the whole system effect, but it's not the efficient way to acquire the threshold for judging the entire system use, therefore, by applying the injection experiment method, the results about the effect on the certain waveform in each interface under certain conditions will be analyzed.

The fundamental condition of injection method is low power microwave source with adjustable parameters such as TWT, parameter test equipment, some of auxiliary equipments as camera, optical microscope or electron microscopy etc. Figure 1 shows the functional block diagram of injection experiment [3].

The power microwave source and output terminal of signal should be separated and shielded in order to avoid the influence from reflected signal, and special attention should be paid while coaxial line transfers to the microwave in order not to cause the distortion of radiation and waveform, and the separation point also requires separation protection. The test system is composed of several parts given below: power microwave source, the control parts of the source, regulation parts of the power, transmission and diagnosis parts of power, test equipment and recording instrument.

2.2 Design of Injection Experiment about LNA

The functional block diagram of injection experiment about LNA is shown in Figure 2. The attenuator and detector are both measured, The microwave delivered from source is adjusted to the power infused by attenuator, and

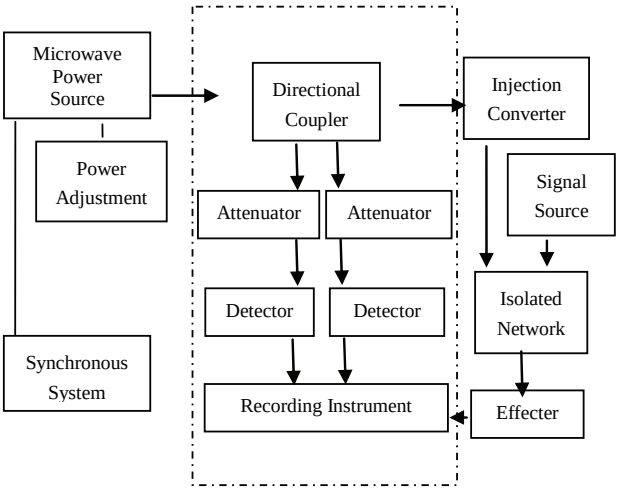

Figure 1. the functional block diagram of injection experiment

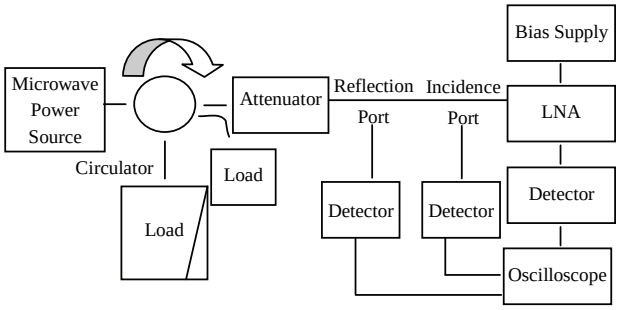

Figure 2. The functional block diagram of injection experiment about LNA

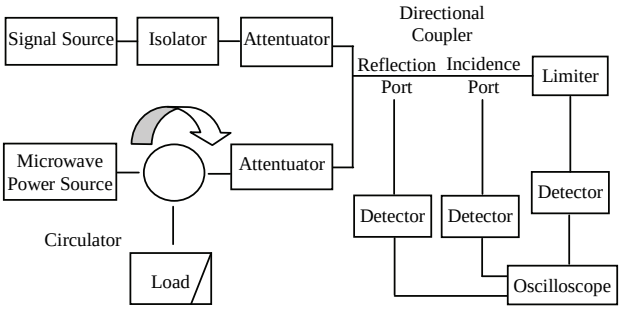

Figure 3. The functional block diagram of injection experiment about Limiter

pour in the decanting point of effecter via directional coupler, then the couple signal created by directional coupler is input to the recording instrument after detecting by detector, finally the power of effecter is obtained. The value of power, which damages the effecter in the microwave pulse environment, is classified at the index of sensitivity, and the threshold is obtained by power diagnose and wave test [4].

2.3 Design of Injection Experiment about Limiter

The leakage of rising edge will be revealed under the action of HPM, in other words HPM can transit the Limiter, the power leakage may lead the next level of circuit to interference and damage, meanwhile HPM may also cause the functional decline of Limiter under certain circumstance, the functional block diagram of injection experiment about Limiter is shown in Figure 3.

3. Analysis

3.1 Analysis of the Structural Characteristic of the Front-End of Radar Receiver

The front-end of radar and satellite communication system fulfill the function of signal amplification and mixing, the damage of receiver caused by the microwave through the front door is in fact the failure of components of

front-end of radar. Figure 4 shows the composition and structure of the front-end of radar, it consists of RF, receiver protector, LNA, mixer and LO [5].

3.2 Analysis of the Effect of LNA in Injection Experiment

The LNA is the vulnerable component of front-end of radar, designed by multiple cascaded straight amplification style, the noise caused by the first level of amplifier has the greatest and the most serious damage to LNA, the gain of whole amplifier is reduced while the noise temperature is increased once the LNA is damaged, thus bring about the SNR of the system a reduction, and finally makes radar system doesn't work [3,4].

Figure 5 and Figure 6 shows the gain of LNA before and after injection experiment, the value of gain is provided by network analyzer.

The output signal can not meet the requirement of next level of circuit while the gain of LNA decline 3dB, generally speaking, the value 3dB is regarded of the standard for judging whether LNA is normal or abnormal, the

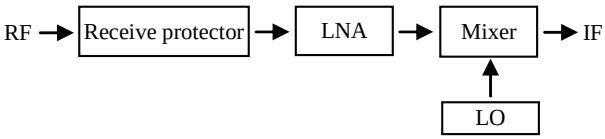

Figure 4. Front end of radar receiver

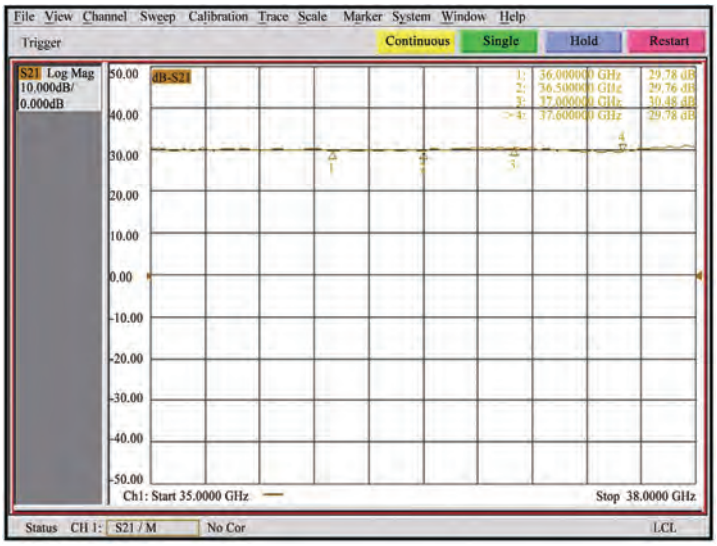

Figure 5. The gain of LNA before experiment

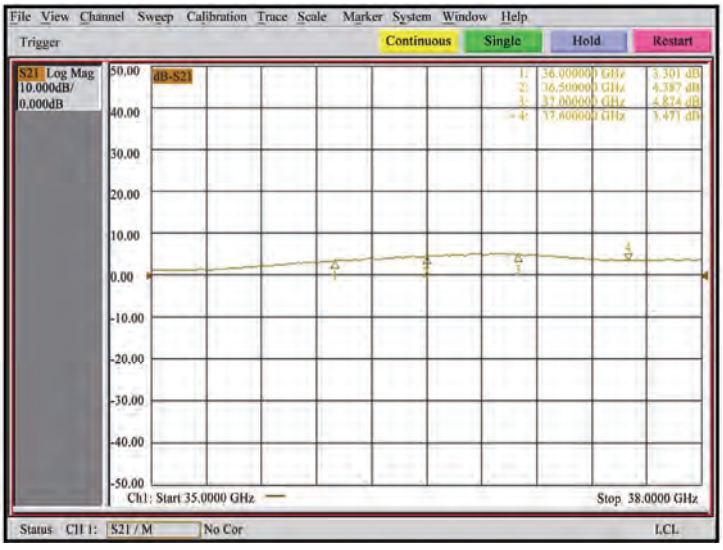

Figure 6. The gain of LNA after experiment

gain declination in injection experiment is more than 3dB after HPM is poured in, it is reputed that HPM can damage LNA efficiently.

3.3 Analysis of the Effect of Limiter in Injection Experiment

The basic function of Limiter is to control the signal under secure level all the time, to avoid the damage of LGA and Mixer receiving distortion of electronic equipments induced by high power signal.

The criterion for judging whether Limiter is normal or abnormal is one more than it of LNA, the first one is short circuit due to breakdown while insertion loss increased, of which 3dB is considered to be as symbol that the limiter is damaged, while an other one is the output level rises as input level rises when the value of insertion loss is constant, clipping is malfunction, the output level is twice higher than HPM is not poured in, in this case open circuit occurred in Limiter due to burn down.

Figure 7 and Figure 8 shows the change of insertion loss among injection experiment, the value of insertion loss is measured by network analyzer.

The insertion loss is higher about 10dB while HPM is poured in, it is more than the criterion (3dB), meanwhile the output level rises as input level rises, and it is obvious that HPM damaged Limiter.

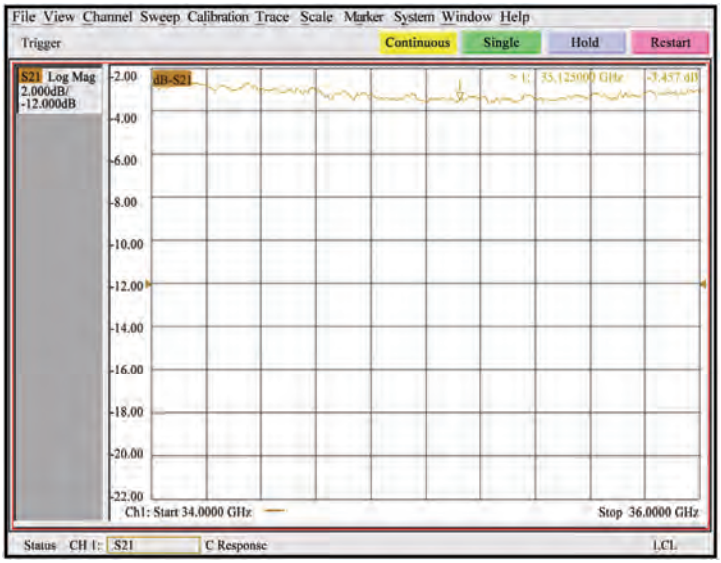

Figure 7. The insertion loss of Limiter before experiment

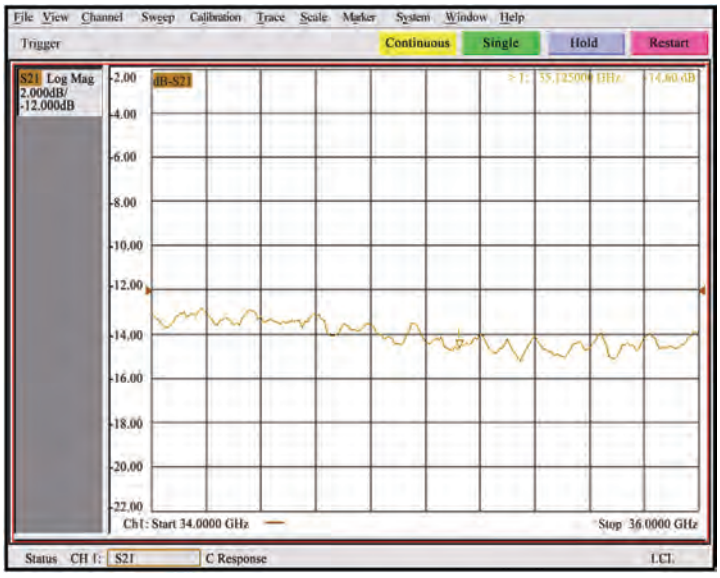

Figure 8. The insertion loss of Limiter after experiment

4. Result

The micrograph describes the damage of LNA in injection experiment is shown in Figure 9.

The result turns out that the damage of LNA is caused by damage of GaAs FET, the microwave signal should pour in the point between grid and source of GaAs FET, electric field breakdown disrupts the deletion layer and creates instantaneous current [6], on the other hand, the HPM destroy the depletion layer and grid directly, the principle of damage of LNA caused by HPM based on the results of experiment is presented below [3,4]:

1) Damage threshold of LNA for different band

- The LNA may be damaged while power infused is about 33.3dBm to 48.6dBm (that is 2.14W to 72.44W), the effect is arisen from the damage of GaAs FET.
- The damage threshold of LNA at X band is divided into two parts: in the case of single microwave pulse the threshold is about 39.5dBm to 48.6dBm (that is 8.91W to 72.44W), while in the case of repetitive frequency microwave pulse the threshold is about 39dBm to 43.9dBm (that is 7.94W to 24.55W).

2) Difference of damage threshold vs band style

- The difference of the damage threshold of LNA among different band is 1.6 dB to 3.5dB.
- Differences of threshold may also exist at the same band. The experiment results shown that difference of LNA at the same band is 2.2dB to 9.6dB.

3) Difference of damage threshold vs pulse width

- Differences of threshold may also exist in different pulse width, it is 2.2dB to3.7dB.

At the same single microwave pulse, the difference of the damage threshold of LNA between single pulse and repetitive pulse (<=100hz) is 3.7~6.5dB; the damage threshold of LNA is 39.5dBm~48.6dBm（8.91W~72.44W）for single pulse and 33.3dBm~43.9dBm (2.14W~24.55W) in repetitive pulse.

4) Difference of damage threshold vs brand of GaAs FET

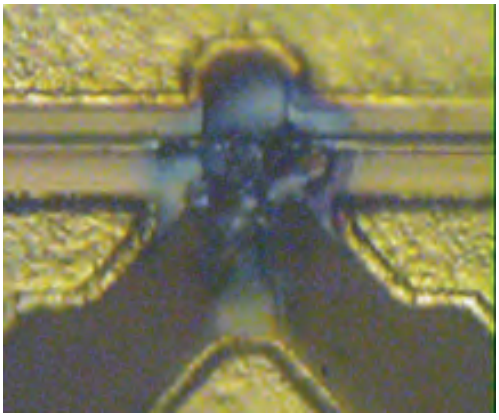

Figure 9. Micrograph of LNA damaged

- The damage threshold of low noise amplifier will be different when using GaAs FET of different brands.
- With different models of the same brand of GaAs FET, the difference of the damage threshold would be 0.3dBm~3.1dBm.

Three types of Limiter are selected to analyze the HPM effect, the principle of damage of Limiter caused by HPM based on the results of experiment is presented below:

- Whether to breakdown or burn down the Limiter at single narrowband microwave pulse high power should be required.
- The insertion loss increased rapidly while standing-wave changed very little.
- The interference effect will be different when the time for the meeting of injected signal and working signal is different, which is caused by the difference of sensitivity of working signals when they work on different positions.
- The damage threshold of Limiter will be different even produced by the same manufacturer, and it varies greatly when using Limiter of different brands.

5. Conclusions

The effects of HPM on electronic equipments should not be ignored, the results based on injection experiment turns out that LNA may be damaged mainly caused by the failure of GaAs FET; the damage threshold of LNA at C band is lower than it at X band, and it is much lower than Limiter.

REFERENCES

[1] M. G. Bäckström and K. G. Lövstrand, "Susceptibility of electronic systems to High-Power Microwaves: summary of test experience," IEEE Transactions on Electromagnetic Compatibility, Vol. 46, No. 3, pp. 396–403, August 2004.

[2] F. Sabath, M. Bäckström, B. Nordström, D. Sérafin, A. Kaiser, B. A. Kerr, and D. Nitsch, "Overview of four European high-power microwave narrow-band test facilities," IEEE Transactions on Electromagnetic Compatibility, Vol. 46, No. 3, pp. 329–334, August 2004.

[3] Y. wang, H. G. Ma, and X. J. Cao, *et al.*, "Proceedings of Annual Report of China Academy of Engineering Physics," Annual Report of China Academy of Engineering Physics, 2003.

[4] Y. Wang and H. G. Ma, et al, "Annual Report of China Academy of Engineering Physics," Annual Report of China Academy of Engineering Physics, 2005.

[5] M. Skolnik, "Introduction to Radar Systems," Third Edition. McGrawHill : New York, 2001.

[6] D. Nitsch, M. Camp, F. Sabath, J. L. Haseborg, and H. Garbe, "Susceptibility of some electronic equipment to HPEM threats," IEEE Transactions on Electromagnetic Compatibility, Vol. 46, No. 3, pp. 380–389, August 2004.

J. Electromagnetic Analysis & Applications, **2010, 2: 116-119**
doi:10.4236/jemaa.2010.22017 Published Online February 2010 (www.SciRP.org/journal/jemaa)

Scientific Research

3D Diffractive Focusing THz of In-Plane Surface Plasmon Polarition Waves

Igor Minin, Oleg Minin

Novosibirsk State Technical University, Russia.
Email: igor.minin@ngs.ru, prof.minin@gmail.com

Received September 11th, 2009; revised October 22nd, 2009; accepted October 28th, 2009.

ABSTRACT

Demonstrated that analog of diffractive and refractive 3*D optics in free space can be developed to manipulate surface waves such as surface plasmon polaritons* (*SPPs*). *It has been shown that an air-gap control of a floating dielectric block can generate the dynamic phase and amplitude modulation of the SPP transmission coefficient. Unlike conventional bulk optics, the nano-scale surface optics for SPP processing contains several unexpected and interesting features in addition to the physical features described. Dynamic plasmonic information processing on the nano-scale using air-gap control may be an effective mechanism for building a dynamic plasmonic information processing system.*

***Keywords*:** *Diffractive Optical Element, Surface Plasmon Polarition Waves, Three Dimension*

1. Introduction

THz and optical information processing on the nano-scale is considered to be a main objective in the field of nanophotonics. Recently, THz and optical information processing on the nano-scale has become a reality because of the exploitation of the full potential of surface plasmon polaritons (SPPs) [1–3]. SPPs are electromagnetic surface waves formed through strong interaction between electromagnetic field and free electron oscillations at a metal-dielectric interface. It is strongly desired to excite and control propagating SPP fields in a systematic fashion as is possible with optical fields both in free space and dielectric waveguides. One of unique properties of the SPPs is that SPPs wavelength can be shorter than the wavelength of radiation in surrounding media, leading to applications in sub-diffraction-limited techniques.

Discovering this effect birthed many new research areas in SPP/subwavelength optics or other spectral band fields. To realize the promise of SPP technologies, a comprehensive arsenal of optical elements for launching, detecting, guiding, imaging, focusing, and otherwise transforming SPP waves must be readily available. Once the basic optical manipulation of SPP has become routine, it will pave the way for more sophisticated devices, including different wavebands, possibly including confocal microscopes with sub-diffraction limited resolution obtained by focusing of SPP fields [4].

Surface electromagnetic effects could enhance the efficiency of numerous physical and chemical processes [7], as these effects lead to an increase of the electromagnetic fields at the surface, giving rise to an improved experimental sensitivity. In particular, the excitation of surface plasmons (SP) [8] at the metal surface may increase by three orders of magnitude the intensity of optical beams generated at the surface, like Raman or second harmonic signals [9].

A SP corresponds to the quantum of energy associated to a harmonic oscillation of the free charges at the metal surface (the SP wave), which is mostly perpendicular to the surface and which propagates along the surface. Solving Maxwell equations (homogeneous problem) for this interface leads to the SP dispersion relation:

$$K_{sp} = \frac{\omega}{c}\sqrt{\frac{\varepsilon}{\varepsilon+1}},$$

where ε is the dielectric constant of the metal, K_{sp}—wave number of SP, $\omega=2\pi/\lambda$, λ is a wavelength in free space. So we solved the material problem, but to match the moments, we can choose one of three main techniques. The first technique uses a prism and total internal reflection; the second one involves scattering from a topological defect like small holes in a thin film. The third technique makes use of periodic corrugations in the metal's surface.

In the far infrared, this dielectric constant takes large values, thus:

$$K_{sp} \approx \frac{\omega}{c}\left(1-\frac{1}{2\varepsilon}\right),$$

The energy coupled to the SP is diffracted by the grating while SP propagates along the grating surface.

2. Diffractive Focusing Element Design

Several parabolic lens structures for SPPs have been demonstrated [10,11]. Recently, a double slit experiment of SPPs [12] was reported to show that the low- dimensional diffraction theory analogue to Fresnel diffraction theory is applicable to SPPs.

We propose a novel SPP focusing approach using an in-plane SPP 3D conical Fresnel zone plate [5] (FZP) in which the designed rules are strictly following traditional Fourier Optics. The possibilities of SPP focusing using in-plane traditional FZP was demonstrated in [6].

Figure 1 represents an adaptation of a free-space quasi-optical component known as the 3D Fresnel zone plate (conical FZP) for focusing SPP waves.

A conventional free-space flat conical FZP comprises quasi-concentric structure. From the geometric consideration for the FZP on a cone surface the boundaries (a,y) of n-th zone is determined from the quadratic equation [5]:

$$a^2 tg^2\alpha - 2a(htg^2\alpha - n\lambda/2) + h^2 tg^2\alpha - n\lambda F - (n\lambda/2)^2 = 0 \quad (1)$$

$$y = (h-a)tg\alpha\,, \quad (2)$$

where (a,y) is function of the n, h – the height of the cone. $h = D/(2tg\alpha)$, D – is the diameter of the FZP. The design of flat cone FZP is based on a phase modulation of the surface plasmon provided by dielectric block deposited on the interface. The modulation can be realized by changing height or width of the dielectric block. We compare the focusing properties of the flat FZP, and the cone FZPs with different $h=(F/3, F/2, F-10\lambda)$. The diameter of the FZP lenses is 30 mm with a focal length of F=2.5 cm at 1 THz.

Planar diffractive elements have a number of specific features [5,13–14], the main of them being: one-dimensional nature of the element and the need to take into account the properties of the substrate on which the element is placed. From the mathematics standpoint, the first of these factors is easy to take into account: for this, integration over angle in calculating the diffraction integral is replaced with a sum of two values of the integral for $\varphi = 0$ and $\varphi = \pi$ (in the symmetric case). In other words, it is not necessary to compute the double integral but the sum of two single integrals.

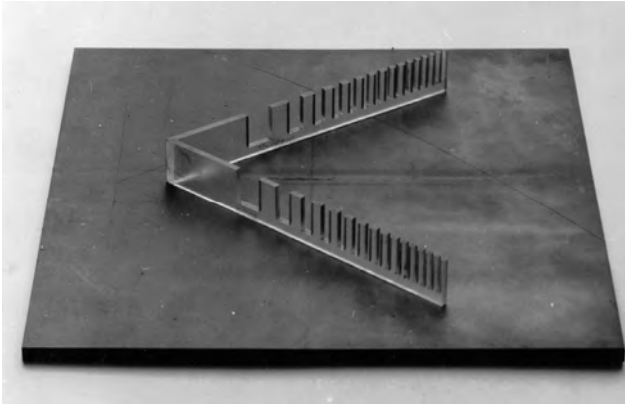

Figure 1. Diffractive planar element on a conical surface

Thus, for the planar analogue of the zone plate it will be sufficient to calculate the sum of two single integrals of the following type [5]:

$$U(p_2) = \sum_{i=1}^{2} \int \frac{\exp(ik(r_i + S_i))}{r_i S_i} \left(\frac{z_2}{S_i} - \frac{z_1}{r_i} \right) RdR\,,$$

where $p_2 = (x_2,0,z_2)$ are the coordinates of the observation point; $p_1 = (x_1,0,z_1)$ are the coordinates of the radiation source;

$$A = -z_1; \quad B = z_2; \quad r^2{}_1 = (z_1 - z)^2 + (x_1 - R)^2;$$
$$S^2{}_1 = (z_2 - z_1)^2 + (x_2 - R)^2$$

and

$$r^2{}_2 = (z_1 - z)^2 + (x_1 + R)^2;$$
$$S_2{}^2 = (z_2 - z)^2 + (x_2 + R)^2.$$

The frequency and focusing properties of diffractive elements fabricated on a curvilinear surface are determined, among other things, by the degree of convexity (concavity) of the surface. We can expect, therefore, that placing of planar elements of integral optics on non-flat curves will provide the possibility of controlling both the frequency and the focusing properties. As an example, consider the main properties of a "conical" diffractive element (Figure 1) [5]. The initial data for such "planar conical" diffractive element were: $D/\lambda \sim 35$, $D/A \sim 0.4$, $D/B \sim 0.8$; the number of phase quantization levels was two; the element of phase inversion type was chosen. Its pro-perties were investigated numerically and experimentally in the 4 mm wavelength band.

3. Experimental and Simulation Results

The method of computing simulation is described in detail in the book [5]. The detailed description of experimental set-up and the technique of researches are also described in [5].

Figure 2 shows the distribution of field intensity in the focal region of a diffractive element transversally to its optical axis; it was obtained experimentally and by numerical computation of the diffraction integral. The transition from three-dimensional element to two-dimensional structures increases the level of side lobes. Further investigation of the properties of such elements showed that the frequency and focusing properties are maintained in a wide spectral interval, just as they are for three-dim-

ensional diffractive elements. As it follow from the Figure 2, the proposed focusing element allow to focus SPP with limiting space resolution according Airy criterion [5].

Therefore, the investigation of the planar two-dimensional diffractive element fabricated on a conical surface and a comparison of the results obtained with the characteristics of similar three-dimensional diffractive elements (Figure 3) allow us to draw a conclusion that such planar elements possess adequate frequency characteristics, sustain focusing ability in a wide spectral range on wavelengths that differ from the nominal wavelength, and are diffraction-constrained systems. It could be noted that the focal length of the conical FZP is less influenced by changes in air-gap, *i.e.*, a change in the effective refractive index, since the focal length is mainly determine- ed by the spatial diffractive profile, which is fixed. The confined field distribution is characterized in detail by the method of Finite-Difference Time-Domain (FDTD). Calculations were performed by the software package, XFDTD 6.2, from REMCOM.

Also we have shown that an air-gap control of a floating dielectric block can generate the dynamic phase and amplitude modulation of the SPP transmission coefficient. As an application of this property, we have demonstrated the variable-focusing properties of an SPP floating dielectric parabolic lens using numerical simulations and compared the focusing properties of SPP parabolic lenses and SPP Fresnel lenses. Unlike conventional bulk optics,

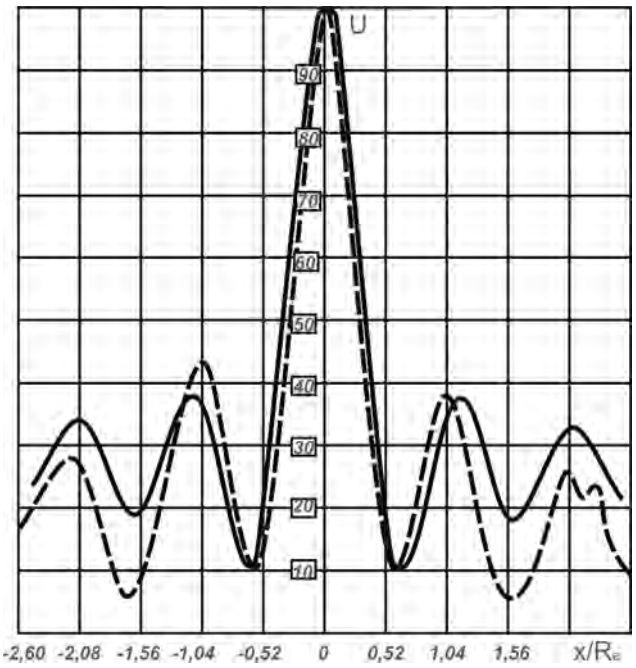

Figure 2. Field intensity distribution transversally to the optical axis of a planar diffractive element:
_____theory; _ _ _ _ _ experiment

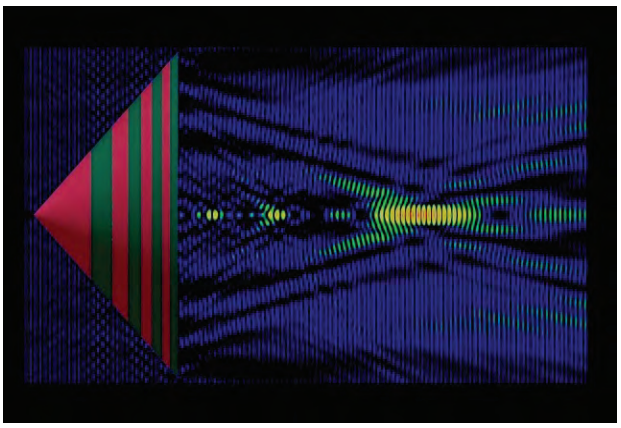

Figure 3. The field intensity distribution along the optical axis of 3D conical FZP calculated by FDTD method

the nano-scale surface optics for SPP processing contains several unexpected and interesting features in addition to the physical features described in this paper. Dynamic plasmonic information processing on the nano-scale using air-gap control may be an effective mechanism for building a dynamic plasmonic information processing system.

4. Conclusions and Discussion

The successful adaptation of free-space 3D conical Fresnel Zone Plate for operation on SPP waves demonstrates that analogues of Fourier diffractive components can be developed for SPP 3D optics. As in free-space, the basic SPP optical components are the necessary enablers for more sophisticated future devices.

So we have demonstrated that analogs of diffractive and refractive 3D optics in free space can be developed to manipulate surface waves such as SPPs and focusing electromagnetic waves with diffraction limit.

The possibility of manipulating SPP-like light beams, but in 2D and 3D, will provide many new possibilities. For example, the implementation of optical digital computers mostly depends on the creation of optical logic elements (optical analogues of electronic gates) that carry out various logical operations (AND, OR etc) that would go beyond the speed of microelectronic devices and their degree of integration, also reducing cost and power consumption [5,13,14]. Diffractive (dispersive) elements can be used for spectrally selective addressing of signals, can be applied in polychromatic optical processors, serve as a basis for polychromatic logic elements or multiplexer or a focusing element with selectivity in the multimode regime etc. [5]. It has been shown by detailed simulation results obtained using a parallel FDTD method that novels diffractive element in the THz waveband offers the potential to realize novel types of devices for communications, sensing, integrated optics,

networks, transmission lines, and so on [15–18]. To this end, diffractive planar elements fabricated on non-flat surfaces make it possible to enrich the "pool of devices" for applications including integrated optics at different waveband, including THz, and to design elements with novel properties and potentials.

Another application of new SPP 3D FZP is to focusing surface plasmon polariton trapping of colloidal particles. The in-plane 3D FZP focus area releases a significant amount of energy to the liquid, particularly in the center region where an enhancement of the near-field intensity is observed. Thus, the localized convection streams, which result from this off-equilibrium process, are enhanced when the SPP resonates. The resulting contrast leads to an in-plane electromagnetic intensity gradient, which can be engineered to form a stable potential well able to trap particles located in its vicinity.

REFERENCES

[1] X. Wu, D. Li, W. H. Sun, F. Gao, Z. J. Zhang, and R. W. Peng, "Coupling of terahertz surface plasmon polaritons in corrugated stacks of dielectric and semiconductor," PIERS Online, Vol. 5, No. 2, pp. 101–104, 2009.

[2] M. Rajarajan, C. Themistos, B. M. A. Rahman, and K. T V Grattan, "Plasmonics in metal-clad terahertz waveguides," PIERS Online, Vol. 3, No. 3, pp. 294–299, 2007.

[3] J. G. Han, X. C. Lu, A. K. Azad, M. F. Gong, and W. L. Zhang, "The role of non-resonant effect in terahertz transmission through subwavelength holes," PIERS Online, Vol. 4, No. 4, pp. 481–484, 2008.

[4] S. C. Chen, T. M. Chang, and D. P. Tsai, "Focusing the enhanced near-field by manipulating the nano-plasmon-driving intensifiers," PIERS Online, Vol. 1, No. 4, pp. 445–447, 2005.

[5] I. V. Minin and O.V. Minin, "Diffractional quasioptics," Moskow: InformTei, pp. 180 (in Russian), 1992. See also: O. V. Minin and I. V. Minin, "Diffraction optics of millimeter waves," London: IOP Publisher, pp. 396, 2004.

[6] L. Feng., K. Tetz, B. Slutsky, V. Lomakin, and Y. Fainman, "Fourier plasmonics: Diffractive focusing of in-plane surface plasmon polarition waves," Applied Physics Letters, 91, 081101, 2007.

[7] Schatz G. C. and R. P. van Duyne (Eds.), "Electromagnetic mechanism of surface-enhanced spectroscopy," Wiley, New York, 2002.

[8] R. F. Wallis and G. I. Stegeman (Eds.), "Electromagnetic surface excitations," Springer Series on Wave Phenomena, Springer, Berlin, 1988.

[9] D. B .Ostrowsky and R. Reinisch (Eds.), "Guided wave nonlinear Optics," Kluwer Academic Publishers, Dordrecht, 1992.

[10] I. P. Radko, S. I. Bozhevolnyi, A. B. Evlyukhin, and A. Boltasseva, "Surface plasmon polariton beam focusing with parabolic nanoparticle chains," Opt. Express 15, 6576–6582, 2007.

[11] W. Nomura, M. Ohtsu, and Yatsui T, "Nanodot coupler with a surface plasmon polariton condenser for optical far/bear-field conversion," Applied Physics Letters, 86, 181108, 2005.

[12] R. Zia and M. L. Brongersma, "Surface plasmon polariton analogue to Young's double-slit experiment," Nature Nanotech, 2, pp. 426–429, 2007.

[13] I. V. Minin, O. V. Minin, C. Chen, J. Mititu, and D. W. Prather, "Novel type of the elements of integrated diffractive optics," Terahertz for Military and Security Applications IV, Novel Terahertz Devices and Concepts III. Proc. SPIE 6212, pp. 17–21, April 2006, Gaylord Palms Resort and Convention Center Orlando (Kissimmee), Florida, USA

[14] I. V. Minin, O. V. Minin, D. Prather, S. Shi, "The potential of flat curvilinear DOE as a key element of future integrated diffractive optics and information protected element," In Proceeding of the 5th IEEE-Russia Conference "Microwave electronics: measurements, identification, applications," MEMIA 2005, pp. 13-15, December 2005, Novosibirsk, Russia, pp. 186–193.

[15] Y. Y. Feng and M. Willatzen, "Plasmonic effects in dynamic tunable metal-dielectric composites," PIERS Online, Vol. 4, No. 6, pp. 625–630, 2008.

[16] R. Blaikie, L. Lin, and R. Reeves, "Surface-plasmon-enhanced optical transmission through planar metal films," PIERS Online, Vol. 1, No. 6, pp. 634–637, 2005.

[17] T. Suyama, Y. Okuno, and T. Matsuda, "Plasmon resonance-absorption in a metal grating and its application for refractive-index measurement," PIERS Online, Vol. 1, No. 6, pp. 659–663, 2005.

[18] P. Wang, X. J. Jiao, L. Tang, D. G. Zhang, Y. H. Lu, J. P. Xie, and M. Hai, "A planar metallic collimator based on controlling surface plasmons's phase," PIERS Online, Vol. 1, No. 3, pp. 369–371, 2005.

Call for Papers

Journal of Electromagnetic Analysis and Applications (JEMAA)

ISSN: 1942-0730 (Print), 1942-0749 (Online)
www.scirp.org/journal/jemaa

JEMAA is a professional journal in the field of electromagnetic analysis, testing and application. The goal of this journal is to provide an international platform for engineers and academicians all over the world to promote, share, and discuss various new issues and developments in the field of electromagnetic. This journal is edited to encourage deeper understanding and greater effectiveness in theory analysis, testing, numerical calculation and engineering application that relevant electromagnetic fields.

Editors-in-Chief

Subject Coverage

JEMAA publishes four categories of original technical reports: papers, communications, reviews, and discussions. Papers are well-documented final reports of research projects. Communications are shorter and contain noteworthy items of technical interest or ideas required rapid publication. Reviews are synoptic papers on a subject of general interest, with ample literature references, and written for readers with widely varying background. Discussions on published reports, with author rebuttals, form the fourth category of JEMAA publications. Topics of interest include, but are not limited to:

- Electromagnetic Numerical Analysis
- Multiphysics Coupled Problems
- Electromagnetic Inverse Problems
- Electromagnetic Structure Optimization
- Test Electromagnetic Analysis Method
- Workshop Benchmark Problems
- Electromagnetic Devices
- Electromagnetic Compatibility
- Electromagnetic Nondestructive Testing
- Electromagnetic Material Modelling

Notes for Intending Authors

Submitted papers should not be previously published nor be currently under consideration for publication elsewhere. Paper submission will be handled electronically through the website. All papers will be peer reviewed. For more derails about the submissions, please access the website.

Website and E-Mail

http://www.scirp.org/journal/jemaa jemaa@scirp.org

J. Electromagnetic Analysis & Applications, 2010
Published Online February 2010 in SciRes (http://www.SciRP.org/journal/jemaa).

CONTENTS

Volume 2 Number 2 **February 2010**

9771942073000 06